THEORETICAL AND EXPERIMENTAL STUDIES OF ATOMIC AND MOLECULAR SCATTERING

by

DAVID SMITH HORNE

Thesis presented for the degree of

DOCTOR OF PHILOSOPHY

University of Edinburgh

October, 1969.

CONTENTS

ACKNOWLEDGEMENTS

SUMMARY

1. INTRODUCTION 1

General Introduction 2

Collisions and the Molecular Beam Method. 7

A Resume of Elastic Scattering Theory. 12

2. THEORY 17

Introduction. 18

Molecular States of the Alkali Halides. 19

Models for Potential Energy Curves. 25

Alkali Halide Ground State. 32

Curve Crossing Problem. 35

Scattering Predictions for the Potassium-Iodine Atom System. 48

An Expression for the Total Cross-Section Arising from a Screened Coulomb Potential. 56

Scattering Predictions for the Potassium Iodine Molecule case. 60

3. ATOMIC BEAM SOURCES 68

Introduction. 69

The Radio Frequency Discharge Source. 74

Thermal Iodine Source. 87

4. EXPERIMENTAL 94

Introduction. 95

Description of Apparatus. 96

Detection and Modulation System. 100

Experimental Set Up. 106

Preliminaries and Data Acquisition Procedure. 109

5. RESULTS AND DISCUSSION 113

Treatment of Results. 114

Results. 123

Total Cross-Section Results. 135

Potassium + Iodine Atom Scattering. 141

Potassium + Iodine Molecule Scattering. 168

Sodium + Iodine Atom Scattering. 173

CONCLUSIONS 174

REFERENCES 175

ACKNOWLEDGEMENTS

I wish to thank Dr. M. A. D. Fluendy and Dr. K. P. Lawley for their advice, encouragement and understanding.

To all other members of the Edinburgh Molecular Beams Group my thanks also, in particular to Mr. W. Stevenson, our transformer of mind into metal.

I am indebted to the University of Edinburgh for the provision of laboratory, library and computing facilities and also to the Carnegie Trust for the Universities of Scotland for a Scholarship during the period of this work.

SUMMARY

Small angle differential cross-sections in the thermal energy range are reported for the elastic scattering of potassium from atomic and molecular iodine. Such interactions are among the simplest two-state curve crossings to be found in chemistry.

The situation is complicated by the fact that the curve-crossing case is only one of four which can occur when an alkali metal and a halogen atom collide. It was hoped that information on both the curve-crossing and these other interactions would be derived from the small angle scattering in the thermal energy range.

The molecular beam apparatus had already been constructed for alkali metal-alkali metal collisional studies. The chief modification to this was the building of a halogen atom source. The iodine atom source was of a two-chamber design, with the temperature of the upper chamber controlling the degree of dissociation. A radio frequency discharge source for atomic chlorine is also described.

The other main modification was the introduction of a cross-beam modulation system to increase the detection efficiency. As before the primary beam was velocity selected before collision, the scattered alkali particles being surface ionized and subsequently counted.

In both iodine atom and molecule cases differential cross-sections were measured at three different relative collision energies. The angular structure in the iodine atom system was found to be best interpreted in terms of an adiabatic potential involving an electron transfer at the crossing point plus an 'effective' covalent potential to account for the other three interactions. This latter potential is a Lennard-Jones (12, 6) with $\epsilon = 5 \times 10^{-14}$ ergs and

$C_6 = 1400 \times 10^{-60}$ ergs cm^6.

The interpretation of the iodine molecule results has been based on the 'optical model' treatment since in this case chemical reaction opens another exit channel for the scattering species. The results here lend hope that the small angle scattering of reactive species will prove to be a sensitive function of both the form and parameters of the reaction probability function.

C H A P T E R I

I N T R O D U C T I O N

INTRODUCTION:

Using the crossed molecular beam technique theoretical and experimental investigations have been made into the thermal energy scattering of potassium with iodine molecules and atoms and of sodium with atomic iodine. Measurements of both total and differential cross-sections (at small angles) were made for both atomic iodine cases, only the differential small angle scattering being measured for molecular iodine.

These measurements are expected to yield information on the long range forces prevailing before reaction in the iodine molecule case as well as providing an insight into the effect of curve-crossing in collision processes.

Since I succeeded to a molecular beam machine which came on-line for alkali-alkali scattering during my period of work, the main experimental requirement for the above study was a halogen atom source. Two have been built. The first, used only for iodine, supplies the dissociation energy thermally while the second dissociates the molecule in a radiofrequency discharge.

From a theoretical point of view these scattering processes are interesting in that they provide classic examples of curve crossing. In its ground state the alkali halide molecule is essentially $M^+ X^-$ near its equilibrium bond distance. Calculations based on such a model (RIT 51, HON 54, RIC 57) agree well for experimentally determined quantities such as dissociation energies, vibration-rotation coupling constants and variation of the dipole moment with vibrational state or internuclear distance. However, such a model can only be used to construct a potential energy curve describing molecular properties near the equilibrium position.

The Coulombic (ionic) potential energy curve fails to give a correct picture of the adiabatic dissociation of any alkali halide molecule, since the products must be two uncharged atoms in their ground states. Thus the zeroth order potential curve for the 'purely ionic' configuration must cross that for the 'purely covalent' configuration at some point, R_c. During a collision in this energy state the electron distribution of the atoms must undergo an abrupt change in the vicinity of R_c from dominantly covalent outside to dominantly ionic inside. This corresponds to the jump of electron from the alkali to the halogen atom, though should R_c be large or the relative kinetic energy be high the electron may not have time to jump and the purely covalent curve will be followed.

The range, R_c, at which electron transfer is expected to occur is given by

$$e^2/R_c = I(M) - E(X) \qquad (1)$$

where I (M) is the ionization potential of the alkali atom and E (X) is the electron affinity of the halogen atom. Thus taking the electron affinity of atomic iodine as 3.078 eV (BER 62) and the ionization potentials of potassium and sodium as 4.339 eV and 5.138 eV (COT 62) respectively the crossing points for the systems K/I and Na/I (in Å) are found to be 11.27 and 6.93 respectively. In calculating these values it has been assumed that the Coulombic attraction is dominant and that in effect the covalent potential energy curve is horizontal at the crossing-point.

From these considerations, one may draw potential curves like those of fig. 1.1. which show the behaviour of some of the KI states which have the same symmetry as the molecular ground state.

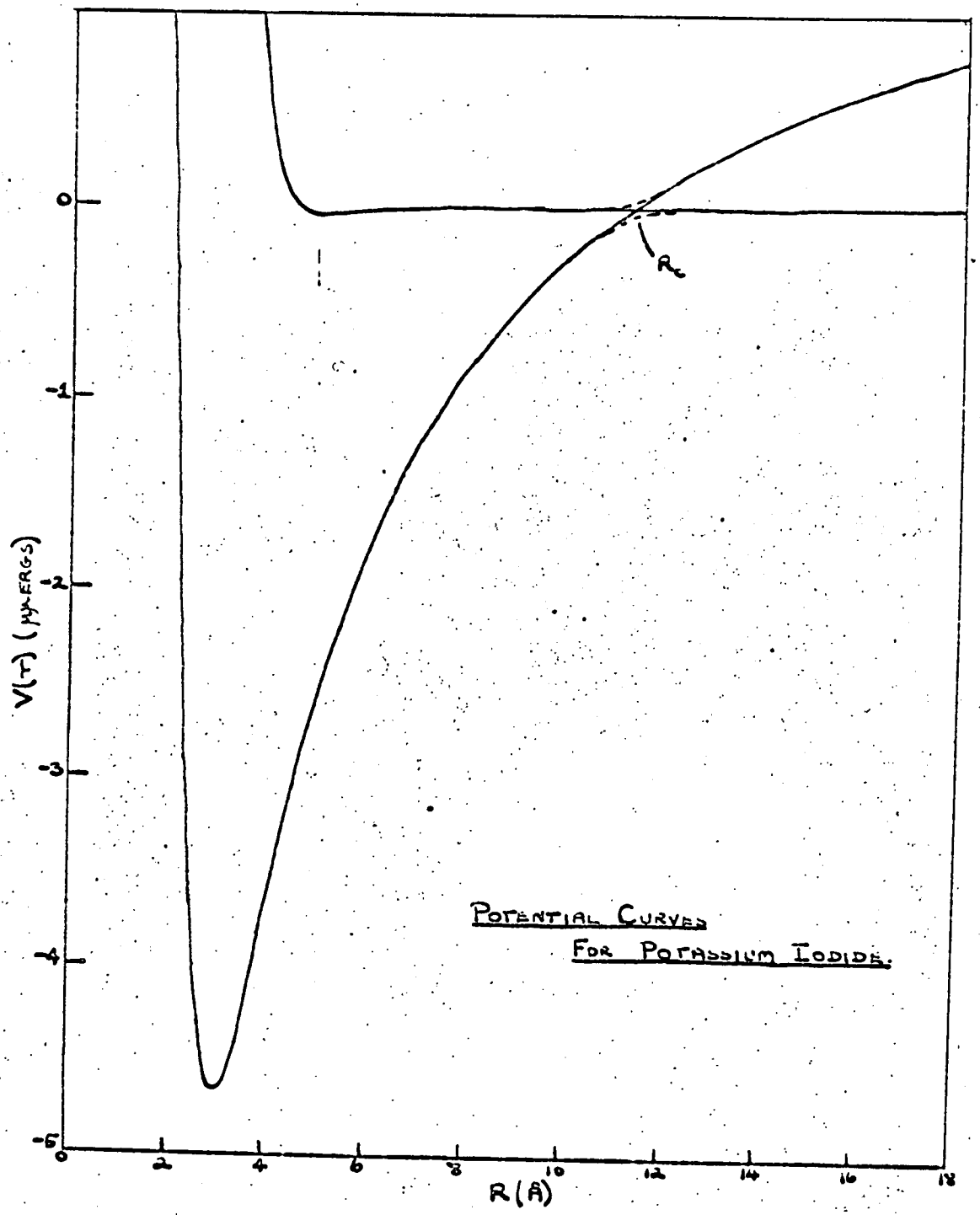

Fig. 1.1. K-I potential curves.

The alkali halide molecule's ground state is appropriately denoted as $^1\Sigma^+$ in the notation of Hund's case (a) coupling. Here both Λ, the component of orbital angular momentum along the internuclear axis, and Σ, the corresponding component of total spin angular momentum, are both good quantum numbers. Should it be possible to so describe the molecular states formed from an alkali atom (^2S) and a halogen ($^2P_{3/2}$), then these states will be denoted $^1\Sigma$, $^3\Sigma$, $^1\Pi$ and $^3\Pi$. Of these only one has the same symmetry as the ionic ground state. Moreover, the statistical weightings of these states (1, 3, 2 and 6 respectively) are such that only 1/12 of the colliding pairs of atoms interact along this $^1\Sigma$ curve. In accordance with the non-crossing rule only these pairs have any possibility of electron transfer, so that 11/12 of the atom pairs will undergo scattering from the other three potential curves.

However, it may be that only Ω, the resultant of Λ and Σ is a good quantum number. In this case, Hund's case (c) notation should be used, and the molecular states formed from the atoms will be :- 0^+, 0^-, 1, 2, with the 0^+ state having a weight of 1/8.

Neglecting the scattering from the purely covalent curves, the effect of curve crossing on the thermal energy scattering has been investigated by Child (CHI 69) who has shown, using a semiclassical treatment, that the cross-section for the M-X case goes over from being determined by the covalent potential curve to being governed by the ionic curve as the interaction between the states increases. With the K-I crossing point at 11.27 Å and that of NaI at 6.93, the KI ought to have less chance than NaI of following the ionic curve, so that KI would have a smaller interaction between the states than the Na/I system.

Evidence from U-V absorption spectroscopy (BER 57) supports this view. During an absorption the behaviour of an alkali halide molecule may be pictured as follows: absorption of light carries the system vertically from the ground state to the $^1\Sigma^+$ excited state and produces a change in the electronic wave function corresponding to the transfer of an electron from the halide ion to the alkali. Following this, the nuclei move apart toward R_c. As this point is reached, the electronic wave function readjusts itself, and, effectively, the electron leaves the metal again for the halogen. Electrostatic forces then pull the nuclei together again and the above process is reversed. If the electron follows perfectly as the nuclei move, the $^1\Sigma^+$ state will have bound levels and the electronic absorption spectrum should show a series of bands. Should the electrons not follow the nuclear motion, then as the nuclei move apart beyond R_c they will continue as two neutral particles. This corresponds to a continuum level of the ground electronic state, lying to the red of the adiabatically determined dissociation limit. This latter possibility is an apparent violation of the non-crossing rule. For KI a strong continuum lies well to the red of a state dissociating to K (^2S) and I ($^2P_{1/2}$) while for NaI, instead of a continuum, a band spectrum appears (SOM 29, LEV 31, BER 57). Thus in KI it appears that the non-crossing rule is violated in dissociation, so that scattering from the covalent curve might be expected to dominate whereas in NaI this rule is obeyed and the colliding atoms would appear to follow the Coulombic curve.

Further discussion of these conclusions is postponed until the results of the present study have been given.

In the next chapter the theoretical problem is gone into in much greater detail while chapters three and four give a description of atomic beam sources

and the apparatus in general. The remainder of this chapter is devoted to a short introduction to the molecular beam method.

COLLISIONS AND THE MOLECULAR BEAM METHOD.

Although the decay of atoms or molecules in excited states with emission of photons is a process occurring spontaneously at a calculable rate, nearly all other formation and destruction processes in physics and chemistry involve the collision of two or more particles. Such collisions may involve only the exchange of kinetic energy and in these so-called elastic collisions only the direction of the relative velocity vector is changed. Alternatively in processes where the quantum states of the particle are changed either by the addition or removal of energy, an inelastic collision is said to have taken place. Reactive collisions, the third and final category, are those in which chemical reactions occur and thus, in general, involve a change in the masses of the individual colliding partners.

The essential advantage of the crossed molecular beam technique for investigating collisional phenomena is that the smearing over relative velocities and internal states can be reduced considerably.

A molecular beam is defined as a unidirectional stream of gas with a density so low that collisions among molecules in the beam do not occur. To prevent attenuation of the beam by collision with other molecules in the scattering chamber this must be evacuated to around 10^{-6} torr or less. Because the beam molecules experience no collisions, their velocities and internal states do not change in their passage through the apparatus to the scattering region, where, in a crossed-beam experiment, they interact with a second beam.

As a consequence of these collisions occurring in the scattering region, the primary beam intensity, I_o , is attenuated to I according to Beer's Law

$$I = I_0 \exp\left(-n.\sigma^{\mu}_{tot}(g).L\right) \qquad (2)$$

The total cross-section, $\sigma^{\mu}_{tot}(g)$, is, in general, the sum of the elastic scattering cross-section and the sum over all inelastic and reactive cross-sections. It is a function of the intermolecular potential which will vary with the quantum states, denoted by μ, of the colliding molecules, as well as depending on the relative velocity of the colliding partners. Because the crossed beam technique is being used the number density of scatterers, n, and the path length through them, L, must be replaced by $n(x)dx$, the integral of the intensity of the cross-beam over the main beam path through the scattering region.

Measuring the intensity of scattered primary beam as a function of the scattering angles, θ and ϕ, relative to the incident beam, yields the differential cross-section, $I^{\mu}_{v}(\theta, \phi, g)$. The differential cross-section is related to the total cross-section by

$$\sigma^{\mu}_{tot} = \int I^{\mu}(\theta, \phi, g) \sin\theta \, d\theta \, d\phi . \qquad (3)$$

If the potential is isotropic, I^{μ} is independent of ϕ and the above expression simplifies to

$$\sigma^{\mu}_{tot} = 2\pi \int I^{\mu}(\theta, g) \sin\theta \, d\theta . \qquad (4)$$

These then, the total cross-section and the differential cross-section, are the two quantities measured in a molecular beam experiment, the former by measuring the attenuation of the primary beam at $\theta = 0$, the latter by measuring the scattered intensity of primary beam particles at some angle θ.

Thermal energy beams are formed by effusion of a gas or the vapour of a solid or liquid into the scattering chamber through a small hole in the 'oven' wall. At some point in front of this, collimating slits serve to define the beam. Thereafter the beam may be velocity or state selected. Velocity selection is generally achieved using a rotating disc selector of

the Fizeau type. This consists of a number of toothed wheel discs mounted on a shaft, each disc with its slots mutually offset from its neighbour's. The fast rotation of such a device allows the transmission of only a narrow band of velocities, the transmitted velocity being determined by the speed of rotation. Inhomogeneous magnetic fields similar to the well-known Stern-Gerlach arrangement have been used to select molecules in specific rotational quantum states. Such magnets have also been used as velocity selectors (FLU 65) in cases where the beam atom possessed a magnetic dipole since the deflection is a function of velocity. Spin-state selection has also been achieved with two pole (BED 62) or six-pole (BRA 68) fields.

Fig. 1. 2. shows a schematic diagram of a crossed beam apparatus, with two molecular beams containing the reactants being allowed to intersect at the scattering centre.

To determine the angular distribution of the collision products some form of detector is rotated about the scattering centre in the plane of both beams. Alternatively the source configuration may be rotated about the scattering centre with the detector held fixed.

The number of product molecules scattered into a solid angle element $d\Omega$ is given by

$$N_{product} = n_1 n_2 g V \frac{d\sigma}{d\Omega} d\Omega . \qquad (5)$$

where n_1, n_2 are the two beam fluxes, g is their relative velocity, V is the scattering volume and $d\sigma/d\Omega$ is the differential cross-section in the laboratory system. The solid angle 'seen' by the detector is approximately given by $d\Omega = A_{det}/L^2$ where A_{det} is the detector area and L is the distance from the scattering volume to the detector.

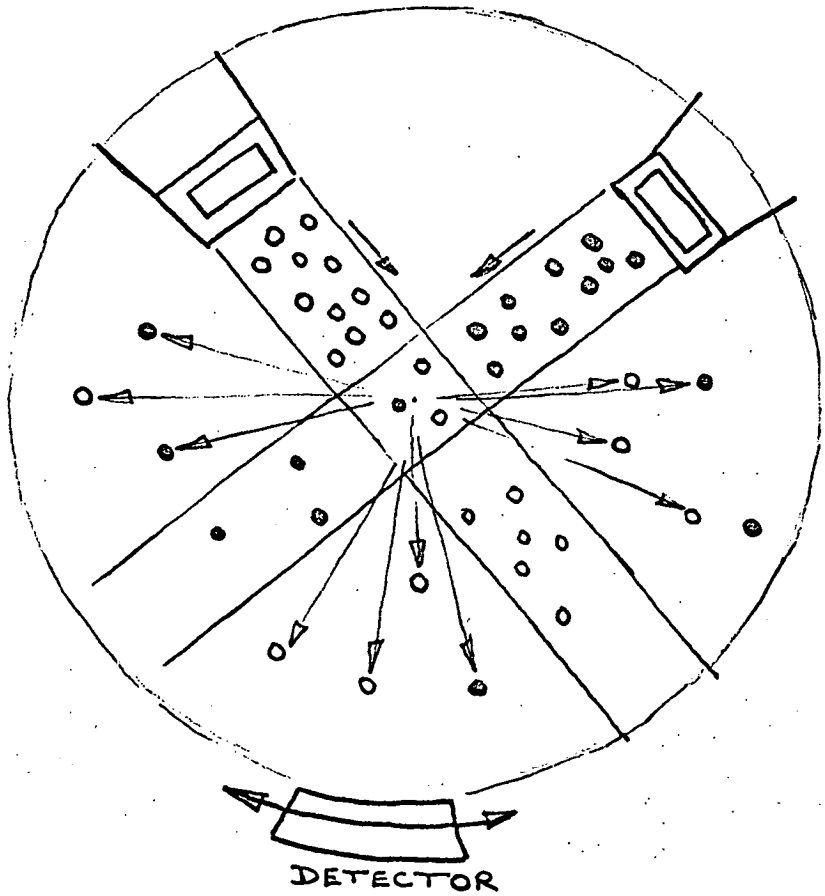

Fig. 1.2. Schematic diagram of crossed molecular beam apparatus.

From the above equation it is possible to estimate the product molecule intensity arriving at the detector. Assuming a cross-section of $d\sigma/d\Omega = 50$ Å^2/str, a detector solid angle of 2.10^{-5} sr, we obtain an expected scattered signal of approximately 10^4 molecules per sec. This assumes a main beam flux of 10^9 molecules per cm.^{2} per sec. and a cross beam flux of 10^{13}.

This corresponds to an electron current of 10^{-15} amps if all the molecules are converted into ions. Since the intensity is so low an extremely efficient detector is required to make the experiment possible. Difficulties are also encountered because the product density is less by several orders of magnitude than the residual gas density in the apparatus. Thus the detector must be able to discriminate between background molecules and product.

The most widely used and most sensitive detectors available at present rely on surface ionization. This detector is based on the surface reaction.

$$M + W \longrightarrow M^+ + \epsilon + W \qquad (6)$$

where M is some alkali and W is a tungsten surface, though metals such as Pt, Re and Ir can be used in place of W. The reaction proceeds in the forward direction if the ionization potential of M is less than the work function of the metal surface. With a hot metal surface, the ions evaporate and can be removed and collected by electric fields. Under favourable conditions efficiencies of the order of 100% can be achieved.

The surface ionizer is, however, limited in its range of detectable molecules. For other substances ionization can be brought about by electron bombardment or field emission. The resulting positive ions must then be mass analyzed to differentiate them from ions produced from the background. This

method is considerably less sensitive than the hot wire ionizer (0.1% to 1%).

To study collision processes, other than those of the alkalis, there must be an increase in beam intensities to compensate for the lack of detection sensitivity. This can be achieved to some extent by using multiple aperture sources or Laval nozzles (HER 66) but increased beam intensities mean the employment of more efficient pumping systems with possible separately pumped source and scattering chambers, and of course, the apparatus becomes considerably more complicated than the simple outline started with.

A RESUMÉ OF ELASTIC SCATTERING THEORY.

Classical. By separating out the motion of the centre of mass of the system, the two body collision problem can be formally reduced to the problem of one particle interacting with a central force field, V (r). This single particle has a mass equal to the reduced mass of the two colliding particles ($\mu = m_1 m_2 / m_1 + m_2$) and is moving with a velocity, g, equal to their initial relative velocity.

Using the conservation of energy and of angular momentum, the angle of deflection, Θ, is obtained as a function of impact parameter, b:

$$\Theta(b) = \pi - 2b \int_{r_0}^{\infty} \frac{dr}{r^2 \sqrt{(1 - b^2/r^2 - V(r)/E)}} \qquad (7)$$

r_0, the lower limit of integration being the distance of closest approach, given by the largest root of the square root term of the integrand.

Corresponding to each value of the impact parameter, there will be a deflection angle, Θ. Fig. 1.3b. illustrates the typical form the relationship between b and Θ will take for an interaction of the form shown in Fig. 1. 3a. For a head-on collision, b = o, $\Theta = \pi$, because the particle will be reflected straight back when it encounters the inner repulsion.

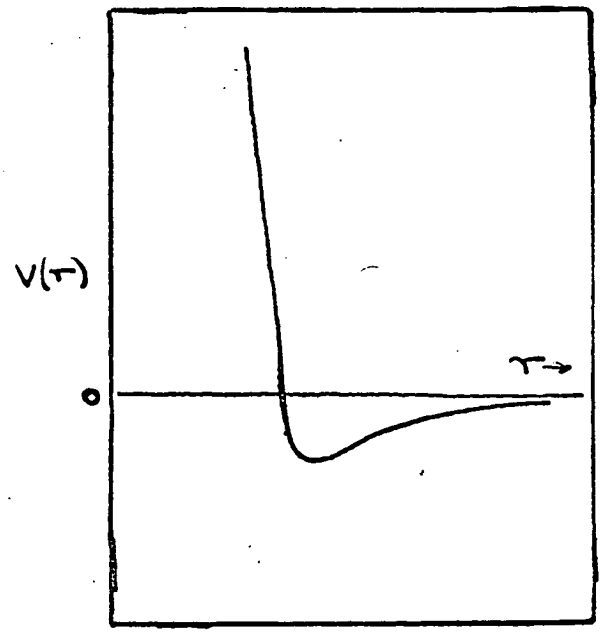

3a.

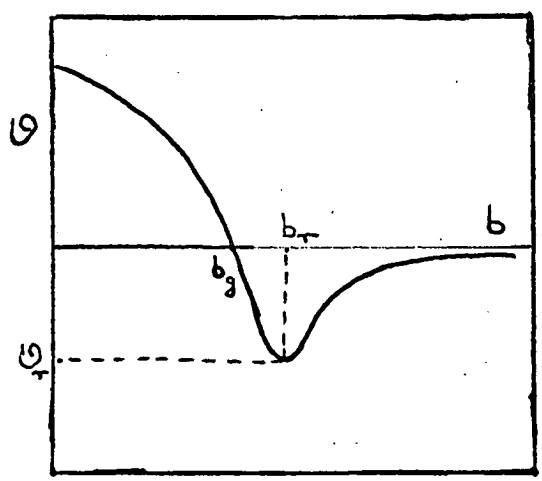

3b

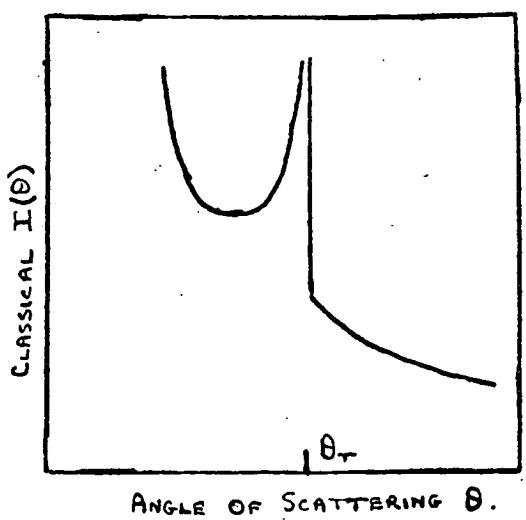

3c.

Fig. 1.3a. Typical form of the interaction energy V(r)

1.3b. Typical form of the relation between impact parameter and angle of deflection.

1.3c. Form of the classical differential cross-section.

As b increases the attraction begins to be felt more and more, so Θ decreases and at same value, b_g, of b the effect of attraction and repulsion will counter-balance to give $\Theta = 0$. Further increase of b will lead to negative values of Θ of increasing magnitude up to a maximum at $b = b_r$. For such collisions the maximum influence of the attraction is felt. As b increases beyond b_r the particle feels less and less of the long range interaction so Θ diminishes in magnitude to vanish as b tends to ∞.

The deflection angle is related to the scattering angle by the relation

$$\vartheta = |\Theta| - s\pi \qquad (8)$$

since ϑ must lie between 0 and π. Using this relation Fig. 1. 3b. can be converted into a plot showing b as a function of the angle of scattering. For the least complex case with the maximum value of $|\Theta|$ at $b = b_r < \pi$ we have the plot shown in Fig. 1. 3c.

Particles for which the impact parameter lies between b and $b + \Delta b$ contribute an amount $2\pi b \Delta b$ to the effective cross-section.

Since $$2\pi b \Delta b = 2\pi b \frac{\Delta b}{\Delta \Theta} \cdot \Delta \Theta$$

we see that $$I(\Theta) = 2\pi b \frac{\Delta b}{\Delta \Theta} \qquad (9)$$

or in the limit $$I(\Theta) = 2\pi b \frac{db}{d\Theta}$$

Referring to Fig. 1. 3c, however, we see that corresponding to any particular value of Θ there will be more than one value of b. The classical differential cross-section is obtained simply by adding these contributions. Arising from this expression, there are several interesting points to note. It will be seen from Fig. 1. 3c. that $\Theta = 0$ not only as b tends to ∞ but also at $b = b_g$. This enhancement of the singularity in classical scattering at $\Theta = 0$ is referred to as a 'glory' singularity. A further singularity in $I(\Theta)$ occurs at $b = b_r$ when $d\Theta/db$ tends to 0 and hence $db/d\Theta$ tends to ∞.

This is known as a rainbow singularity.

However, these singularities are never observed in practice and it is on this point as on others that classical theory fails. Other inadequacies of classical theory are its failure to explain the oscillatory structure of $I(\theta)$ or the exponential behaviour at very small angles.

QUANTUM THEORY. In quantum theory the contributions from the different branches of the b-θ plot are no longer simply added. Each contributes separately, not to the scattered intensity, but to the amplitude of the scattered wave, and the contributions differ in phase. The result is that, when they are combined, a complicated interference pattern is super-imposed on the classical distribution.

The singularities in the classical distribution are present now in a modified form and no longer lead to infinite values of $I(\theta)$ either as tends to 0 or as θ tends to θ_r, the rainbow angle at which $b = b_r$.

As in the classical case the quantum mechanical problem reduces to considering the scattering of a particle of reduced mass, μ, from a centre of force. The problem is now to solve the Schroedinger equation for motion in a spherically symmetric potential, V (r). This equation can be written as

$$(\nabla^2 + k^2)\,\psi(r) = \frac{2\mu}{\hbar^2} V(r)\,\psi(r) \qquad (10)$$

where $k = (2\mu E/\hbar^2)^{1/2}$ is the wave number of the incoming wave. The solution required must have an asymptotic form corresponding to an incident plane wave and an outgoing spherical scattered wave with amplitude $f(\theta)$:

$$\text{i.e.} \quad \psi(r) = \exp(ikz) + \frac{f(\theta)}{r}\exp(ikr) \qquad (11)$$

If the incident flux is g particles / cm.^{2}/sec. where g is the relative velocity, the flux scattered through a solid angle $d\Omega$ is then

$$I(\theta) = |f(\theta)|^2 g\, d\Omega \qquad (12)$$

The differential cross-section is the fraction of the incident flux scattered into $d\Omega$ and hence is given by

$$I(\theta) = |f(\theta)|^2 \qquad (13)$$

In molecular scattering problems eq.(10) is usually solved by expressing the incident wave as an infinite sum of partial waves each with an orbital angular momentum, L . Using this method it can be shown (MOT 65, ROD 67, WU 62) that $f(\theta)$ is given by

$$f(\theta) = \frac{-i}{2k} \sum_{L=0}^{\infty} (2L+1)(\exp 2i\eta_L - 1) P_L(\cos\theta) \qquad (14)$$

where $P_L(\cos\theta)$ are the Legendre functions and η_L are the phase shifts. These latter contain all the information about the scattering process.

CHAPTER II

THEORY.

Introduction.

As already noted, in the region of the equilibrium bond distance, the alkali halide molecule is well described by an ionic model, yet the molecule dissociates to ground state atoms so that a curve crossing must be avoided as the species separate. The effect of this curve crossing on the measured scattering pattern has been the subject of this investigation but the picture is complicated by the fact that since the halogen atom is in a P state collisional interaction between the alkali and halogen atoms may take place along a number of potential energy curves.

Molecular States of the Alkali Halides.

The ground state of an alkali metal atom is a ^2S while that of an iodine atom is $^2P_{3/2}$, the first excited state of the halogen being a $^2P_{1/2}$ 0.943 eV above ground. The atomic spin-orbit coupling is large in the iodine atom whereas it is customary to regard it as very weak in the alkali. At sufficiently large internuclear distance, however, even the atomic spin-orbit splitting of the alkali will be large compared to the interaction energy so that in this region jj coupling will be applicable. The molecule (two interacting atoms) then has a quantum number Ω for the absolute value of the total angular momentum along the internuclear axis. At low values of R, in the region of r_e, the interaction energy may be greater than the individual atomic spin-orbit coupling so that (Λ, S) coupling would then prevail in the molecule, the quantum number Λ being the absolute value of the total orbital angular momentum along the axis, and S being the total spin.

The molecular states for (Λ, S) coupling are given by the Wigner and Witmer rules (WIG 28) for determining the possible values of the projections M_{L_1} and M_{L_2} of L_1 and L_2, the atomic orbital angular momenta, on the internuclear axis. For the KI case $L_1 = 0$ and $L_2 = 1$ so that the possible values of Λ, given by $|M_{L_1} + M_{L_2}|$ are 0 and 1. The resulting values of S are 0 and 1 also, one for each M_{L_1}, M_{L_2} combination.

Using the conventional notation, the KI states resulting from (Λ,S) coupling are thus

$$^1\Sigma_0 \; , \; ^3\Sigma_{0,1} \; , \; ^1\Pi_1 \; , \; ^3\Pi_{0^+,0^-,1,2}$$

the subscripts being the quantum number $\Omega (= |\Lambda + S|)$ of the total angular momentum about the internuclear axis. The statistical weightings of these molecular KI states are respectively 1, 3, 2 and 6.

At large values of R, where (j, j) coupling is applicable, the molecular states are defined by the values of the quantum number $\Omega (= |M_{J_1} + M_{J_2}|)$ (MUL 30.) For Iodine, $J_1 = 3/2$, while for potassium, $J_2 = \frac{1}{2}$, so that the possible M_J values are

$$M_{J_1} = -3/2, \; -\tfrac{1}{2}, \; +\tfrac{1}{2}, \; +3/2.$$

$$M_{J_2} = -\tfrac{1}{2}, \; +\tfrac{1}{2}.$$

leading to the values of

2 (from $(-3/2, -\frac{1}{2})$ and $(3/2, \frac{1}{2})$)

1 (from $(-3/2, \frac{1}{2})$, $(3/2, -\frac{1}{2})$, $(\frac{1}{2}, \frac{1}{2})$ and $(-\frac{1}{2}, -\frac{1}{2})$

and 0 (from $(\frac{1}{2}, -\frac{1}{2})$ and $(-\frac{1}{2}, \frac{1}{2})$

Further since the $\Omega = 0$ state arises because $M_{J_1} = -M_{J_2}$, these states are designated 0^+ and 0^-, in this case the state of lower energy being 0^+. Every combination of M_{J_1} and M_{J_2} corresponds to a different molecular state so that the statistical weightings are 2, 4 and 2 for $\Omega = 2, (1, 1)$ and $(0^+$ and $0^-)$

The transition between the two types of coupling will occur over some intermediate range of R but since the correlation diagram will strongly depend on the ordering of the energy levels something must first be said about this.

Spectroscopy exhibits a dearth of information on this point. Much data is available on the ionic state of the molecule, which must be regarded as the ground state of the molecule. The states we are discussing can be regarded as excited states of this molecule. They are thought to be purely repulsive or in some instances to possess very shallow wells of only around 100 cm^{-1} since the absorption spectrum is mainly continuous but shows diffuse bands near the long wave end of the continuum (BAR 53).

No other spectroscopic information is available though a number of approximate but very useful relations among these different potential energy curves of the alkali halides can be obtained from the perfect pairing

approximation of simple valence bond theory (COU63). Assuming negligible spin-orbit coupling in the atoms, we have seen that as the atoms approach they can follow at lower r values any one of the four interaction curves corresponding to the molecular states $^1\Sigma$, $^3\Sigma$, $^1\Pi$ and $^3\Pi$. In a simply way it is easy to understand how these four curves arise. The electronic configuration for the alkali atom ground state gives it one S electron in its outer electron shell while the outer shell of the halogen can be

$$p_x^2, p_y^2, p_z \qquad (m_L = 0)$$

OR

$$p_x, p_y^2, p_z^2 \qquad (m_L = 1).$$

i.e. there is an unpaired electron on each atom and when the two atoms approach these can be paired in various ways. Two states result when the electrons are paired (i.e. the electron spins are antiparallel) namely the $^1\Sigma$ and the $^1\Pi$. The other two states $^3\Sigma$ and $^3\Pi$ have electrons of parallel spin. Conventionally we would take the $^1\Sigma$ as arising from the pairing of the electrons in the S and p_z orbitals and this state would be the lowest in energy.

The mathematical expression of these statements, usually called the perfect pairing approximation is normally written as follows.

$$V = \sum_{\text{all } i,j} Q_{ij} + \sum_{\substack{\text{orbitals with} \\ \text{paired spins}}} J_{ij} - \frac{1}{2}\sum_{\substack{\text{orbitals with} \\ \text{unpaired spins}}} J_{ij} - \sum_{\substack{\text{orbitals with} \\ \text{parallel spins.}}} J_{ij} \qquad (1)$$

where Q_{ij} is a Coulomb integral between the orbitals i and j, and J_{ij} is an exchange integral. Since the alkali halides only have a single bond the third term in this expression is zero. The approximate expressions for the

interaction energies for the four states of MX are

$$\begin{aligned} V(^1\Sigma) &= Q + J_{sp_z} \\ V(^3\Sigma) &= Q - J_{sp_z} \\ V(^1\pi) &= Q + J_{sp_x} \\ V(^3\pi) &= Q - J_{sp_x} \end{aligned} \qquad (2)$$

Thus at large separations where Q between neutral atoms is very small

$$\begin{aligned} V(^1\Sigma) &= -V(^3\Sigma) \\ V(^1\pi) &= -V(^3\pi) \end{aligned} \qquad (3)$$

Thus with the $^1\Sigma$ level being the lowest in energy, the $^3\Sigma$ is the highest of the four. On the above basis we would also expect the $^1\pi$ and $^3\pi$ to lie between these two in that order, but Magee (MAG 40) says that the exchange integral J_{sp_x} is positive and the order here is therefore reversed, the $^3\pi$ being lower in energy.

The order of the molecular states with (Λ, S) coupling is therefore

$$^1\Sigma, \ ^3\pi, \ ^1\pi, \ ^3\Sigma$$

With this in mind, a possible correlation diagram for the transition between the various forms of coupling has been drawn in Fig. 2.1. To make more quantitative estimates of the range of internuclear distance within which each type of coupling is operable or where the transition occurs (if it occurs), would require a complete solution of the molecular wave equation, possibly using the methods outlined by Tai Yup Chang (CHA 67).

With potassium iodine, however, the crossing point occurs at around 11.3 A. In this region jj coupling is almost certainly applicable so that

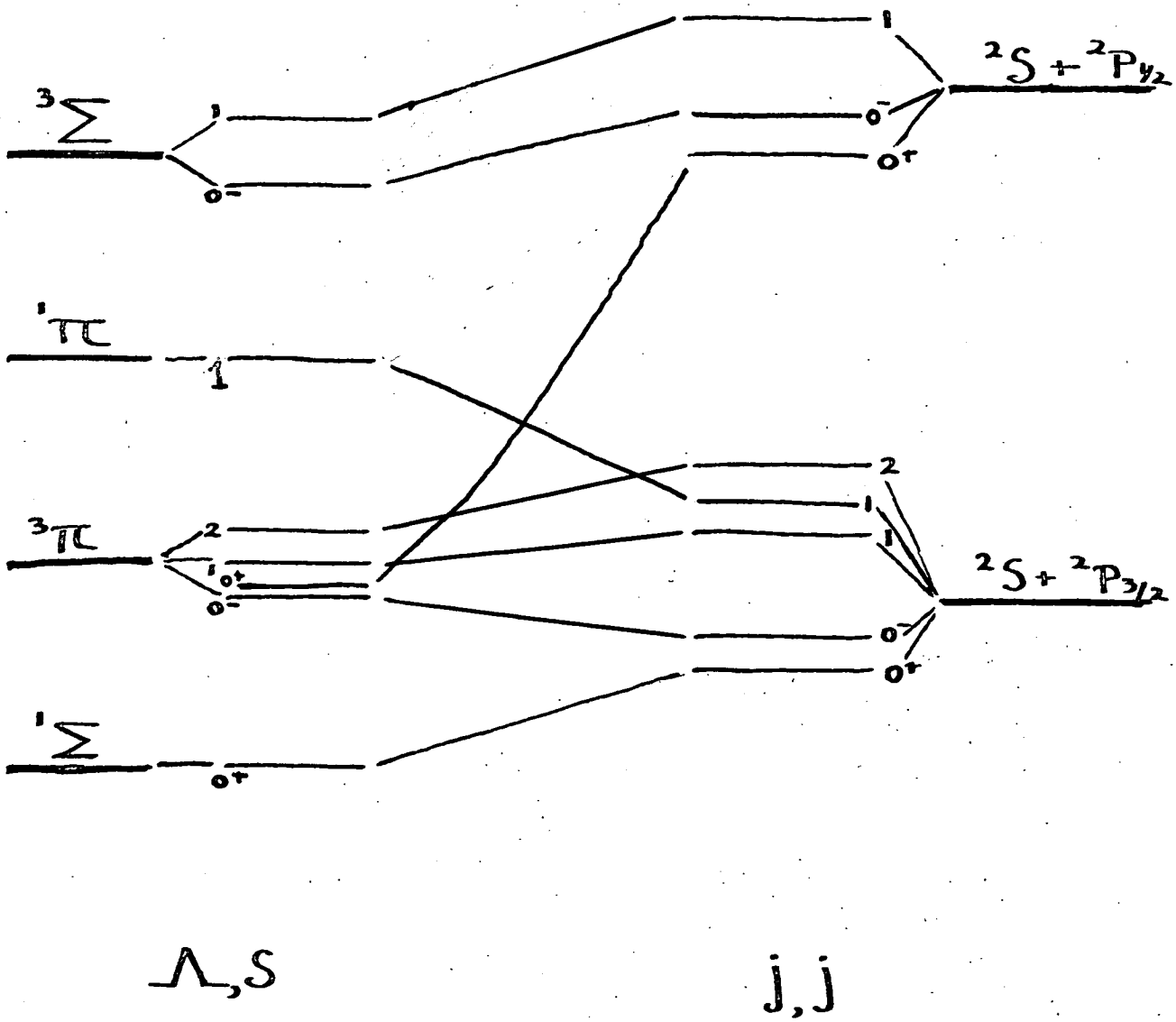

Fig. 2.1. Possible Correlation Diagram.

Note that the complete spectrum of (Λ,S) states is formed by considering both the $P_{1/2}$ and $P_{3/2}$ states of the halogen atom. In our experimental situation only those formed from the $P_{3/2}$ state are accessible, the upper state lying above our collision energies.

the 0^+ state which has the same symmetry as the ionic state will have a statistical weighting of $\frac{1}{8}$. i.e. only $\frac{1}{8}$ of the colliding pairs will have a chance of ever interacting along the ionic curve, the other $\frac{7}{8}$ will follow one of the other three covalent paths. (See page 20).

Should our assumption of (jj) coupling be incorrect, a completely different weighting must be assigned to the molecular states of (Λ, S) coupling. Here the $^1\Sigma$ state which is symmetrical with the ionic state and thus avoids crossing it, only has a weighting of 1/12. The other states are weighted as below.

$^3\Sigma$ = 1/4

$^1\Pi$ = 1/6

$^3\Pi$ = 1/2

Models for Potential Energy Curves.

For the purposes of discussion, it is convenient to divide interatomic and intermolecular forces into short, intermediate and long-range forces.

The short-range forces are invariably repulsive and rise sharply with decreasing internuclear separation. They are usually approximated by some large negative power of R, generally 12.

The long range forces take over at sufficiently large R where the charge distributions of the two interacting molecules do not overlap. It is further convenient to consider the various contributions to these long range forces under three headings.

(i) Electrostatic. (or permanent multipole - multipole forces).

(ii) Dispersion.

(iii) Induction.

(i) The electrostatic contributions to the intermolecular potential energy results from the interactions of the various multipole moments in the molecule: charges, dipoles, quadrupoles, etc. Though the iodine atom possesses a quadrupole moment, the alkali atom has no multipole moments, so that there is no electrostatic contribution to the potential.

(ii) Dispersion contributions have their origins in and may be calculated by use of quantum theory. In view of the difficulties associated with the calculations, various approximate formulae have been derived for the coefficients of these terms in the interaction series. The first term of this series varies as r^{-6} though there are further terms varying as r^{-8}, r^{-10} etc., which may be neglected in the first round of fitting.

The C_6 coefficient may be variously estimated from the London formula

$$C_6 = \frac{3}{2} \cdot \frac{I_a E_b \alpha_a \alpha_b}{I_a + I_b} \qquad (4)$$

where I_a, E_b are the ionization energies of the atoms and α_a, α_b are the polarizabilities, or the Kirkwood - Muller formula

$$C_6 = \frac{6 m_e c^2 \alpha_a \alpha_b}{N_0} \Big/ \left[\frac{\alpha_a}{\chi_a} + \frac{\alpha_b}{\chi_b} \right] \qquad (5)$$

where α_a, α_b are again the polarizabilities, χ_a, χ_b are the diamagnetic susceptibilities of the molecules, N_0 is Avogadro's no., M_e is the electronic mass and C the velocity of light, or, as another alternative, reached from the same beginning by a different approximation, the Slater - Kirkwood formula gives

$$C_6 = \frac{3 e \hbar}{m_e^{1/2}} \frac{\alpha_a \alpha_b}{(\alpha_a/N_a)^{1/2} + (\alpha_b/N_b)^{1/2}} \qquad (6)$$

Where N_a, N_b are the numbers of electrons in the outer shells of the atoms and all other symbols have been defined before or have their usual meaning.

Unfortunately all of these formulae have been found unsatisfactory. (SAL 50, PIT 59). Both the London and Slater - Kirkwood formulae give C_6 coefficients which are usually too small whereas the Kirkwood - Muller formula generally gives too large a value. The formulae are thus by no means accurate though they may be useful for order of magnitude calculations.

A further drawback on their use in this instance is the lack of data on the polarizability of atomic iodine, either theoretical or experimental. In the end a value of 4.6 α - 24 cm^3 was estimated by subtracting the polarizability of atomic hydrogen from that of hydrogen iodine using the values listed in Hirschfelder, Curtiss & Bird (HIR 64). For the alkali metal polarizabilities, an average of the values published in the table of Bederson and Robinson (BED 66) was used. Diamagnetic susceptibilities were obtained from International Critical Tables. For the ionization potential

and electron affinity, the values given in Chapter I were used. Substitution of these values as required by the various formulae led to the following values of the dispersion coefficient for the potassium - iodine system

C_6 (London) = 700. $\alpha - 60$ ergs. $cm.^6$

C_6 (Slater - Kirkwood) = 310. $\alpha - 60$ ergs. $cm.^6$

C_6 (Kirkwood - Muller) = 790. $\alpha - 60$ ergs. $cm.^6$

In view of the wide disparity in these values and the empirical guesswork involved in the estimation of the iodine atom polarizability, a range of C_6 values from 800 to 1800 was included in our calculations of scattering patterns.

(iii) Induction Contribution and Calculation of the Quadrupole Moment.

Because of the halogen's quadrupole moment, a dipole may be induced in the alkali leading to an attractive r^{-5} term in the potential.

According to the definition of Buckingham (BUC 59) the Θ_{zz} component of the quadrupole moment tensor is given by

$$\Theta_{zz} = \frac{1}{2}\int_0^{\infty}\int_0^{\pi}\int_0^{2\pi} (3\cos^2\theta - 1)\,\rho\, r^2 \sin\theta \, d\phi \, d\theta \, dr \qquad (7)$$

where ρ, the charge density is given by $\psi^* \psi e$, ψ being the normalized one - electron wave function for an outer shell electron. Only the outer shell gives rise to a quadrupole moment, the inner shells being spherically symmetric. For atomic iodine, wave functions with n, l, m and s as good quantum numbers are available. (HER 63). However, in iodine the jj coupling scheme is more correct with n, j, m and s as good quantum numbers. The tabulated functions $\psi_{n,l,m,s}$ must therefore first of all be transformed to functions $\psi_{n,j,m,s}$.

Following Slater (SLA 60), we may write for a wave function with a given J and M

$$\varphi_{J,m} = \sum_{m_L, m_S} C_{m_L, m_S; J, m}\, \phi_{m_L} \qquad (8)$$

Where $C_{m_L, m_S; J, m}$ are the Clebsch - Gordan coefficients and ϕ_{m_L} are the unperturbed functions characterized by M_L , M_S .

Slater lists the formulae for the required Clebsch - Gordan coefficients as

$$\begin{aligned}
S = \tfrac{1}{2} : J = L + \tfrac{1}{2} \;,\; m_s = \tfrac{1}{2} \;;\; C &= \sqrt{\frac{L+m+\tfrac{1}{2}}{2L+1}} \\
m_s = -\tfrac{1}{2} \;;\; C &= \sqrt{\frac{L-m+\tfrac{1}{2}}{2L+1}} \qquad (9) \\
J = L - \tfrac{1}{2} \;,\; m_s = \tfrac{1}{2} \;;\; C &= -\sqrt{\frac{L-m+\tfrac{1}{2}}{2L+1}} \\
m_s = -\tfrac{1}{2} \;;\; C &= -\sqrt{\frac{L+m+\tfrac{1}{2}}{2L+1}}
\end{aligned}$$

so that the wave functions of the various J states of I ($^2P_{3/2}$) are as given below

$$\begin{aligned}
\varphi_{3/2,\,3/2} &= \phi_1 \beta \\
\varphi_{3/2,\,1/2} &= \sqrt{\tfrac{2}{3}}\,\phi_0 \beta + \tfrac{1}{\sqrt{3}}\,\phi_1 \alpha \\
\varphi_{3/2,\,-1/2} &= \tfrac{1}{\sqrt{3}}\,\phi_{-1} \beta + \sqrt{\tfrac{2}{3}}\,\phi_0 \alpha \qquad (10) \\
\varphi_{3/2,\,-3/2} &= \phi_{-1} \alpha
\end{aligned}$$

The ψ_{m_L} wave functions are given by

$$\psi_{m_L} = \frac{P_{nl}(r)}{r} \Theta_{lm}(\theta)\, \Phi_m(\phi) \qquad (11)$$

where $P_{nl}(r)$ is the radial wave function as tabulated

$\Theta_{lm}(\theta)$ is the spherical harmonic $\left(= \sqrt{\frac{3}{2}} \cos\theta \quad \text{for } m_L = 0 \right.$

$\left. = \frac{\sqrt{3}}{2} \sin\theta \quad \text{for } m_L = \pm 1 \right)$

and $\Phi(\phi) = e^{im\phi}$

Using these wave functions transformed using equations (11) and the quadrupole moment definition, the values of Θ_{zz} listed were found for the J states of atomic iodine.

$$\text{For} \quad \varphi_{3/2,\pm 3/2} \qquad \Theta_{zz} = -\frac{e\langle r^2\rangle}{5} \qquad (12)$$

$$\text{where } \langle r^2\rangle = \int_0^\infty P(r)^2 r^2 dr$$

$$\varphi_{3/2,\pm 1/2} \qquad \Theta_{zz} = \frac{e\langle r^2\rangle}{10}$$

P (r) being the iodine 5p one electron wave function listed by Hermann and Skillman. The integration was carried out numerically, using a Simpson's rule routine with an automatically varying step length, the inter-tabulated values being found using a seven-point interpolation formula (backward, forward or central differences as required). This gave a value for $\langle r^2\rangle$ of 6.593Å^2, so that the values of Θ_{zz} are

$$\text{For} \quad \varphi_{3/2,\pm 3/2}, \quad \Theta_{zz} = -2.11\,\alpha - 26 \text{ e.s.u.}$$

$$\text{For} \quad \varphi_{3/2,\pm 1/2}, \quad \Theta_{zz} = 1.06\,\alpha - 26 \text{ e.s.u.} \qquad (13)$$

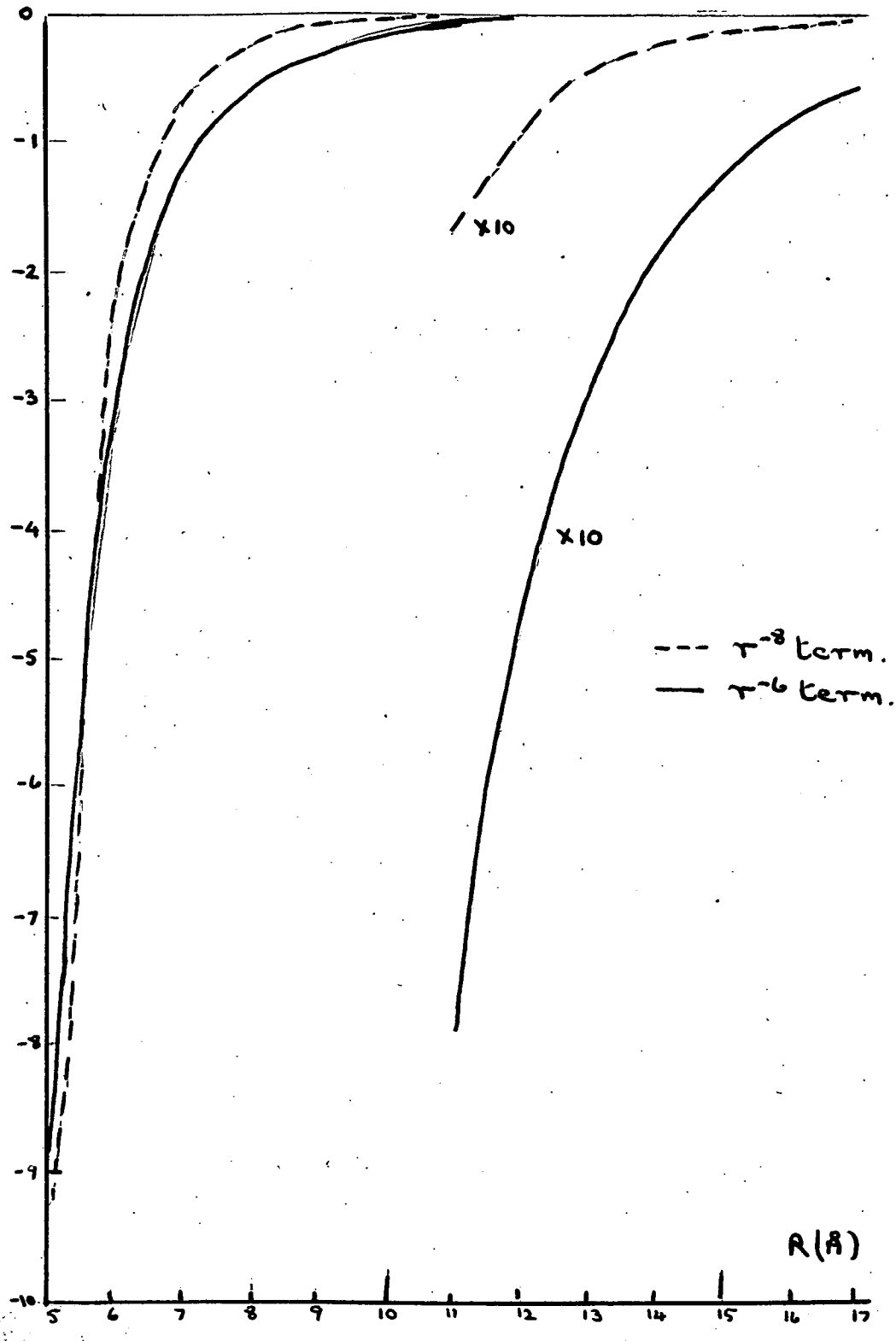

Fig. 2. 2. Comparison of r^{-6} and r^{-8} terms in the K/I interaction.

Again following Buckingham, the field due to the quadrupole along the line of centres is

$$F = 3\Theta_{zz}/r^4$$

the induced potential due to this being $V = -\frac{1}{2}\alpha F^2$ where α is the polarizability of the other atom. Thus the C coefficient in the potassium iodine atom potential is given (for each state) by

$$C_8 = \frac{9}{2}\alpha_K \Theta_{zz}^2$$

assuming the zz axis follows the line of centres through the collision.

With jj coupling applying, the statistically weighted average over the molecular states gives

$$C_8 = \frac{9}{10}\alpha_K \langle r^2 \rangle^2 e^2$$

yielding a value of $3.61\alpha - 72$ ergs cm .

Assuming a value of $1400\alpha - 60$ ergs. cm^6 for the dispersion C_6 coefficient a compatison of the attractions from induction and dispersion forces is given in Fig. 2.2. This shows that the attraction due to quadrupole - induced dipole forces is approximately $1\frac{1}{2}$ times the dispersion contribution at 4 Å (assuming multipole expansion is valid at such a small separation) dropping to less than 10% at 10 Å and continuing to fall relative to the dispersion force. In spite of this no r^{-8} term was included in any potential used in scattering calculations. Since an empirical fit to the data was being attempted, it was felt that the attractive forces would best be represented by a single term in r^{-6}, the introduction of extra parameters probably not being justified by the data.

The repulsive part of the potential due to short range forces was estimated by a positive term in r^{-n} where n ranged from 10 to 14 in our calculations.

Alkali Halide Ground State.

Patel et al. (PAT 67) have compared four different potential energy curves for alkali halide diatomic molecules, all of them assuming the molecule to be constituted of ions. They were

(1) Born Mayer $$V(r) = -e^2/r + B\exp(-r/\sigma). \quad (17)$$

(2) Rittner

$$V(r) = -\frac{e^2}{r} - \frac{e^2(\alpha_1+\alpha_2)}{r^4} - 2\frac{e\alpha_1\alpha_2}{r^7} - \frac{C}{r_6} + A\exp\left(-r/\rho\right) \quad (18)$$

(3) Varshni - Shukla

$$V(r) = -\frac{e^2}{r} + P\exp(-kr^2) \quad (19)$$

(4) Modified Varshni - Shukla

$$V(r) = -\frac{e^2}{r} + P\exp(-kr^{3/2}) \quad (20)$$

B, σ, A, ρ, P and k are constants; α_1, and α_2 are the polarizabilities of the ions.

Varshni and Shukla (VAR 61) concluded that their potential model (3) was superior to the Born-Mayer but slightly inferior to Rittner's. Patel et al, have modified Varshni and Shukla's potential to give 4 which they claim accounts for rotational and vibrational constants more satisfactorily.

Graphs of the last three potentials are shown in Fig. 2.3. where it can be seen that the 1/r term quickly dominates all the potentials for $r > r_e$. Honig et al (HON 54) have given the value of r_e as 3.0478 ± 0.0001Å while Herzberg (HER 50) gives the energy for dissociating the KI molecule into ground state atoms as 3.33eV. Thus the Rittner potential seems to be inferior to the other two in the prediction of the minimum position and all three seem to straddle the experimentally observed value of the well-depth. Since this

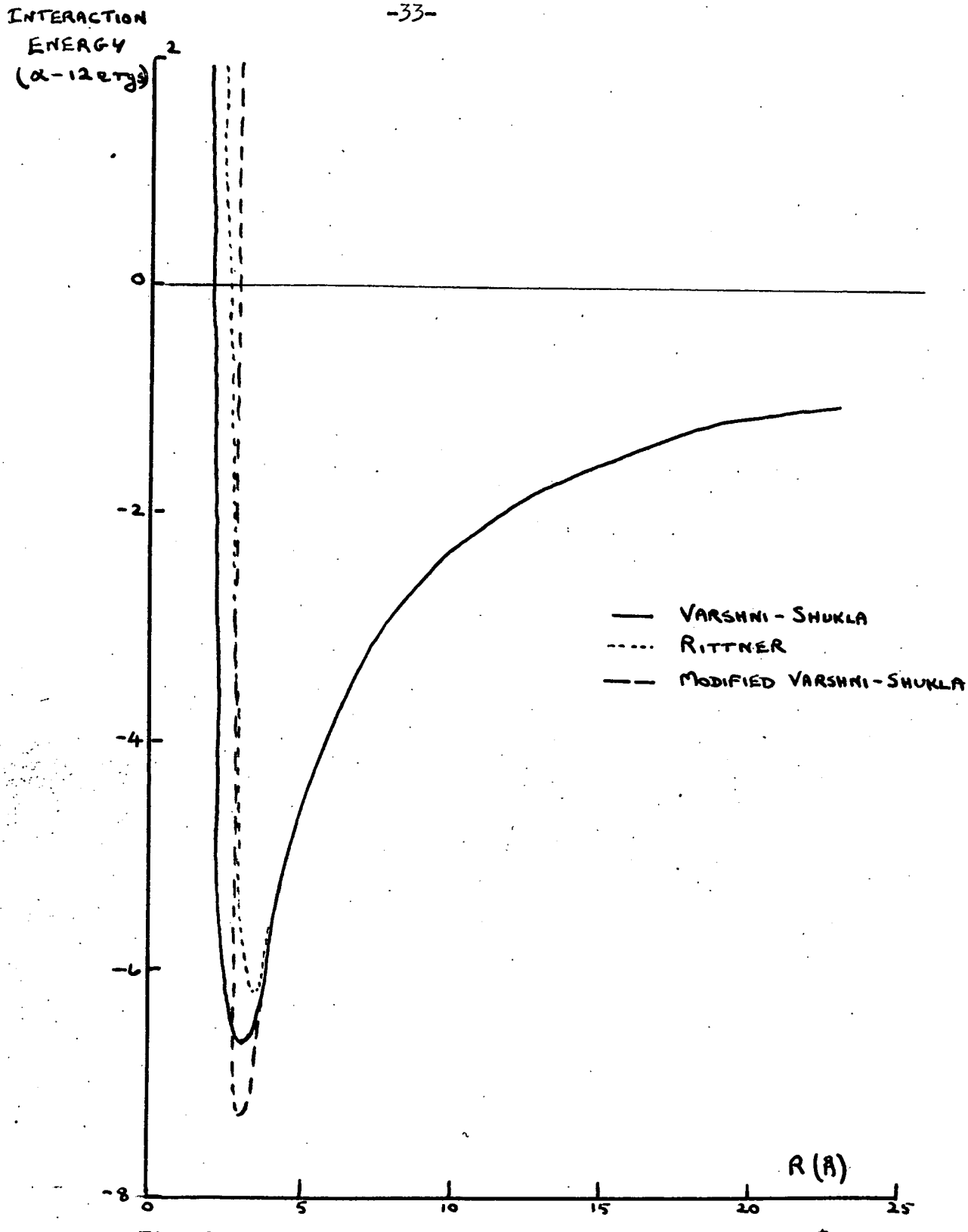

Fig. 2.3. Comparison of ionic model potentials for K^+ I^-

latter value is probably in error by approximately 3%, no conclusion can really be drawn about the relative performances of the potentials 2, 3 and 4 in this respect.

None of the potentials being obviously better than the others, the Varshni - Shukla potential (3) was arbitrarily chosen as the potential curve for the ground (ionic) state ($^1\Sigma$) of the potassium iodide molecule.

Curve Crossing Problem.

Having considered the covalent and ionic interactions possible in an alkali halide molecule, these and the curve crossing problem will now be placed in perspective.

An alkali halide molecule in its ground state can be represented fairly well by an ionic model yet the dissociation products are neutral atoms. An avoided curve crossing must therefore occur during the dissociation. When we bring such a pair of atoms together, however, interaction takes place along several potential curves, the number and weighting of these depending on the type of coupling assumed. But only one curve has the same symmetry as the ionic state curve so that it is only on this curve that the avoided crossing can occur. Fig. 2.4. shows schematically the crossings and avoided crossings for this situation where it has been assumed that jj coupling is applicable.

The majority ($\frac{7}{8}$) of the interactions between the two atoms therefore take place on the comparatively shallow-welled, if not repulsive, purely covalent curves, so that it is possible that the scattering features produced by the curve-crossing event will be masked by their behaviour. For the moment, therefore, the other covalent states will be forgotten and the curve-crossing will be treated as the two-state problem it really is.

Considerable theoretical interest has been shown recently in the role of curve crossing in atomic and molecular collisions (LEV 69, CHI 69) although only in the latter case has any real attempt been made to predict scattering behaviour at thermal energies. The following is by no means a complete summary of this literature but is merely an outline of the problem and of Child's method of solution (CHI 69).

At thermal energies, the two atoms must come together on the covalent

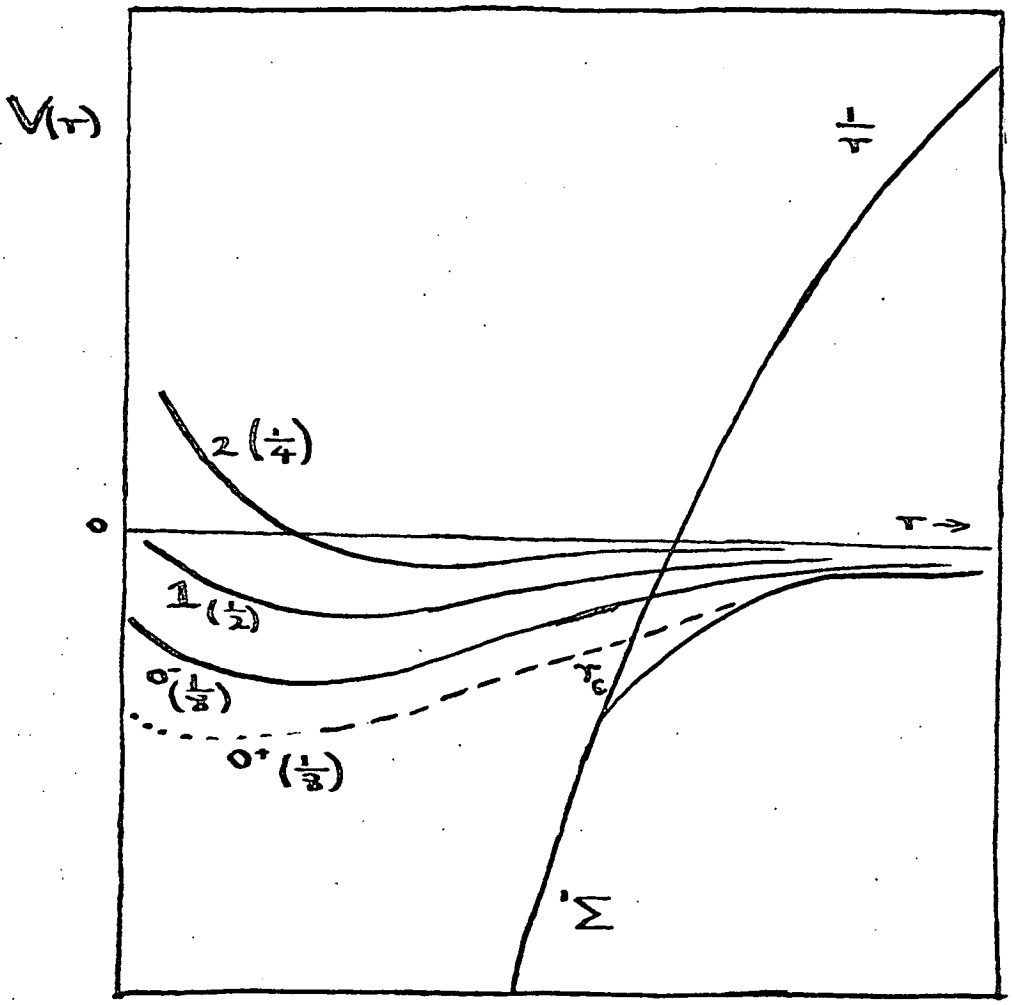

Fig. 2.4. Schematic K-I potentials in region of crossing point (Brackets give weighting appropriate for jj coupling)

0^+ or $^1\Sigma$ curve (see Fig. 2.5.) If the two particles are thought of as colliding with a definite impact parameter b or angular momentum L the incoming wave packet can be analyzed into two coherent parts, one of which is the result of scattering entirely on V_o , the second to scattering on V_o for internuclear separations greater than R_c and on V_b for $R < R_c$. Speaking classically for the moment each of them follows the trajectory for its potential, V_o or $V_o \rightarrow V_b$, and is ultimately scattered through its own classical angle, $\Theta_1(L)$ or $\Theta_2(L)$. If the observations are made at $\Theta = \Theta_2(L)$ then the upper part of the packet will not be observed here since it is being scattered predominantly to some other angle (namely, $\Theta_1(L)$). However, there is some different angular momentum, L' , such that $\Theta_2(L) = \Theta = \Theta_1(L')$, and the true scattering observed at the angle Θ is classically the sum of these two contributions but quantally the interference between these two coherent parts of a plane wave. Our problem is to calculate the relative extent to which scattering takes place on the upper and lower potential curves, always remembering that the system must always return to its initial state.

Following the model of Born and Oppenheimer for molecular problems, it is usual to take advantage of the extreme difference in masses between electrons and nuclei to separate the electronic and nuclear co-ordinates. The nuclear motion can then be taken as slow compared to the electronic motion so that it has appeared natural to base a description of the collision process on the representation of adiabatic molecular states. This representation is all the more attractive because it is now relatively covenient, though expensive of computer time, to make numerical computations of electronic wave functions and energy levels as a function of the internuclear co-ordinates, which are treated as fixed (or adiabatically varying) parameters. In itself the

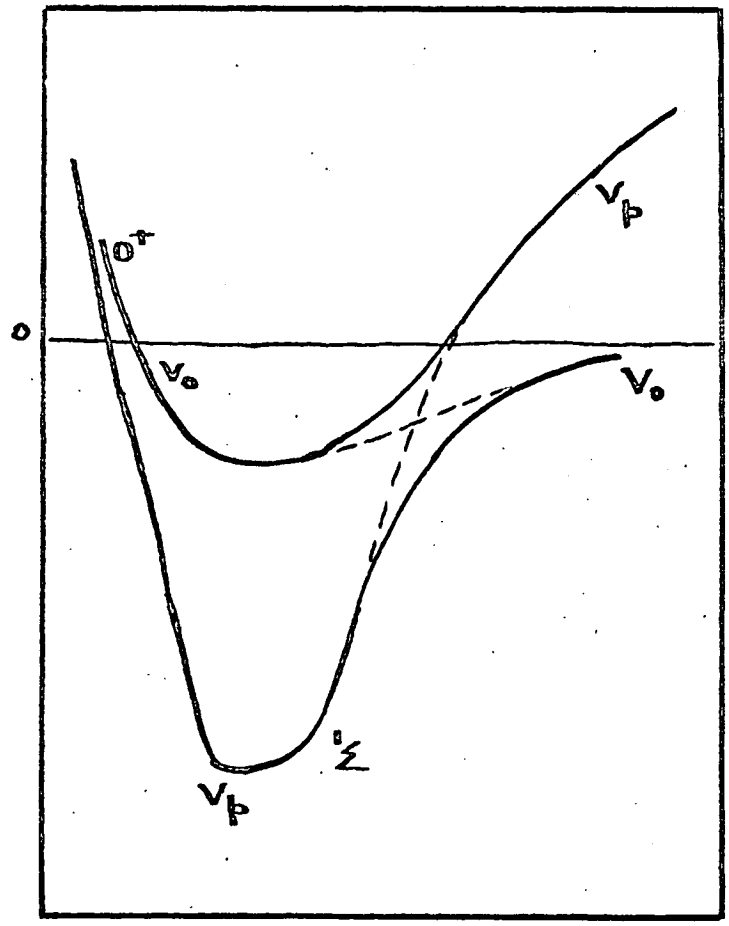

Fig. 2.5. Schematic of two state curve-crossing problem.

adiabatic representation gives no obvious indication of the parameter governing inelastic transition probabilities. Indeed, from the adiabatic point of view all such inelastic transitions result from a break-down of the Born-Oppenheimer separation of co-ordinates. One of the most important sources of such transitions lies in the situation where two adiabatic molecular states approach each other closely, i.e. the situation existing in the potassium-iodine atom or molecule case. This problem was studied originally by Landau (LAN 32), Zener (ZENER 32) and Stueckelberg (STU 32) who derived the familiar Landau-Zener formula for the transition probability.

Child's (CHI 69) analysis of the K - I/I_2 problem is based on a model similar to that used by Landau and Zener in that the potential curves are taken to vary linearly with distance and the interaction between them is taken to be constant over the region of the crossing. His solution may be briefly summarized as follows.

Expanding the wave functions for both coupled states in partial waves leads to the following coupled equations for the $l^{th.}$ partial wave:

$$\left.\begin{aligned} \left(\frac{-\hbar^2}{2\mu}\frac{d^2}{dr^2} + V_1^{\ell}(r) - E\right) u_{1\ell} &= A(r)\, u_{2\ell} \\ \left(\frac{-\hbar^2}{2\mu}\frac{d^2}{dr^2} + V_2^{\ell}(r) - E\right) u_{2\ell} &= A^*(r)\, u_{1\ell} \end{aligned}\right\} \quad (21)$$

where $$V_i^{\ell}(r) = V_i(r) + \ell(\ell+1)\hbar^2/2\mu r^2$$

Boundary conditions are set by the requirement that the wave functions remain finite in the classically inaccessible regions, $r < a_{1\ell}$ for $u_{1\ell}$ and $r > b_{2\ell}$ for $u_{2\ell}$ in Fig. 2.6. The solution is normalized by setting the incoming part of $u_{1\ell}$ (r) equal to the incoming part of a plane wave; in the semi-classical approximation:

$$u_{1\ell}(r) \sim \sqrt{\frac{k_1(\infty)}{k_{1\ell}(\infty)}}\left[C_\ell \exp\left(i\int_{a_{1\ell}}^{r} k_{1\ell}(r) - \frac{i\pi}{4}\right)\right. \tag{22}$$

$$\left. + \exp\left(-i\int_{a_{1\ell}}^{r} k_{1\ell}(r) + \frac{i\pi}{4}\right)\right)$$

where $k_{1\ell}(r) = \sqrt{2\mu\left(E - V_1^{\ell}(r)\right)}/\hbar$

The total wave in the incident channel then becomes

$$u_1(r) = \frac{1}{2ikr}\sum_{\ell=0}^{\infty}(2\ell+1)\, i^{\ell} \exp(i\eta_\ell)\, u_{1\ell}(r) P_\ell(\cos\theta) \tag{23}$$

$$\approx \exp(ikz) + f(\theta)\exp(ikr)/r \tag{24}$$

$$f(\theta) = \frac{1}{2ik_1}\sum_{\ell=0}^{\infty}(2\ell+1)\left[C_\ell \exp(2i\eta_\ell) - 1\right] P_\ell(\cos\theta) \tag{25}$$

and η_ℓ is the phase shift for scattering under $V_1(r)$; in semi-classical form

$$\eta_\ell = \lim_{r\to\infty}\left\{\int_{a_{1\ell}}^{r} k_{1\ell}(r)\,dr - k_1 r + (\ell+1/2)\pi/2\right\} \qquad (26)$$

The required differential cross-section for elastic scattering $I(\theta) = |f(\theta)|^2$ differs from that for scattering under $V_1(r)$ in so far as the coefficients, c_ℓ, derived from equation (21) differ from unity.

The Landau-Zener model is then introduced as a means of providing an approximate solution to equation (1). Two assumptions are made by this model.

(i) the interaction term $A(r)$ is real and constant.

(ii) over the range of r where the interaction is important:

$$V_i^\ell(r) = \left(-k^2/2\mu\right) f_i x + V_i^\ell(r_x) \qquad (27)$$

where $x = r - r_x$ and r_x is the crossing point in Fig. 2.6, both of these being tied up in the main assumption that transitions occur to an appreciable extent only in a very narrow zone around the crossing point.

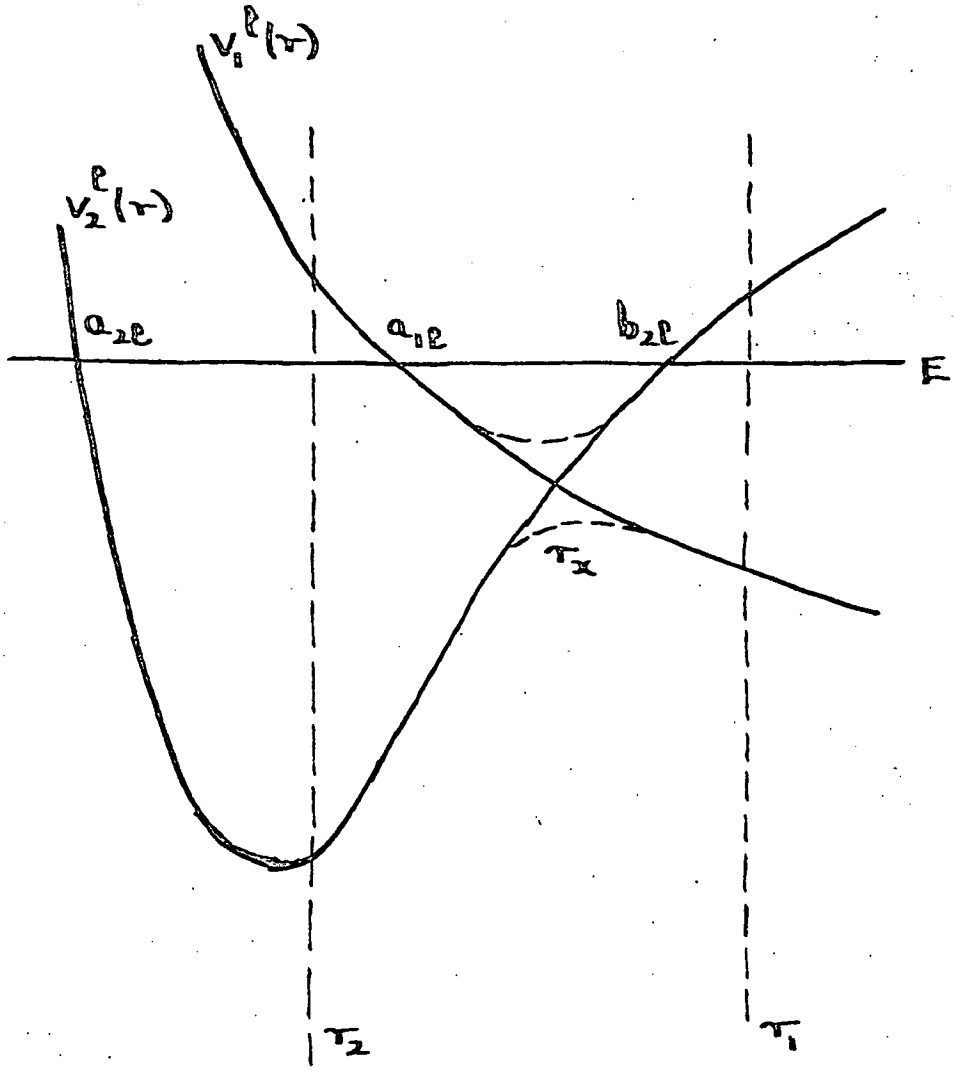

Fig. 2.6. Curve Crossing Diagram (Chi 69)

The use of such a model was severely criticised by Bates in 1960 (BAT 60) on the grounds that at high velocities the transition probability is expected to be proportional to v^{-2} whereas the LZ formula leads to a probability proportional to v^{-1} in this limit. Heinrichs (HEI 68) points out that Coulson and Zalewski (COU 62) and Dubrovskii (DUB 64) have shown that generalized formulae which have the correct behaviour in v^{-2} at large velocities and reduce precisely to the LZ formula at low velocities can be derived in the framework of the near adiabatic formulation. On the other hand, in Watson's treatment (WAT 68) the LZ formula is obtained in a precise inherent limit, namely for velocities less than a certain upper value. This value is such that the expansion of the formula in powers of $1/v$ which is used in Bates's argument is not valid. All of these results, Heinrichs' included, indicate that there exists a range of low velocities in which the LZ formula is valid and where it is essentially unaffected by the precise behaviour of the probability at high velocities. Heinrichs, however, goes on to show that a better approximation to the transition probability is obtained if one assumes, consistently with the Landau-Zener model, that the transitions take place in a small region of atomic size round the point R_c of the trajectory. By defining the width of this finite region as $2S\sqrt{\gamma}$ where $S \geq 1$ is a numerical constant and γ is as defined by the LZ formula, a precise condition which inherently limits the range of validity of the LZ formula as a lowest-order approximation is derived. This condition is nothing more than a form of the criterion for the validity of the near-adiabatic collision theory and merely expresses the fact that v must be small compared to a typical electronic orbital velocity.

Having established that the use of the Landau-Zener model is justifiable, Child's introduction of it reduces the coupled equations to

$$u_1'' + (\epsilon - f_1 x) u_1 = \alpha u_2$$
$$u_2'' + (\epsilon - f_2 x) u_2 = \alpha u_1 \qquad (28)$$

where $\epsilon = 2\mu(E - V^{\ell}(r_x))/\hbar^2$ and $\alpha = 2\mu A/\hbar^2$

Bykhovskii et al (BYK 65) have obtained the solution of this equation when f_1 and f_2 are both positive. Child, following similar lines solves them for the case where $f_1 > 0$ and $f_2 < 0$, which case is claimed to exist for the K - I situation. Taking account of the sign in the first term on the right hand side of equation 2.27 , the coefficient f_1 can only be positive for all values of L if the diabatic or covalent state of KI is purely repulsive. The effective potential $V_1^{\ell}(r)$ will eventually give a negative slope at the crossing point but for low values of L its slope must be positive so that the equations ought first to be solved for the case where both f_1 and f_2 are negative changing to Child's case for some value of L dependent on the covalent potential parameters and the position of the crossing point. Assuming that only the attractive r^{-6} term need be considered at the crossing point of 11.27Å, the slope of the effective potential curve becomes positive for L = 50 when $C_6 = 1400 \text{Å}^6$ μergs. This low value of L, coupled with the fact that Bykhovskii et al., also obtain the Landau-Zener formula for the transition probability, make it permissible to use Child's result over the complete range of L.

In the case of the alkali atom-halogen atom case he gives the coefficient C_{ℓ} by the equation

$$C_{\ell} = \frac{\cos\beta_{\ell} - \mu_{\ell}\cos\phi_{\ell}\exp[i(\beta_{\ell} - \phi_{\ell})]}{\cos\beta_{\ell} - \mu_{\ell}\cos\phi_{\ell}\exp[-i(\beta_{\ell} - \phi_{\ell})]} \qquad (29)$$

where $$\mu_{\ell} = \exp(2\pi\delta_{\ell}) - 1$$

and δ_{ℓ} is the Landau-Zener parameter, given by

$$\delta_\ell = A^2/\hbar v_\ell |F_1 - F_2|$$

A being the interaction constant, F_1 and F_2 the slopes of the potential curves and V_ℓ the radial velocity at the crossing point for the l^{th} partial wave.

Also β_ℓ is the phase change given by (see Fig. 2.6)

$$\beta_\ell = \int_{a_{2\ell}}^{b_{2\ell}} k_{2\ell}(r)\, dr. \qquad (30)$$

and ϕ_ℓ may be interpreted in terms of either of the adiabatic potential curves. If the upper curve is chosen, ϕ_ℓ is the phase integral between classical turning points for the upper curve and is given by

$$\phi_\ell \approx \int_{a'_{1\ell}}^{b'_{1\ell}} k_{+\ell}(r)\, dr. \qquad (31)$$

or if the lower curve is chosen, ϕ_ℓ is given by

$$\phi_\ell = \int_{a_{1\ell}}^{r_{1\ell}} k_{1\ell}(r)dr + \int_{r_{2\ell}}^{b_{2\ell}} k_{2\ell}(r)dr - \int_{r_{2\ell}}^{r_{1\ell}} k_{-\ell}(r)\, dr \qquad (32)$$

which is the difference in phase integrals between $r_{2\ell}$ and $r_{1\ell}$, associated with a change from motion governed by $V_1(r)$ and $V_2(r)$ to motion governed by $V_-(r)$.

β_ℓ, ϕ_ℓ, δ_ℓ and μ_ℓ and therefore C_ℓ are functions of the reduced energy ϵ_ℓ:

$$\epsilon_\ell = \frac{2\mu(E - V^\ell(r_x))}{\hbar^2} = 2\mu\left(E - V(r_x) - \frac{\ell(\ell+1)\hbar^2}{2\mu r_x^2}\right)\Big/\hbar^2 \qquad (33)$$

When ϵ_ℓ is sufficiently high i.e. for low values of L for a given relative energy E, then μ_ℓ is small. In this case the composite phase factor $C_\ell \exp(2i\eta_\ell)$ reduces to

$$C_\ell \exp(2i\eta_\ell) \approx \exp(2i\eta_\ell) \quad \text{for } \beta_\ell \neq (n+\tfrac{1}{2})\pi$$
$$\approx \exp[2i(\eta_\ell+\beta_\ell-\phi_\ell)] \quad \text{for } \beta_\ell=(n+\tfrac{1}{2})\pi$$

this latter exception occurring when the Bohr quantisation condition for a bound state of the ionic potential is satisfied. Thus in this high relative radial energy case, the system remains on the covalent curve $V_1^{\ell}(r)$ unless the energy is in resonance with one of the bound states of $V_2^{\ell}(r)$, when it switches over to the lower adiabatic curve.

At the opposite extreme when ϵ_ℓ is sufficiently low that $\mu_\ell \gg 1$ the composite phase factor in the typical case is given by

$$C_\ell \exp(2i\eta_\ell) \approx \exp[2i(\eta_\ell+\beta_\ell-\phi_\ell)] \quad \text{for } \phi_\ell \neq (n+\tfrac{1}{2})\pi$$
$$\approx \exp(2i\eta_\ell) \quad \text{for } \phi_\ell = (n+\tfrac{1}{2})\pi$$

Thus the phase shift is now determined by the adiabatic curve $V_-(r)$, unless the energy is in resonance with one of the bound states of the upper adiabatic curve, this giving rise to a switch to $V_1(r)$.

The number of partial waves affected by the coupling of states is limited to those whose classical turning points lie within the crossing point separation. Ignoring resonance contributions, the low L values in this range have a phase shift determined by the covalent potential. Whether the phases for the higher L values are determined by the covalent or adiabatic potential depends on the value of the interaction constant, A. If this is small, only a small number of high impact parameter collisions will be affected. This will show up first in the small angle scattering. As the constant A increases more and more values of L are affected and the range of angle influenced is widened. According to Barry (BER 57), the interaction constant for KI is

very weak so that it may be that the K - I scattering will be wholly determined by the covalent potential. On the other hand, if any of the high L value phases are affected, then the small angle scattering will be predominantly determined by the ionic curve.

Scattering Predictions for the Potassium - Iodine Atom System.

Referring back to Chapter I, the differential cross-section for elastic scattering was, according to quantum theory, written as

$$\sigma(\theta) = |f(\theta)|^2 \tag{34}$$

where $$f(\theta) = \frac{1}{2ik}\sum_{\ell=0}^{\infty}(2\ell+1)(e^{2i\eta_\ell}-1)P_\ell(\cos\theta)$$

so that $$\sigma(\theta) = \frac{1}{4k^2}\left\{\left(\sum_{\ell=0}^{\infty}(2\ell+1)(\cos 2\eta_\ell - 1)P_\ell(\cos\theta)\right)^2 + \left(\sum_{\ell=0}^{\infty}(2\ell+1)\sin 2\eta_\ell P_\ell(\cos\theta)\right)^2\right\} \tag{35}$$

The computer program, Monoenergy Forward, written by Cowley (COW 68) was used to calculate differential cross-sections in centre of mass and laboratory co-ordinates for a given model potential for orthogonal, monoenergetic beams. This calculates phase shifts by the JWKB method until η_ℓ is less than 0.1 radians, higher order phase shifts being derived using the asymptotic Born approximation.

In a real apparatus, however, the beam interaction region has a finite size, the beams have a measurable velocity distribution, and the detector subtends a finite solid angle at the scattering centre. The results of monoenergy forward are therefore not very useful for comparing theoretical predictions with experimental results. Accordingly, Cowley wrote a second program, DELILAH, which computes elastic differential cross-sections in the laboratory system averaged over the cross-beam velocity and angular spreads. The main beam is assumed unidirectional and monoenergetic. Again the JWKB and Born approximations are used to calculate the phase shifts but at

five equally spaced collision energies determined by the limits of integration over beam speeds and intersection angles. A complete set of phase shifts for any relative energy between the lowest and highest can then be obtained by interpolation. The integrals are evaluated by Gaussian quadratures, seven quadrature points on each integral being used. The results of these calculations, which still do not include the effect of a finite detector size, can then be compared with the experimentally observed results. Since only relative differential cross-sections can be measured, only the angular structure of the theoretical predictions is of interest and no attempt is made to normalize the distribution functions.

Using these programs theoretical differential cross-sections were computed for comparison with the experimentally observed curves. For the alakli metal-halogen atom case several interpretations are possible.

First of all, if the interaction constant between the 0^+ covalent state and the ionic state is small and if the covalent potentials have sufficiently similar parameters, the interaction might be describable by a single potential curve of the Lennard-Jones n - 6 type, with variable parameters n, well depth ϵ and equilibriumdistance, r_m. For K - I, Levi (LEV 34) has suggested a well depth of approximately 2×10^{-14} ergs while earlier calculations suggested a C_6 coefficient of around 1400×10^{-60} ergs. cm^6. Delilah was designed especially for such a calculation and the calculated small angle scattering pattern for these parameters is shown in Fig. 2.7. Such a potential also leads to rainbow structure at wider angles as the monoenergy calculation shows (Fig. 2.8.)

The next simplest explanation again confines the interaction to a single potential curve but this time assumes that the structure is due entirely to a single covalent curve switching to the ionic curve at the crossing point

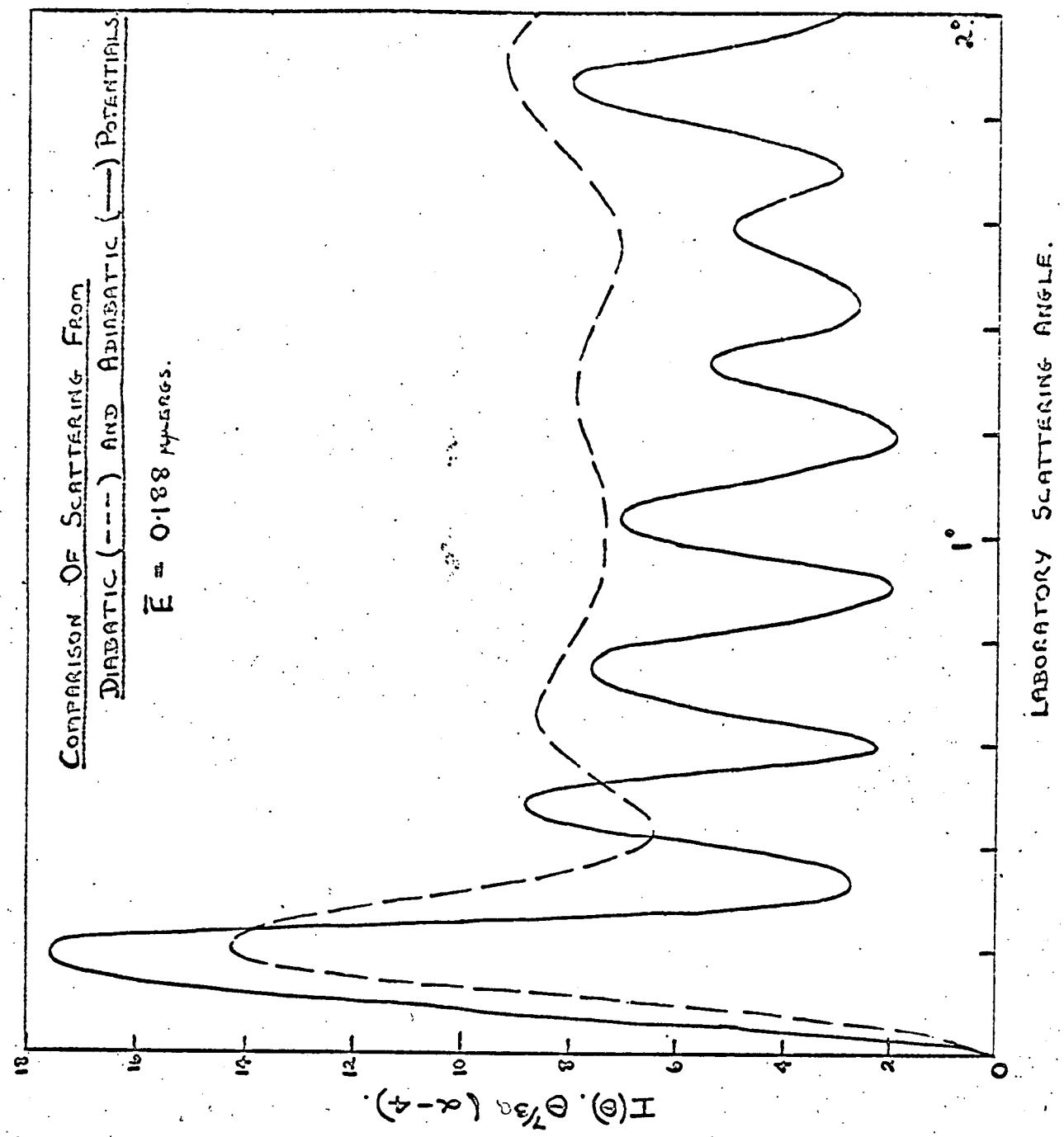

Fig. 2.7. Comparison of scattering from adiabatic and adiabatic potentials.

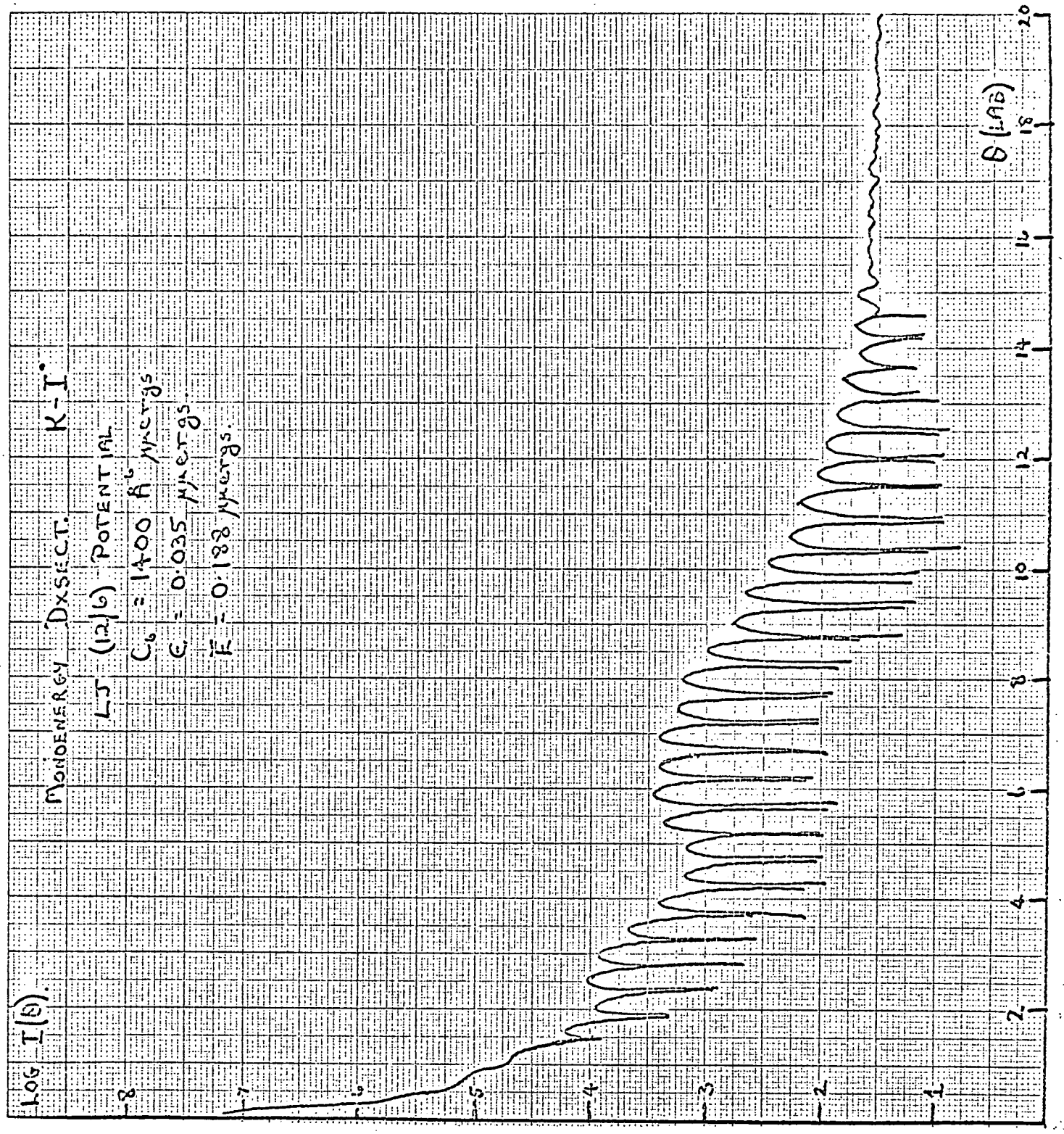

Fig. 2.8. Monoenergy cross-sections for K-I collisions.

separation. Such a situation could arise (i) if electron spin were not conserved and all the covalent curves were describable by a single set of parameters or (ii) if the interaction constant were large so that the 0^+ covalent curve switches to the ionic curve while the parameters of the other covalent curves were such as to give rise to no small angle structure.

To avoid a sharp discontinuity in the potential an interpolative switching routine was employed to smoothly change an LJ N - 6 potential to an ionic model over a region of variable width around the crossing point. This width was usually about 0.1Å and the Varshni-Shukla potential

$$V(r) = -\frac{e^2}{r} + P\exp(-kr^2)$$

was adopted as the ionic model. Monoenergy calculations showed that the small angle scattering pattern varied only slightly with the width of the switching region and the ionic model employed. This width implies an interaction constant of 0.007 μergs . The phase shifts associated with this deep potential well are large and show typical orbiting behaviour with a sudden discontinuity at an angular momentum, L*. The JWKB method of calculating phase shifts is inaccurate for this region but, since it occurs only over a small range of L, it is considered to have a minimal effect on the observable differential cross-section. Fig. 2.7. also shows the small angle differential cross-section for this adiabatic potential case. The main beam velocity and cross-beam temperature are the same in both cases. Points of difference to note at this stage are (i) the first peak is much closer to zero in the adiabatic case and (ii) the peak angular frequency is lower in the covalent case than in the adiabatic one.

Further interpretations involve combinations of these first two extreme

cases. Thus, as has already been pointed out, the interaction between alkali and halogen atoms can take place along several potential curves, only one of which involves the possibility of charge transfer at some value of R. The scattering arising from each of these is independent of any other and they add together in proportion to their statistical weights. This independence assumes the conservation of spin throughout. Thus depending on the type of coupling postulated, one may invoke three or four interaction curves, one of which could be the ionic curve arising from an adiabatic transition at the crossing point. In that case it is possible that the low weighting of the ionic curve would render its structure almost invisible within the peak patterns (if any) arising from the other curves. Moreover each potential has an independent choice of parameters so that the number of possibilities is increased markedly with a consequently smaller chance of being unambiguous in the interpretation. The small angle structure arising from a combination of two covalent potentials and the adiabatic potential weighted according to the jj coupling scheme is shown in Fig. 2.9. The individual patterns are also shown, giving some idea of how peaks are enhanced or washed out as the patterns move in and out of phase.

So far it has been assumed that the coupling between the states is such that the scattering is predominantly determined by one or other of the extremes. Should the interaction constant take some intermediate value, this particular collision process will have two coherent and interfering branches. In these circumstances it is difficult to give a simple expression for $f(\theta)$, though this has been done using an S - matrix formulation for the case where the inelastic channel is also open (MAT 69).

In summary therefore, the following models have been suggested for the K - I interaction

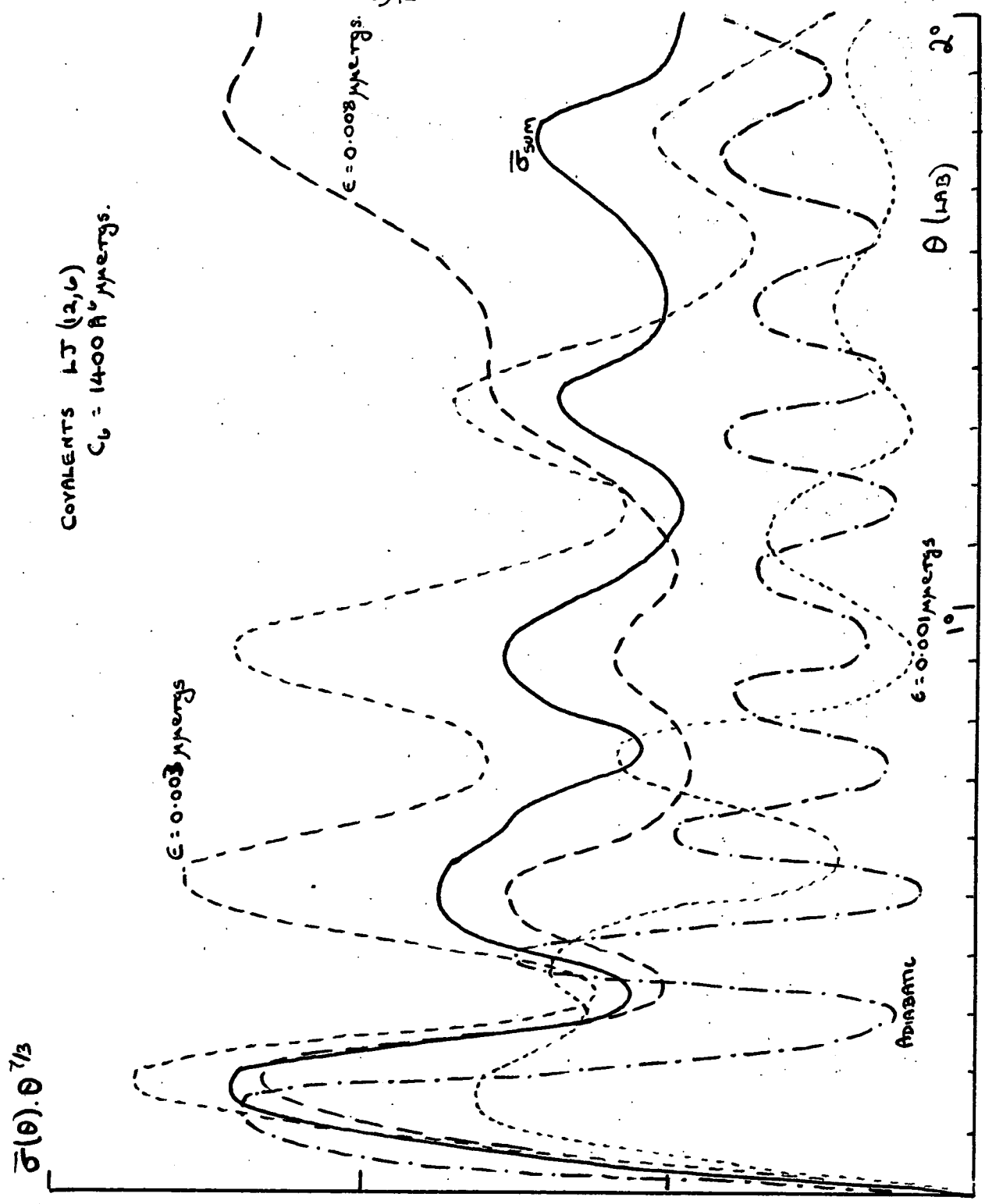

Fig. 2.9. Adiabatic plus covalent potential cross-sections weighted according to (jj) coupling.

(i) A single Lennard-Jones N,6 model with the parameters N, ϵ and r_m to be determined. Interaction Constant small.

(ii) A single potential switching from an LJ n, 6 to an ionic model at the crossing point. Large interaction constant.

(iii) A combination of several covalent potentials of the LJ type. Small interaction constant.

(iv) A combination of one or more covalent potentials with the switching potential. Large interaction constant.

(v) A situation where the interaction constant takes some intermediate value. In this case the scattering pattern may contain interference structure arising from the two coherent branches of the scattering amplitude. This model may be restricted to a two-state one, though further covalent interactions due to the different M_L and M_S states of the pair may be invoked if necessary.

It is also helpful at this point to specify the criteria which make a model acceptable. Position and frequency of peaks are useful in pinpointing possible candidates for the interaction model but the energy dependence of their pattern must also follow that of the experimental pattern. In this way models acceptable at one energy may be eliminated. Even so, such a fitting procedure, as outlined here, does not lead to a necessarily unique set of potential parameters. Other models, just as plausible, might also lead to the same results. Indeed at the end of the day, we may be left with a choice of two or three. It is then to be hoped that further observations of total cross-sections or wider angle scattering will lead to the elimination of some or all but one of these models.

An Expression for the Total Cross-Section Arising from a Screened Coulomb Potential.

Massey and Mohr (MAS 34) were the first to develop an approximate formula for the total cross-section appropriate for heavy particle scattering from an inverse s power dependence. Their expression for this was

$$Q_{mm} \approx P(s)\left[\frac{C^{(s)}}{\hbar v}\right]^{2/s-1} \qquad (36)$$

A somewhat more accurate derivation by Landau and Lifshitz yielded the same velocity dependence for Q but a slightly different expression for the function P (S).(LAN 59)

For the important case of S = 6, we have the result

$$Q = P_6\left[\frac{C^{(6)}}{\hbar v}\right]^{2/5} \qquad (37)$$

This implies that a log-log plot of Q (v) against v should be linear with a slope of - 0.4. That the influence of short-range repulsive forces causes undulations on this line is being neglected for the moment.

If the interaction between halogen atom and alkali were to follow an n, 6 potential then the total cross-section would be expected to exhibit the above behaviour. Should, however, the adiabatic curve be the interaction potential, then a completely different velocity dependence might be shown by total cross-section, though this may not occur in the thermal energy range.

If we approximate the ionic part of the potential by a screened Coulomb field

$$V(r) = \frac{2Ze^2}{r}\exp(-\lambda r) \qquad (38)$$

and assume that the Born approximation for the phase shift may be used over

the entire range of L, then η_ℓ may be written as

$$\eta_\ell = \frac{-\gamma Z e^2 \pi}{\hbar v} \int_0^\infty \left[J_{\ell+1/2}(kr) \right]^2 \exp(-\lambda r)\, d(kr) \qquad (39)$$

which leads to (WU 52)

$$f(\theta) = \frac{-2\gamma Z m e^2}{\hbar^2} \cdot \frac{1}{q^2+\lambda^2} \qquad q = 2k\sin\left(\frac{\theta}{2}\right). \qquad (40).$$

But the total cross-section for scattering from such an isotropic potential can be written as

$$Q = 2\pi \int_0^\pi |f(\theta)|^2 \sin\theta\, d\theta$$

so that substituting and integrating directly, after changing the variable to $\theta/2$ gives

$$Q = \frac{4\gamma^2 Z^2 m^2 e^4}{\hbar^4 \lambda^2} \cdot \frac{1}{4k^2+\lambda^2} \qquad (41)$$

Since $1/\lambda$ is of the order of 10Å and the wave number $k \gg 10$, the above expression may be approximated by

$$Q \propto \frac{1}{k^2}$$

i.e.

$$Q \propto v^{-2} \qquad (42).$$

Thus a log-log plot should have a slope of - 2 in marked contrast to the - 0.4 of the r^{-6} dependence. It now remains to be seen whether the range of the potential sampled by the total cross-section at thermal energies lies within the Coulombic region. This is most easily determined from the Massey-Mohr treatment assuming a covalent potential with an r^{-6} dependence.

The Massey-Mohr total cross-section is calculated over two regions of phase shift: (i) where $|\eta_\ell| > \frac{1}{2}$ and here the random phase

approximation is used to calculate the contribution from this region $0 < \ell < L^*$, L^* being the angular momentum quantum number for which $\eta_\ell = 1/2$. Thus $Q_{<L^*} \approx 2\pi L^{*2}/k^2$

(ii) for values of $\ell > L^*$ (where $\eta_\ell \leq 1/2$), the JB approximation is used for η_ℓ. For this region

$$Q_> \approx \frac{8\pi}{k^2} \int_L^\infty d\ell\,(\ell + 1/2) \sin^2 \eta_{JB} \approx \frac{8\pi}{k^2} \int_L^\infty d\ell . \ell . \eta_{JB}^2$$

$$\eta_{JB} \approx a_s \ell^{1-s}$$

where $$a_s \approx f(s)\, \mu\, C^{(s)} k^{s-2}/\hbar^2$$

so that $$Q_> \approx \frac{4\pi}{k^2} \frac{a_s^2}{s-2} L^{*4-2s} \approx \frac{\pi}{s-2} \cdot \frac{L^{*2}}{k^2}$$

The dependence of the total cross-section on the potential thus enters through L* i.e. the range of the potential which the MM total cross-section samples depends on the point of onset of the random phase region. Using the above expression for the JB phase shift and remembering $l + \frac{1}{2} = kb$, the range of potential sampled at any given velocity is supplied by the condition

$$\frac{0.5288\, C_6}{\hbar v b^{*5}} = \frac{1}{2} \qquad (43)$$

Thus $b^* \gtrsim 10$Å when v, the relative velocity is approximately 2×10^4 cm. sec^{-1}. Also when $v \gtrsim 5 \times 10^5$ cm. sec^{-1}, the range sampled is only reduced to 6Å. Hence for our experimental range of energy, the Massey-Mohr total cross-sections would be sampling a covalent potential range of 8 to 10Å which is well within the K - I crossing point. In other words b* passes into the

Coulombic region below our energy range so that the total cross-section for the adiabatic curve will show its v^{-2} dependence within the thermal energy range.

As far as the sodium/iodine atom case is concerned, the crossing point here lies at approximately 7Å while the C_6 coefficient is approximately half the K - I value. This range is not sampled until just outwith the experimental energy range so that thermal energy total cross-sections in the Na / I system will be governed solely by the covalent regions of the potential and the log-log plot will show a -0.4 dependence whether or not switching occurs.

Scattering Predictions for the Potassium Iodine Molecule Case.

The scattering of potassium from molecular iodine is complicated by the possibility of chemical reaction though the molecular energy state build up is simpler than that of K/I. Thus there are no spin or angular momentum restrictions forbidding the partners from entering the ionic state. The wide angle reactive scattering has been the subject of several investigations (MIN 66, BIR 67, ROS 69) but so far the elastic scattering has not been fully investigated for any angular range. No rainbow structure has ever been observed in any of these studies and this is taken to mean that for distances of closest approach about equal to the distance of the potential minimum, chemical reaction takes precedence over elastic scattering.

Dynamics of Collisions. In a binary collision the conservation laws of energy and linear and angular momentum are often particularly helpful in understanding microscopic features of both reactive and non-reactive scattering. If E is the initial kinetic energy of relative motion of the reactants, Z the associated internal energy (rotational, vibrational or electronic) and ΔD_o° the difference in dissociation energy of products and reactants, then the final kinetic energy of relative motion of the products E' and the internal energy of the products are given by

$$E' + Z' = E + Z - \Delta D_o^\circ \qquad (44)$$

The direction of the centre of mass velocity vector, the centroid, is given by

$$\theta_c = \tan^{-1}\left[\frac{m_{x_2} v_{x_2}}{m_m v_m}\right] \qquad (45)$$

Fig. 2.10. is a vector diagram of initial and final velocities in a binary collision involving mutually perpendicular initial velocity vectors. In the case of an elastic collision where Z' = Z and $\Delta D_o^\circ = 0$. we have the familiar result that E' = E or its equivalent $|\underline{v}_r'| = |\underline{v}_r|$. For inelastic or reactive collisions, however, the magnitude of v_r' is restricted

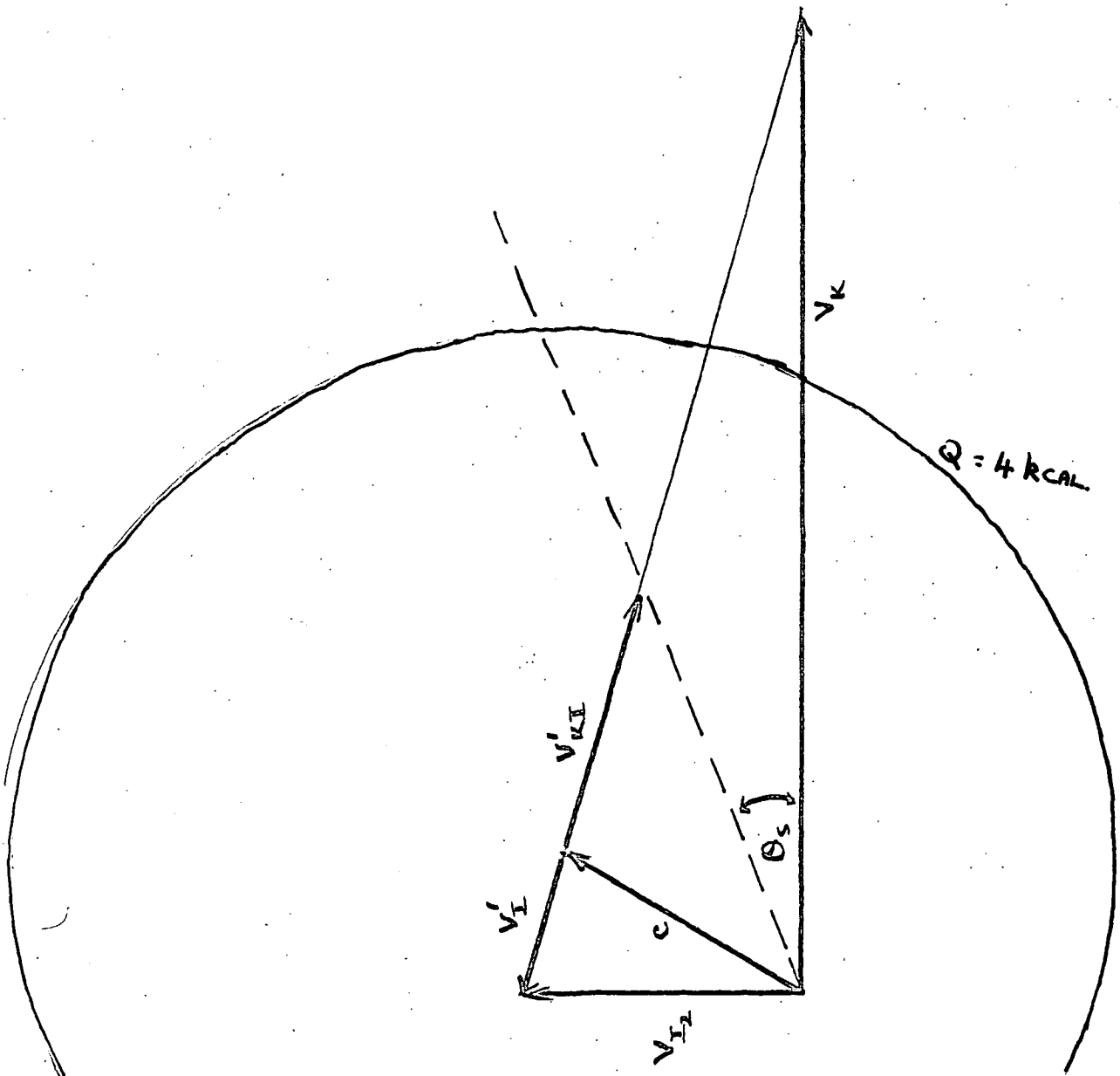

Fig. 2.10. Diagram for spectator stripping in the K + I system. The recoil vectors v'_I and v'_{KI} are restricted to fall on the relative velocity vector v_r and the products are found at 90° and θ_s respectively in the lab. system. Q_{KI} are the envelopes of recoil velocity vectors of the product KI for the Q given.

to

$$v_r' = \left[\frac{2(E_R + E')}{m_{mx}(1 + m_{mx}/m_x)} \right]^{1/2} \qquad (46)$$

where E_R is the initial relative energy and E' is defined by equation 2.44. above. The circles in Fig. 2.10. indicate the length of recoil velocity vectors for KI produced with various amounts of final relative translational kinetic energy.

The K - I_2 reactive scattering has been interpreted using the elastic spectator model. In this method the electron transfers from the alkali atom to an atom of the halogen molecule. The X^- ion is hauled off by the Coulomb force, the other halogen atom merely spectating. Since the model assumes that this unreacting halogen is unaffected, this product X atom must be found at 90° in the LAB co-ordinate system. The product MX is found at an angle θ_s given by

$$\theta_s = \tan^{-1}\left[\frac{m_x v_{x2}}{m_m v_m} \right] \qquad (47)$$

which angle Birely et al (BIR 67) finds equal to 20° i.e. the product KI distribution is observed peaked at 20° in the LAB system.

Analysis of Scattering. Reactive molecular collisions may be studied via the differential cross-section for the elastic scattering of the reactants using the proceudre known as the "optical model". (BER 66, ROS 67, BER 68, MAR 69). In this model the interaction potential is assumed complex

$$V(r) = V_o(r) + iW_o(r) \qquad (48)$$

with the imaginary part added to represent absorption due to reaction. Such a complex potential implies complex phase shifts and these may be written as

$$\eta_\ell = \eta_\ell^\circ + i\,\varepsilon_\ell \qquad (49)$$

In terms of the S-matrix formulation (MOT 65) the quantal differential cross-section may be represented as

$$f(\theta) = \frac{1}{2ik}\sum_{\ell=0}^{\infty}(2\ell+1)(S_\ell - 1)P_\ell(\cos\theta) \qquad (50)$$

where $S_\ell = \exp(2i\eta_\ell)$ and k is the incident wave number.

We have (BER 66) for the total elastic cross-section

$$Q^{el} = \frac{\pi}{k^2}\sum_{\ell=0}^{\infty}(2\ell+1)|1 - S_\ell|^2 \qquad (51)$$

for the total non-elastic (i.e. both reactive and inelastic) cross-section

$$Q^{in} = \frac{\pi}{k^2}\sum_{\ell=0}^{\infty}(2\ell+1)\left[1 - |S_\ell|^2\right] = \frac{\pi}{k^2}\sum_{\ell}(2\ell+1)\,p_\ell \qquad (52)$$

where $p_\ell = 1 - |S_\ell|^2 = 1 - \exp(-4\varepsilon_\ell)$ is the "opacity function." and for the total cross-section

$$\begin{aligned} Q^{tot} &= Q^{el} + Q^{in} \\ &= \frac{\pi}{k^2}\sum_{\ell}(2\ell+1)\left\{1 - |S_\ell|^2 + |1 - S_\ell|^2\right\} \qquad (53) \\ &= \frac{2\pi}{k^2}\sum_{\ell}(2\ell+1)\left[1 - Re\,S_\ell\right] = \frac{4\pi}{k}\cdot Im\,f(0). \end{aligned}$$

Also the differential cross-section in this optical model treatment is given by

$$\sigma(\theta) = \frac{1}{4k^2}\left\{\left(\sum_{\ell=0}^{\infty}(2\ell+1)P_\ell(\cos\theta)\left(1 - \exp(-2\varepsilon)\cdot\cos 2\eta_\ell\right)\right)^2 + \left(\sum_{\ell=0}^{\infty}(2\ell+1)P_\ell(\cos\theta)\exp(-2\varepsilon)\cdot\sin 2\eta_\ell\right)^2\right\} \qquad (5$$

So that in terms of the opacity function, p_ℓ,

$$\sigma(\theta) = \frac{1}{k^2}\left\{\left(\sum_{\ell=0}^{\infty}(2\ell+1)\sin 2\eta_\ell(1-p_\ell)^{1/2}P_\ell(\cos\theta)\right)^2 + \left(\sum_{\ell=0}^{\infty}(2\ell+1)\left[\cos 2\eta_\ell(1-p_\ell)^{1/2}-1\right]P_\ell(\cos\theta)\right)^2\right\} \tag{55}$$

The procedure now is to postulate some parametrized form for p_ℓ, the opacity function, which can be assumed to reflect the imaginary part of the equivalent potential (which accounts for reactive scattering.) In this function if we set $\varepsilon = 0$, then we define a collision problem analogous to that being studied save for the absence of reactive scattering. Thus when $\varepsilon \doteq 0$. the equation for $\sigma(\theta)$ above will yield the differential cross-section for pure elastic scattering for this reference problem.

Some calculations were carried out for the K - I system using an LJ (12,6) potential with what were thought to be appropriate parameters. C_6 was calculated using the Slater - Kirkwood formula as 1400×10^{-60} ergs cm.^{6} with ε, the well depth taken as 0.02 $\mu\mu$ergs. The real phase shifts, were computed using the JWKB approximation for $\eta_\ell^\circ > 0.1$ rad., higher order phases being computed using the Jeffreys - Born approximation.

The opacity function was assumed to be off the form

$$p_\ell = 1 - \exp(-4\varepsilon_\ell)$$
$$\text{with} \quad \varepsilon_\ell = A\left\{1 + \exp\left(\frac{\ell - L^*}{\Delta L}\right)\right\}^{-1} \tag{56}$$

and is shown in Fig. 2.11. As can be seen this allows an appreciable

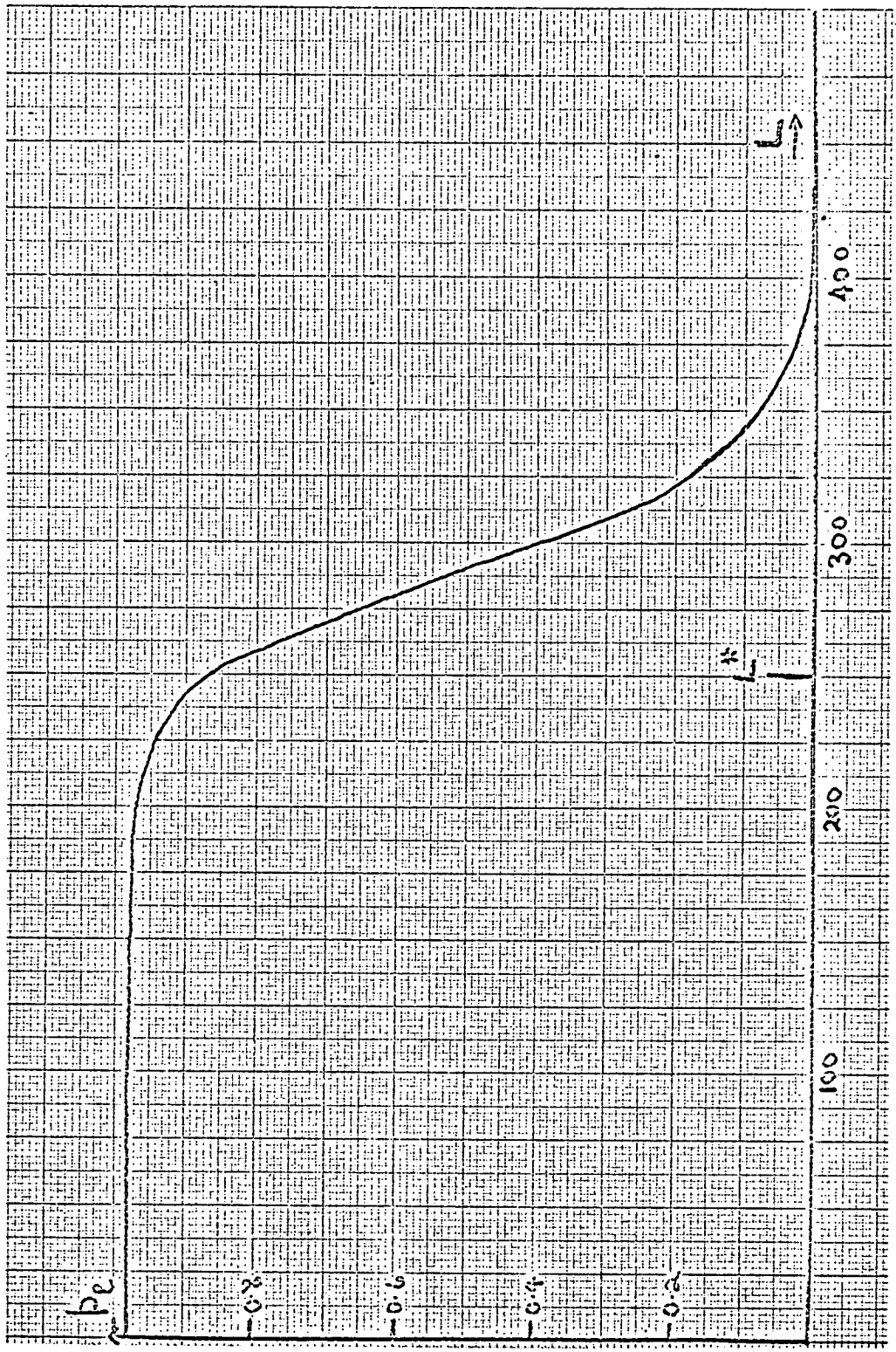

Fig. 2.11. Opacity function for optical model.

amount of reactive scattering for $L > L^*$ as well as allowing some elastic scattering at lower L values.

The case of $\Delta L = 1$ corresponds to the step function

$$p_\ell = A \qquad \ell < L^*$$

$$p_\ell = 0 \qquad \ell > L^*$$

Bernstein and Levine (BER 68) have shown that this sharp cut-off introduces spurious oscillations and so this case was not considered.

The differential cross-sections were computed at 0.1° intervals using the relation given in equation 2.55 and the result plotted as $\sigma(\theta).\theta^{7/3}$ to reveal the quantum oscillations more clearly. A sample set of results for a collision energy within our experimental range is shown in Fig. 5.35.

The reference curve, with $\varepsilon_\ell = 0$ is plotted with symbol $\square$, and shows the expected oscillatory structure, with both a high and a low frequency. The curve with symbol $\times$ is that obtained using our probability function with $\Delta L = 25$ and L^* equivalent to an impact parameter equal to R_c, the crossing-point radius i.e. we assume that reaction predominates after the crossing point is reached. As can be seen from the graph, the low frequency oscillations corresponding to low impact parameter interactions are removed but the higher frequency ones still remain though somewhat attenuated. When the value of L^* is doubled (graph $\diamond$) the quenching of elastic scattering is increased and even the higher frequency oscillations are almost obliterated, only the very low angle peaks remaining.

One would expect that reaction could occur for $L > L^*$ as well as not occurring for $L < L^*$. These latter effects are allowed for in our model by use of a "diffuse" boundary. One peculiarity of our function is its

asymmetry about L^*, allowing more reactive scattering for $L > L^*$ than elastic for $L < L^*$. The probability function is also grey in that it allows a certain amount of elastic scattering to take place for all L within the reactive sphere. This latter scattering takes place on the LJ potential curve. Interpreting our results on the 'harpooning' model of Herschbach (HER 66), we might also postulate that not all electron transfer led to reaction products. In this case the alkali metal could regain its electron after interacting with the iodine along a Coulombic type of potential curve, thus giving another form of elastic scattering.

Thus a study of the optical model's predictions for small angle elastic scattering could reveal features of the reactive scattering probability function. However, it may be that the introduction of extra parameters in the various functional forms of p_ℓ, coupled with the possibility of two 'elastic' potentials may only serve to increase the ambiguity of the interpretations rather than help to clarify an already complicated situation.

CHAPTER III

ATOMIC BEAM SOURCES.

INTRODUCTION

The main requirements of an atomic beam source are stability and efficiency. Stability is important since runs may last for up to two days. High efficiency is also necessary since the presence of the parent molecule in large quantities will only confuse the analysis of any scattering pattern obtained. It is also desirable that all the atoms should be in the same electronic state.

Jennings (JEN 61) has reviewed the production of atoms, in general. From the methods listed therein, only the following satisfy the above criteria.

(i) Electrical discharges

(ii) Thermal dissociation.

All other methods fail on one or both counts. Thus photolysis produces too low a concentration of atoms while shock tube methods give very high but transient concentrations.

(i) Electrical Discharges. These produce high concentrations of atoms at pressures up to 15 torr, above which the discharge goes out.

Three main types have been used to produce atoms.

(a) The low frequency electrode discharge or Wood's tube.

(b) The radio frequency or electrodeless discharge, operating at a frequency of a few megacycles.

(c) The microwave discharge which operates at a frequency of 2500 - 3000 megacycles.

The earliest system due to Wood (WOO 20) consisted of a U-tube one to two metres long, the gas being admitted through the arms and being withdrawn from the middle. The discharge occurs between aluminium electrodes situated inside at the ends of the arms. Though the main disadvantage of this type of source is its size, an other factor working against it is contamination of the beam by

electrode material.

The problem of this attack on the electrodes can be obviated by use of the radiofrequency 'electrodeless' discharge which also has the advantage that no special discharge tube is required. The electrode assembly outside the tube may consist either of two electrodes wrapped round the tube (capacitative coupling) or of a coil of several turns of copper wire wound round the tube (inductive coupling). The power is supplied from a radiofrequency generator operating between 1 and 30 MHz with a power output up to 200 watts. So far as is known, no systematic studies have been made of the factors which influence the yield of atoms produced by an r.f. discharge.

Microwave discharges, operating at 2500 to 3000 MHz with power inputs of several hundred watts are the most recent developments in discharges. Usually triggered with a Tesla coil, the discharge is generated inside a quartz tube passing through a tunable resonant cavity coupled to a waveguide leading from a microwave source.

(ii) Thermal Dissociation. Temperatures in excess of 2000 °K are difficult to obtain, and consequently it is necessary for a molecule to have a fairly low dissociation energy if appreciable atom yields are to be obtained. Nevertheless hydrogen atom beams of 'good' intensity have been produced by thermal dissociation in a tungsten tube heated electrically to 3000 °K (MAR 66). The supplying of power to a device like that and the cooling of its surroundings makes it impossible to use in the present thermal beam set-up. However, it is possible to design a thermally dissociating source for 'weakly' bonded diatomics such as the halogens. Thus Beck (BEC 68) uses a thermal bromine atom source which gives 40% dissociation at 1450 °K.

There were therefore two methods available for efficiently producing a stable beam of atoms. The final choice of method had to be governed by its

suitability for use in dissociating the chosen molecule within the confines of an existing apparatus. Each method was considered in the light of these overriding factors.

At first, since the planned experiments were to be studies of the reactive scattering of chlorine atoms from several hydrocarbons, the requirement was for a chlorine atom source. Preliminary thermodynamic calculations showed that, for source pressures in the region of one torr, a temperature of 1600°K would be required to give 90% dissociation, whereas equally high levels of dissociation could be produced in halogens and other diatomics in a high frequency discharge. Thus it was decided to build a chlorine atom discharge source, but which type - microwave or radiofrequency.

Both types have been used to produce the following atoms in the presence of their parent molecules: hydrogen, oxygen, nitrogen and the halogens. Table 3. 1. sums up the yields so obtained.

From the point of view of percentage dissociation, therefore, microwave discharges seemed to have the edge on r.f., though this appeared to depend strongly on the efficiency of coupling of power into the system, something which is extremely difficult to measure in an r.f. discharge. As a summary of the confusion which exists in the results above we may cite the following. Both using microwave, Greaves and Linnett (GRE) quote lower H-atom yields than Shaw (SHA). This could be due to their lower power availability, i.e. more power higher dissociation. The results of Clyne and Thrush (CLY 63) using r.f. appear to be characterized by singularly low yields. Linnett's (LIN56) yields are higher though his r.f. generator is of lower power. Does this mean that atom yield decreases as power input decreases (in contradiction to the previous statement) or does it simply mean that Linnett had a more efficient coupling of power into his system. The latter seemed a more reasonable conjecture.

Gas.	% Dissoc.	Power (Watts)	Frequency. (MHz)	Pressure. mm. Hg.	Reference.
Hydrogen	90.	100	3000	0.5	Shaw.
	Not quoted	50	2927	3 - 48	Greaves & Linnett
	¼ - 1	350	18	2	Clyne & Thrush.
	½ - 5	350	18	0.8 - 4	do.
Oxygen		70	2 - 6	0.05 - 2	Linnett & Marsden
	½ - 5	350	18		Clyne & Thrush.
Nitrogen	½ - 2	350	20	1.26 - 6.32	do.
	¼ - 1		18		
Halogens. Cl.	8 - 18			0.2 - 0.7	Rod. & Kling.
	60	50	3000		
	up to 100	100	2450		Ogryzlo.
I/Br.	80 - 100		450		Garvin, Green & Lipworth.

TABLE 3.1.

There was, however, no doubt that in both microwave and r.f. discharges the atom yield varied with both gas pressure and power input.

Another point to note is that Ogryzlo's high yields (OGR 61) were achieved only after he coated the inside of his discharge tube with an axyacid. None of the others tried this, though they noted in some cases (GRE 59) that 'wet' gases gave higher dissociations under comparable power and pressure conditions. The addition of contaminants to a gas is not, however, a good idea in a beam experiment.

Power inputs on both units are variable so that no advantage is to be gained with either discharge, though high inputs with r.f. tend to spread the discharge. The critical point is coupling this power into the actual discharge. It is generally acknowledged that this is relatively easy to achieve in a microwave cavity which is accurately resonant and with the discharge tube correctly positioned. Difficulty is, however, encountered in tuning the cavity to the load placed upon it. The fixed frequency means that the actual cavity lid or base has to be mechanically moved, an almost impossible operation on a moving source within a vacuum chamber. The coupling of an r.f. power input is generally acknowledged to be much more difficult but here the frequency is variable and the circuit can be tuned to the load.

The microwave discharge is generally initiated by holding a Tesla coil in the vicinity of the discharge tube. Unless such a coil was a built-in fixture on the source mounting, there would be no way of reaching the discharge in the vacuum system. R.F. discharges require no special means of initiation.

Now as to pressure range, Jennings (JEN 61) seems to think that r.f. discharges work better at lower pressures. His evidence seems to be based

solely on the work of Greaves and Linnett who found that a microwave discharge could be sustained in hydrogen only over the pressure range 3 - 48 mm. Hg., this with a power input of 50 watts. This is in direct contrast to Shaw who obtained a maximum of 90% dissociation in H_2 at 0.5 torr, though his power input was 100 watts. With r.f. discharges the minimum pressure is probably lower than for microwave and the maximum pressure is not known. But again, the pressure range probably varies with power input so that neither discharge gained any advantage from this point.

Another difficulty to be overcome especially with microwave is getting the power to the cavity of discharge tube. With r.f. a fairly thin shielded cable is all that is required, whereas with microwave either a vacuum tight waveguide (yet a flexible one since the oven was to be on a turn-table) or a coaxial cable is the answer. The waveguide appeared highly impracticable and a coaxial cable for microwave was thought to be rather thick and hence fairly inflexible.

To sum up, the r.f. discharge was chosen as a chlorine atom source for the following reasons.

The microwave discharge's fixed frequency raised two problems. First the fixed size of the cavity could give space problems and secondly the problem of mechanically tuning the cavity to give optimum power input. There were also the problems of initiating a microwave discharge without a Tesla Coil and of introducing the microwave power to the cavity.

THE RADIO FREQUENCY DISCHARGE SOURCE.

(i) Atom Production Mechanism. The generally accepted picture of the dissociation process in a low pressure gaseous discharge postulates a swarm of electrons moving through the gas under the influence of an applied electric field (MAS 52).

In the positive column of a d.c. discharge or in the plasma of a high frequency discharge, Fite (FIT 67) has shown that the velocity distribution of the electrons is that known as the Druyvesteyn distribution whose dependence on speed is given by

$$f(v)dv = v^2 \exp\left(-3hv^4/8\lambda^2 a^2\right) \qquad (1)$$

where $h = 2m/M$ (m = electron mass, M = heavy particle mass)

λ = mean free path.

$a = \left(\frac{q}{m}\right)E$ (q = electron charge, E = Electric field)

This distribution function is similar in shape to the Maxwell-Boltzmann distribution for a given mean speed, except that the most probable speed is slightly higher and the high energy tail is diminished in the Druyvesteyn distribution. Nonetheless, the distributions are sufficiently similar that one can, in the Maxwellian sense, define an electron temperature which is characteristic of the mean energy of the electrons. This electron temperature depends upon the ionization potential and pressure of the gas and is very large compared with the temperature of the gas. For example, in a low pressure discharge, Fite feels it is doubtful if the gas temperature is very much higher than 500 $^{\circ}$K compared with an electron temperature of perhaps 50,000 $^{\circ}$K. It is this disparity in temperature which is perhaps the most striking of the non-equilibrium aspects of a gas discharge.

The majority of electrons arise from ionizing collisions in the discharge. To sustain the discharge, the rate of electron production must balance the rate of electron loss.

Chief among the electron production mechanisms is simple electron impact ionization.

$$e + A \rightarrow 2e + A^+ \qquad (2)$$

where A is a groundstate neutral molecule or atom.

Electron loss processes are more numerous. Among the more important are diffusion to the walls of the discharge tube, dissociative recombination of electrons and ions ($e + AB^+ \rightarrow A + B$)and dissociative attachment to form negative ions ($e + AB \rightarrow A + B^-$). Numerous processes, however, operate to liberate the electron from the negative ion, among these being photodetachment ($h\upsilon + B^- \rightarrow B + e$), associative detachment ($A + B^- \rightarrow AB + e$) and electron impact neutralization ($e + B^- \rightarrow 2e + B$)

Other, probably negligible, loss processes are three body recombination with an electron as the third body i.e. $A^+ + e + e \rightarrow A + e$. and radiative recombination $e + A^+ \rightarrow A + h\upsilon$.

Thus dissociation by means of electron molecule collisions may be the direct result of electron impact or may occur indirectly as, for example, by the production of a metastable particle in the primary electron molecule collision with dissociation following a secondary encounter between the metastable and the neutral molecule. Production of a neutral atom may also follow initial formation of an ion via an electron induced transition from the ground state of a molecule to an unstable level.

Despite the wide use of the electrical discharge for dissociation, except with regard to hydrogen, very little progress has been made in working out the details of the dissociation process. For hydrogen, use has been made of a theory due to Emeleus (EME 36) and Lunt and Meek (LUN 36). According to this theory, the number of electronic excitations leading to the dissociation of molecules into atoms is directly proportional to the number of electrons supplied to the discharge, for conditions such that the density of undissociated molecules is effectively a constant. In both the d.c. and the high frequency discharge plasmas, for a given pressure, the electric field

intensity is essentially constant and independent of discharge current. Thus, for a discharge operating at constant pressure, a linear relationship is found between the rate of radical production and the power input to the discharge at very low power levels for which the density of undissociated molecules is practically a constant. Data for hydrogen given by Shaw (SHA 59) for the production of H atoms in both d.c. and high frequency discharges at low power levels bear this out.

A more recent study has been that of Jansson and Middleton (JAN 67) into the production of nitrogen atoms in a microwave discharge. They conclude that N-atoms originate primarily from thermal dissociation of the neutral gas which has been heated by random electron collisions. In drawing this conclusion they consider the dissociative recombination of N_2^+, N_3^+ and N_4^+ ions as the only other means of producing nitrogen atoms, neglecting excitation processes and dissociative attachment in forming negative ions as well as other negative ion processes. Jansson and Middleton also have a low percentage dissociation so that their conjectures concerning the neutral molecule temperature could be tested by forming a beam from the discharged gas and measuring the beam velocity distribution through a calibrated velocity selector.

(ii) Experimental

The radio-frequency oscillator was an unmodified transmitter with a frequency of 27 MHz and a power output over four levels with a nominal maximum of 200 watts. This set was supplied by Wolfendale Electronics Ltd., Bournemouth.

All testing of the source was carried out in a test chamber built from six inch diameter glass X and T pieces supplied by Quickfit. The pumping system used a Leybold DPL 150 oil diffusion pump backed by an S12 single stage

rotary pump, also Leybold. Cryogenic pumping in the neighbourhood of the source was provided by a specially designed liquid nitrogen cold trap. During a run the pressure was typically 5×10^{-7} to 2×10^{-6} torr, as measured by a Leybold ionization gauge.

The molecular beam was detected by means of an EAI Quad 250 mass filter employing electron bombardment ionization followed by quadrupole mass selection. Currents were measured on a Keithley 610B electrometer and recorded on a Servoscribe RE511 chart recorder. Gas line pressures for source gases were measured on an Edwards Model 9 Pirani gauge and all pressures given are uncorrected readings from this instrument.

Initial tests were carried out on the end of the gas line which was later used to supply the source. These showed that, in air, capacitative coupling gave a discharge over a longer pressure range than inductive coupling. The pressure range generally started about 0.4 - 0.6 torr extending to 3 - 7 torr depending on power input and electrode configuration.

The final electrode design and the source itself are shown in Fig. 3.1. The discharge tube was of $\frac{1}{2}$" o.d. pyrex glass, the mounting and supports being of aluminium and stainless steel. The earthed wire mesh screen as well as earthed screening on all r.f. leads were found to be effective in cutting down the interference of the discharge with other electronic equipment notably the mass filter. The source had a single slit 10 thou. wide by $\frac{1}{8}$" high.

Performance.

Preliminary tests of the discharge source were carried out with hydrogen, oxygen and carbon tetrachloride before the dissociation of chlorine was attempted by this method.

Hydrogen. First attempts to produce an H-atom beam from the discharge source

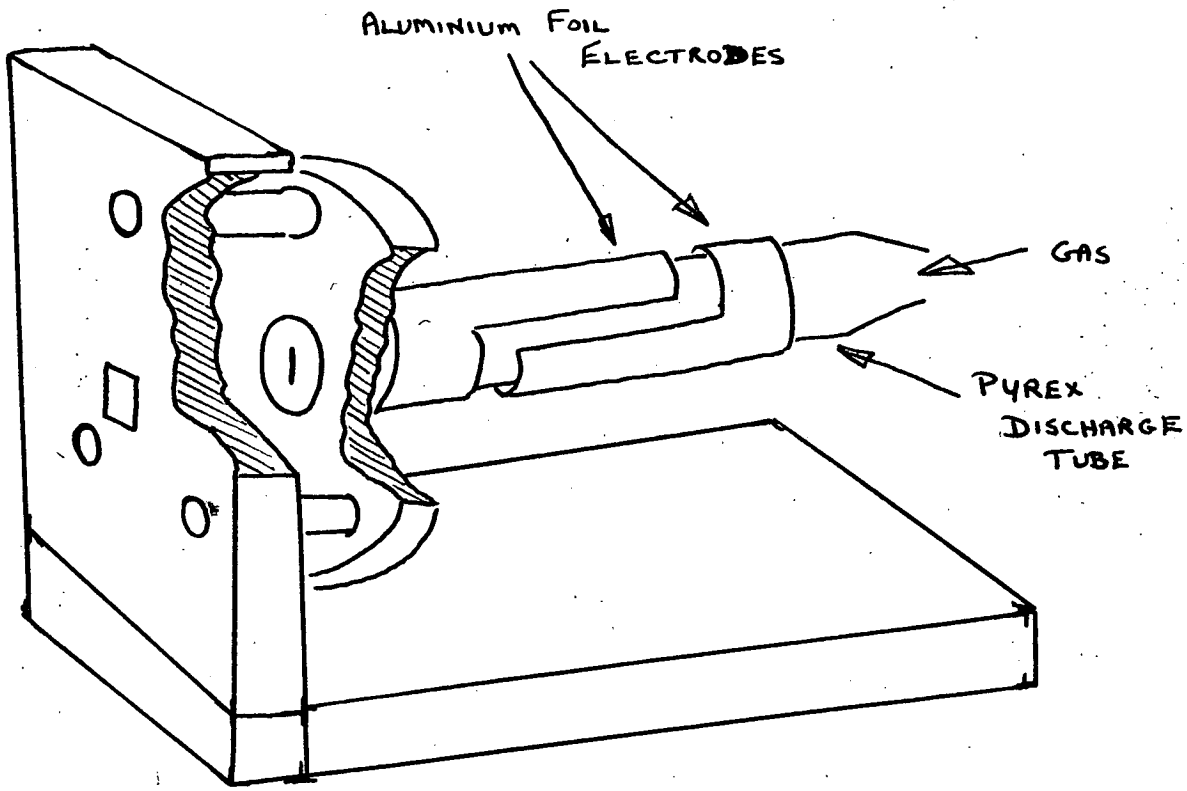

Fig. 3.1. Radiofrequency Discharge Source.

were singularly unsuccessful with either no dissociation or such a small percentage as to be undetectable as a change in the H^+ or H_2^+ ion signals.

Tests were then carried out using hydrogen poisoned with from 3 to 25% water, since this technique had been found efficacious in producing high dissociations (SHA 59). At most these succeeded in doubling the H^+ signal but no detectable change was observed in the H_2^+ signal. That this should be so is not too surprising. The cracking pattern observed for the hydrogen molecule was $H^+ : H_2^+ :: 1.5 : 100$. If it is assumed that the probability of ionizing a hydrogen atom is the same as that for producing a proton from an H_2 molecule, than the observed increase in signal represents less than 1% dissociation.

In a blank experiment with H_2O alone, the discharge resulted in a significant amount of OH radicals being created as well as removing 80% of the H_2O molecules from the original beam. Taking into account the removal of H_2O, the OH^+ signal was increased by a factor of 3. A similar increase was observed in the O^+ signal, but an overall decrease occurred in the H^+ ion current, only a small percentage of this not arising from the reduced H_2O flux. This small portion must arise from either H atoms in the beam or from OH radicals. Since the creation of an OH radical also gives an H atom, the low H^+ current must be attributed to the much lower ionization probability of an H atom compared to an OH radical or to the recombination of H atoms to molecular hydrogen. Unfortunately no attempt was made to detect any molecular hydrogen in the beam during this experiment.

Oxygen. With the source pressure at one torr, a blue colour was observed on switching on the discharge in oxygen. This changed to pink over a period of minutes. The O^+ signal increased from $0.9\alpha - 7$ amps to $1\alpha - 7$ amps with the discharge on, while the O_2^+ signal decreased to $5\alpha - 7$ amps from $9\alpha - 7$ amps.

If the decrease is attributed to removal of O_2 by dissociation, this means a 45% efficiency. Addition of H_2O to the oxygen did not produce any significant increase in the percentage dissociation achieved.

Carbon Tetrachloride. With the r.f. generator on full power, an intense light blue discharge was obtained with carbon tetrachloride. Table 3.2. below gives the ion currents for the various ions produced from the beam molecules.

TABLE 3.2.

Effect of R.F. discharge on CCl_4

	Discharge Off (α - 8 amps)	Discharge On (α - 8 amps)
Cl^+_{35}	0.5	4.5
CCl^+	Not measured	
CCl^+_2	2.2	0
CCl^+_3	9	0
CCl^+_4	0	0
C^+	Not measured.	

Before the CCl^+ and C^+ ions currents could be measured the transmitter burned out. Tests were not resumed after it was repaired.

In view of the fact that no CCl^+_3 or CCl^+_2 ions are seen when the discharge is on, it seems safe to assume that there are no parent CCl_3 or CCl_2 radicals present in the beam under these conditions. There may, however, be CCl radicals or carbon atoms and these could prove troublesome should discharging carbon tetrachloride ever be used as a means of producing a chlorine atom beam.

The corresponding fluorine compound, CF_4, has been used in a microwave

discharge to produce a fluorine atom beam, where, of course, problems with handling the diatomic are much intensified, (POL 69). There are, as yet, however, no details available on the performance of this source.

In all the above and succeeding cases no ions were ever observed in the beam emerging from the source with the discharge on. This was checked using a pair of deflector plates situated in front of the source slits and $\frac{1}{2}$ inch apart. No change in ion current was observed when 250 volts was applied to the plates, this being more than sufficient to deflect any ions from the beam before the detector was reached.

Chlorine. With the same design of electrodes as previously, a series of runs was carried out to determine the variation of the degree of dissociation with source pressure and power input. From the graphs shown in Fig. 3.2. it can be seen that the degree of dissociation exhibited a shallow maximum on all four power ranges in the pressure range 0.7 to 0.8 torr. Increasing the input power available also increased the dissociation efficiency. The error bars are intended to give some idea of the reproducibility of the source on different days.

To try to achieve optimum coupling of power into the discharge, the electrode spacing along the discharge tube was varied. This did little, however, and under the optimum conditions the maximum dissociation was raised to 27% on high power.

In view of the disappointing dissociation efficiencies achieved, it was decided to treat the inside of the discharge tube in the manner recommended by Ogryzlo (OGR 61). Because the stability of such treatment had been previously called in question (JEN 61), such a coating procedure had not been used so far.

Following Ogryzlo's recipe the discharge tube was:-

(i) Soaked for one hour in hot, concentrated caustic soda.

(ii) Rinsed several times in distilled water.

(iii) Left to stand for thirty minutes in a 10% solution of H_3PO_4.

After this the discharge tube was drained, returned to its mounting in the test stand and the chamber pumped down.

This treatment was eminently successful, though the discharge tube seemed to show symptoms of an aging process. In the first run of dissociation v. pressure, the maximum dissociation achieved was 50% between 0.65 and 0.7 torr, whereas in the second run, the discharge dissociated more than 90% of the Cl_2 molecules at 0.5 - 0.4 torr. (See Fig. 3.3.)

Keeping the pumps running, the discharge tube was left in the test stand for three days after which the same levels of dissociation were achieved. The coating therefore seemed stable and gave reproducible results.

The degree of dissociation was always measured from the relative heights of the Cl_2^+ (70) peaks with the discharge off and the discharge on. Though the chlorine atom peaks were checked to see that in fact their net height was affected by the discharge, no attempt was made to use these measurements in determining the degree of dissociation. Using solely the molecule peaks assumed that there was no molecular excitation arising from the discharge which might affect the chlorine molecule cracking pattern. At low levels of dissociation, such excitation could cause significant error in dissociations based on measurements as made here, but it is doubtful if the high levels of dissociation finally achieved contain much error from this source.

It is also unfortunate that the presence or absence of excited species in the chlorine atom beam could not be checked. That the molecular beam technique is eminently useful in such investigations has been demonstrated in

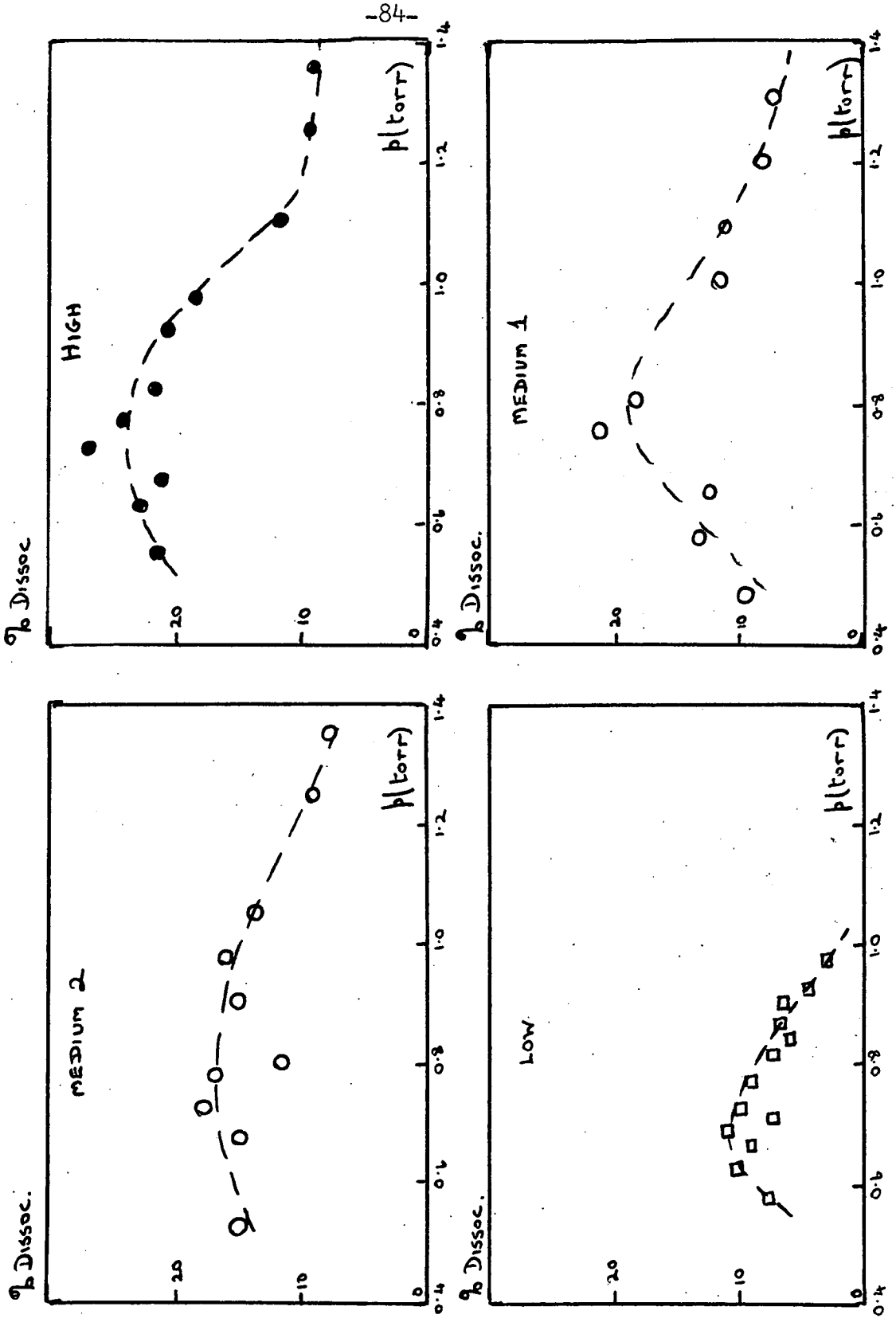

Fig.3.2. Chlorine Dissociation as a function of pressure/power level.

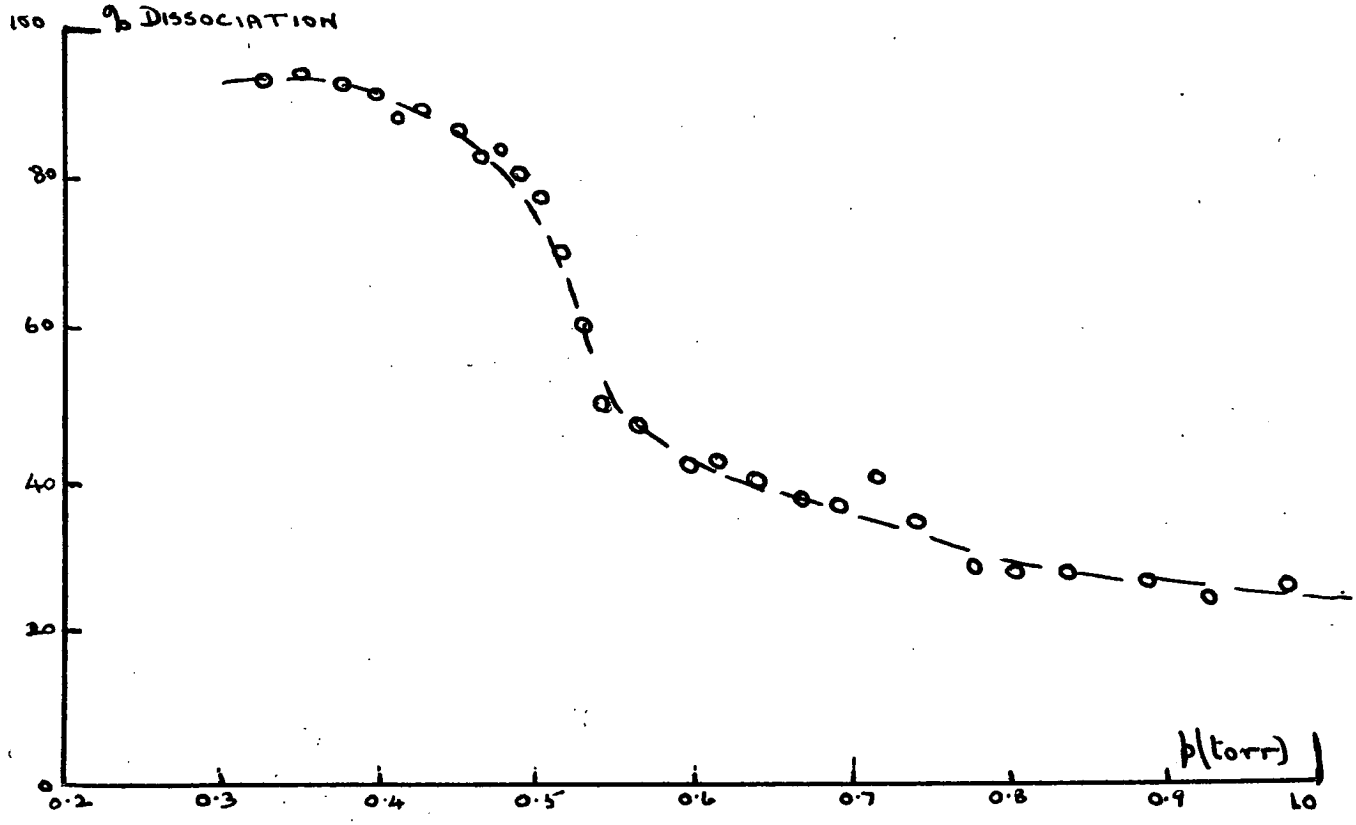

Fig. 3.3. Chlorine Dissociation (coated tube)

a review by Foner and Hudson (FON 66). By comparing appearance potential curves for, say, the Cl^{+}_{35} ion with the discharge on and off, the presence or absence of excited species should be readily detectable. Such measurements were impossible in the chamber used for testing the discharge source since the signal-to-noise ratio under optimum mass filter conditions was never greater than ten. However, by modifying the electron bombardment detector, building a separately pumped detector chamber and perhaps introducing a beam modulating system with lock-in amplification, the measurements required could be carried out. That they are essential is beyond question. Without adequate knowledge of the electronic states of the species, no meaningful interpretation can be made of any scattering data obtained using this chlorine atom source!

One further point, raised earlier, also casts doubts on the usefulness of the chlorine atom source. As noted, there is some controversy over the temperature of the neutral gas in a discharge. The molecular beam technique could resolve this simply by velocity selecting the beam using a selector, already calibrated with an alkali metal source, if necessary. The use of velocity selectors, however, cuts down the observed intensity by perhaps a factor of 100 at the distribution maximum, so that there is no possibility of using one in our measurements. Again such measurements would be possible if the modifications suggested were carried out. These measurements are also essential in view of the strong dependence of the scattering pattern on the relative velocity of the colliding partners.

Thus the r.f. discharge source produces chlorine atoms with high efficiency but the atoms are in some unknown electronic state and of unknown energy. It was therefore decided that work should cease on this source and that a thermal dissociation source should be built for the more

weakly bonded iodine molecule.

Thermal Iodine Source.

In any effusion source, the gas within the source is assumed to be in thermal equilibrium with its surroundings. The degree of dissociation of a diatomic gas, say I_2, in such a source is therefore governed, at constant pressure, by the temperature dependence of the equilibrium constant for the reaction

$$I_2 \rightleftharpoons 2I. \qquad (3)$$

since it can be shown that, if the degree of dissociation is given by α, the equilibrium constant can be written as

$$K_p = \frac{4\alpha^2}{1-\alpha^2} \cdot p_{total} \qquad (4)$$

In thermodynamic terms, this equilibrium constant is expressed by the equation

$$\Delta G_o = - RT \ln K_p . \qquad (5)$$

ΔG_o being the standard free energy of the reaction, referring to the standard state of one atmosphere and temperature T. (°K). By use of the Gibbs-Helmholtz equation the temperature dependence of K_p is given by the relation

$$\ln K_p (T) = \int_{T_o}^{T} \Delta H_o / RT^2 \, dT + \ln K_p (T_o). \qquad (6)$$

where ΔH_o is the heat of reaction.

To proceed further and integrate this equation we must either assume ΔH_o is independent of temperature or we must know its temperature dependence. An explicit expression for this, derived using Kirchhoff's equations, gives

$$\Delta H (T) = \Delta H(T_o) + \int_{T_o}^{T} \Delta C_p \, dT \qquad (7)$$

i.e. the difference between the heats of reaction at T and T is equal to the difference in the amounts of heat that must be added to reactants and

products to raise them from T_o to T.

The heat capacity of diatomic iodine at constant pressure can be expressed by the series $C_{p_{I_2}} = C^\circ + \beta T + \gamma T^2$ whilst that of monatomic iodine will be simply the translational specific heat contribution namely 3/2 R (+ R, since at constant pressure) = 5/2 R.

Thus, substituting and integrating, the temperature dependence of the equilibrium constant is given by

$$\ln(K_p(T)) = \ln K_{p_o}(T_o) - \frac{\Delta H_o}{RT} - \frac{C^\circ}{RT} - \frac{R}{\beta}\ln\frac{\beta T}{R} - \frac{\gamma}{R}T + \frac{5}{2T} \quad (8)$$

Using data from the N.B.S. Circular 500 Tables, the graphs of degree of dissociation versus temperature were drawn in Fig. 3.4. for the total pressures indicated. From these curves it can be seen that for source pressures in the range 0.5 - 2 torr, dissociation levels of greater than 90% are achieved at temperatures in excess of 800 °K, a value fairly readily realizable in our apparatus.

Experimental. The iodine atom source (Fig. 3.5.) was based on the wellknown double chamber design. The lower chamber, boiler or tail, was made by closing off a glass-to-metal seal. This chamber maintained between 25 and 40 °C controls the vapour pressure of the iodine in the source. The seal was brazed into a monel super-heater or upper chamber. At temperatures in the region of 500 °C, this controlled the degree of dissociation.

Tail heating was provided by a 24 watt soldering iron element in an aluminium sheathing block, powered from a Farnell 0 → 5 amp, 0 → 30 volt, stabilized power supply. A specially made nichrome-wound, asbestos-insulated heater surrounded the super-heater, the power here being, supplied by a 0 → 20A, 0 → 30 volts power unit. Temperatures were measured by Cr/Al thermocouples and a Comark 166c electronic thermometer.

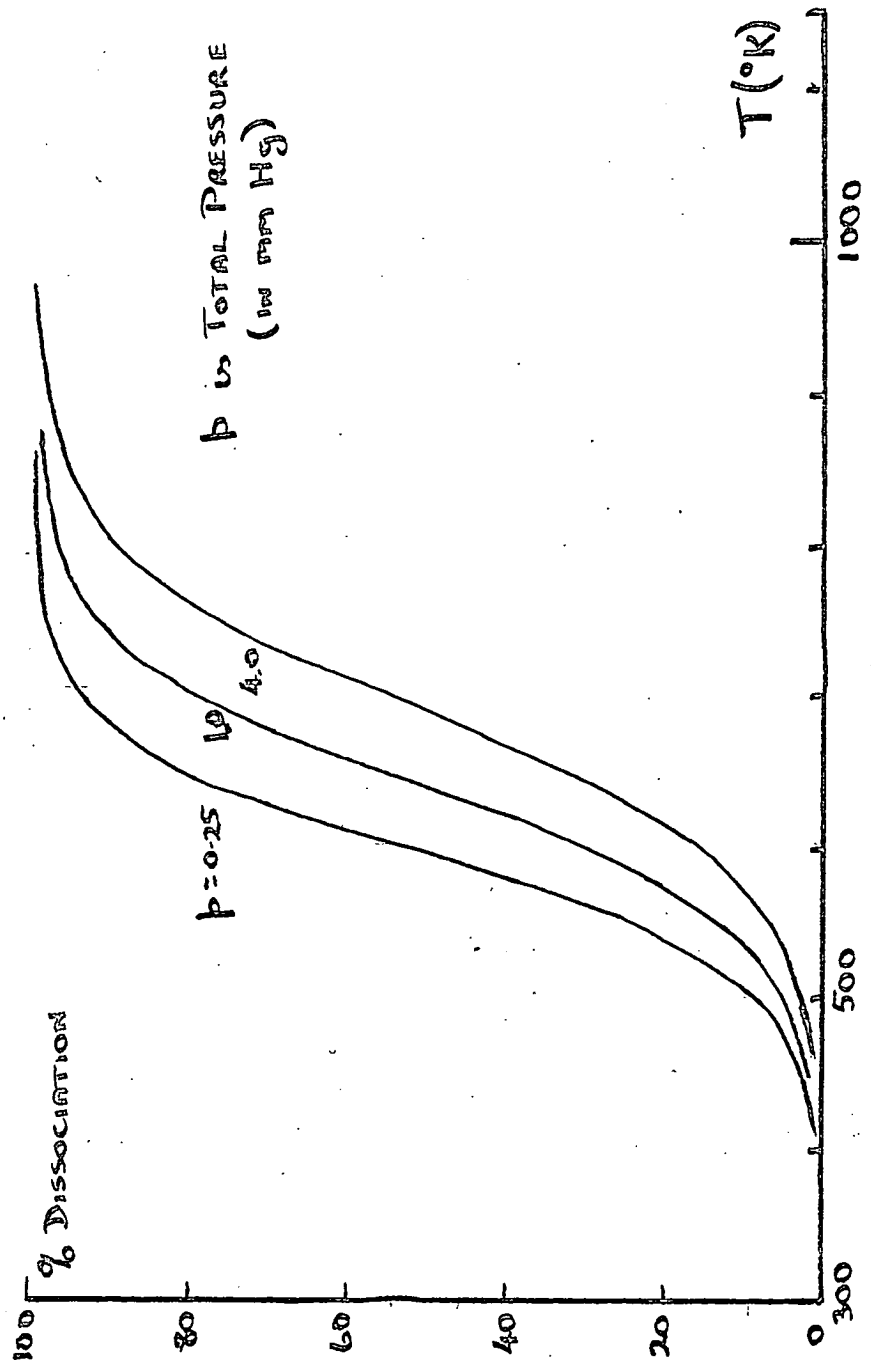

Fig. 3.4. Dissociation of I_2 as a function of Temperature.

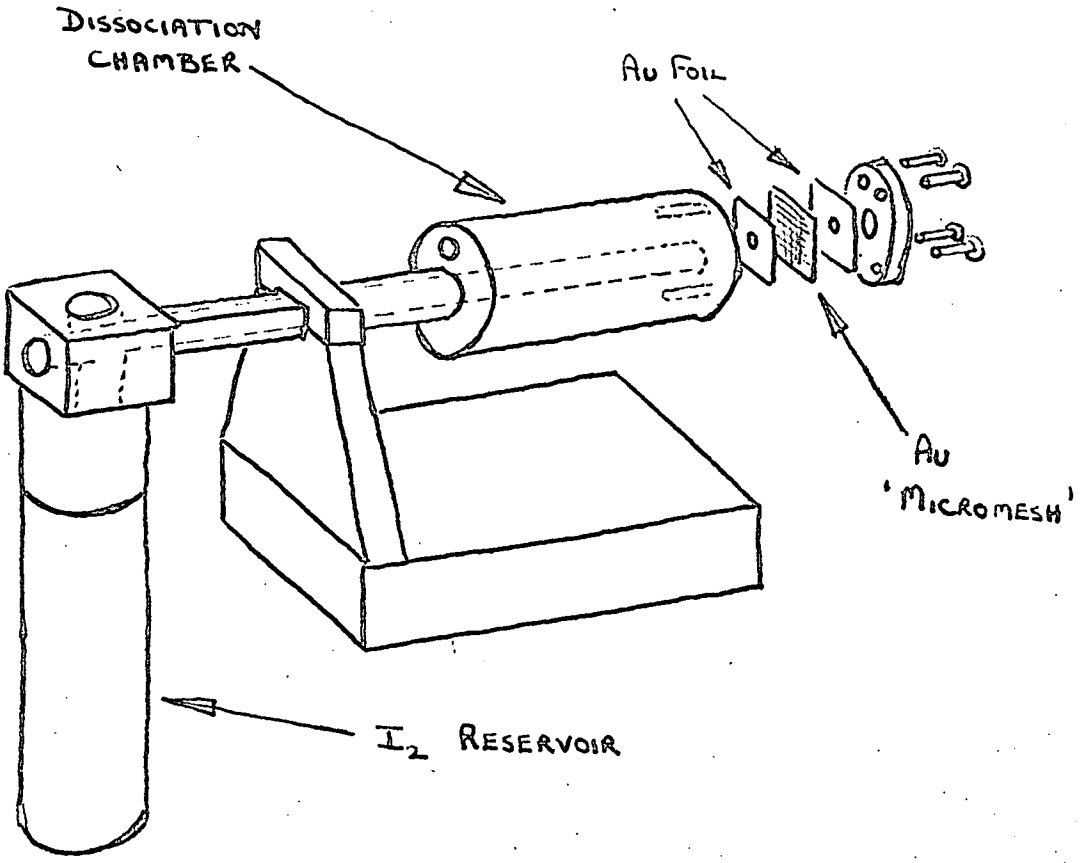

Fig. 3.5. Iodine atom Source (Thermal Dissociation)
Showing slit system.

Performance and Problems. A short series of runs in the test stand showed that the levels of dissociation predicted by calculation for any particular temperature and pressure were being achieved. This series also revealed several problems - overheating of the tail, corrosion and lack of intensity, the perennial problem in molecular beams.

Taking these in turn, the overheating was simply a conduction problem - the heat from the atomizer travelling down the 1/32 inch wall of the tube to the tail. This was overcome in the main apparatus simply by fastening braided copper straps between the central support block of the oven and a cooling-water pipe. Even with this, however, there was seldom any need to use the tail-heater.

Corrosion by the atomic iodine was a much more serious problem. Originally it was thought that stainless steel would be sufficiently resistant to attack by I so much so that the first atomizer and barrel were machined from a stainless steel bar. The first oven slits were also three channels (10 thou. by $\frac{3}{8}$") along one half of a split stainless steel cylinder ($\frac{1}{8}$" diameter). After the first high temperature run, the slits were showing marked signs of corrosion. They also showed that they alone did not give a high enough beam flux. The channels were therefore replaced by three layers of nickel Zacharias foil. These crumbled to powder when the slits were removed after the second run.

By this time, it had been decided to remake the atomizer in monel, a copper-nickel alloy which is highly resistant to attack by the halogens, a somewhat surprising fact since both copper and nickel on their own have been found to be readily corroded. This monel super-heater proved to be highly successful in overcoming the atomizer corrosion problem.

However, we were still faced with the problem of finding suitable slits

of suitable material. As expected the Zacharias slits provided higher intensities than three single channels but the nickel corroded rapidly. Moreover the corrugated foil had been begged in the States since the Department did not have a milling machine accurate enough to machine the roller. Thus even if we wanted to we could not make Zacharias type foil in any other material. But, even if we could have, the nickel foil which lasted fairly well in I_2 was only giving marginally good enough intensities at 5 → 10 torr and the higher the source pressure the higher the atomizer temperature needed to achieve the desired level of dissociation.

Both these problems - corrosion and intensity - were solved by one of those coincidences they would have us believe are so prevalent in scientific research. My coincidence was simply a re-reading of a review by Pauly and Toennies (PAU 65) at a time when another member of the group had procured a fine mesh for use as a grid in a field emission detector he was designing. In this review, it is noted that photoetched meshes with small rectangular holes, 7.5 microns on one side have been suggested for obtaining higher intensities (DAT 61). The copper 'micromesh' supplied by E.M.I. had holes of dimension1.7 thou.sq. , separated by 0.3 thou. web micromesh.

Assuming effusive flow, the intensity in the forward direction calculated for an ideal orifice of area A_o sq. cm. and source pressure P torr at a temperature of T degrees Kelvin for a gas of molecular weight M is

$$I(0) = 1.12 \times 10^{22} \left(\frac{PA_o}{\sqrt{MT}}\right) \text{ mols/str/sec.} \quad (9)$$

Assuming that the above equation holds for a single long channel as well, then at constant temperature and pressure the ratio of fluxes from the different systems is simply the ratio of their effective source areas, so that the micromesh has a factor of twelve advantage on the Zacharias foil since it

packs that many more holes to the same area.

Using an I_2 beam, the copper mesh was most effective but this too crumbled under the onslaught of atomic iodine. E.M.I. also supply the mesh in gold, however, and this was found to resist attack fairly well, thought it was replaced after every run. The slit system was particularly easy to make, simply sandwiching a piece of micromesh between two pieces of gold foil from which the exposed area had already been cut.

All measurements reported were made with this source and slit system, though some of the early I_2 runs were made with Zacharias foil.

CHAPTER IV

EXPERIMENTAL

INTRODUCTION

On the experimental front, the main effort has been directed into increasing the signal-to-noise ratio of a thermal energy molecular beam apparatus built between 1964-1968. to study alkali metal-alkali metal small angle scattering. A complete description of this machine is contained in the Ph. D. Thesis 'Theoretical and Experimental Studies of Molecular Scattering' by L. T. Cowley (Edinburgh, 1968). Inherent in the design of this machine was a high resolution capable of observing the oscillations expected in small angle scattering. However, this high resolution also made it impracticable to observe scattering at much greater than one degree from the main beam for by this angle the signal-to-noise ratio had dropped to 0.1 . Because the detector was at a fixed distance from an only slightly variable scattering centre, the only real means of extending the angular range of our observations were (i) to boost the intensities of our beams (ii) to reduce the background in both detector and scattering chamber (iii) to improve the detection efficiency of the surface ionization detector (iv) to improve the signal-to-noise ratio by any other means possible, e.g. modulation.

From the data of L. T. Cowley, typical values for the above quantities were:

Main beam intensity		1 →1.5 MHz.
Background (at $\theta = 0$)		10→ 12 Khz.
Overall detection efficiency	=	11%
Signal-to-noise Ratio at 1 degree	=	0.1

Following the modifications to be described, these quantities now have the values.

Main beam intensity 1 → 1.5 MHz.

Background (at $\theta = 0$) 1 → 3 kHz.

Overall detection efficiency - not measurable.

Signal-to-noise ratio at 1° degree = 5

The plan of the rest of this chapter is roughly as follows:- First of all a general description of the apparatus pointing out any minor modifications carried out, after which there is a full description of all major changes made.

Description of the Apparatus

The main features of the apparatus are shown in Fig. 4.1. Broadly, it consists of two vacuum chambers, the larger containing the sources and scattering region and the smaller a separately pumped detection chamber. For a full and complete description of the original thermal energy beam apparatus, the Ph. D. thesis of L. T. Cowley, (1968) should be consulted, only a cursory description being given of any part not altered or removed.

The sources, collimating slits, beam flags, velocity selector and chopper were all mounted on a turntable, rotatable about the "scattering centre" so that in-plane angular measurements over the complete "internal quadrant" could be made. The turntable could be rotated in accurately measurable increments of 0.05°. Because of the reduction in intensity incurred in mechanical velocity selection only the primary beam carried a selector.

An all stainless steel structure, the main chamber was built in two sections, the top part being a removable lid. The lower portion was a square skeletal frame approximately 50 cm. long. Sideplates were bolted onto the four sides of this frame and held the detector chamber, a perspex window and electrical and water lead-throughs. The fourth side was blank. Contained within the lid which had to be lifted clear by chain hoist, was a 20 litre copper cold trap. From this hung $\frac{1}{8}$" copper sheeting forming a liquid

Fig. 4.1. Cut-away view of thermal energy molecular beam apparatus.

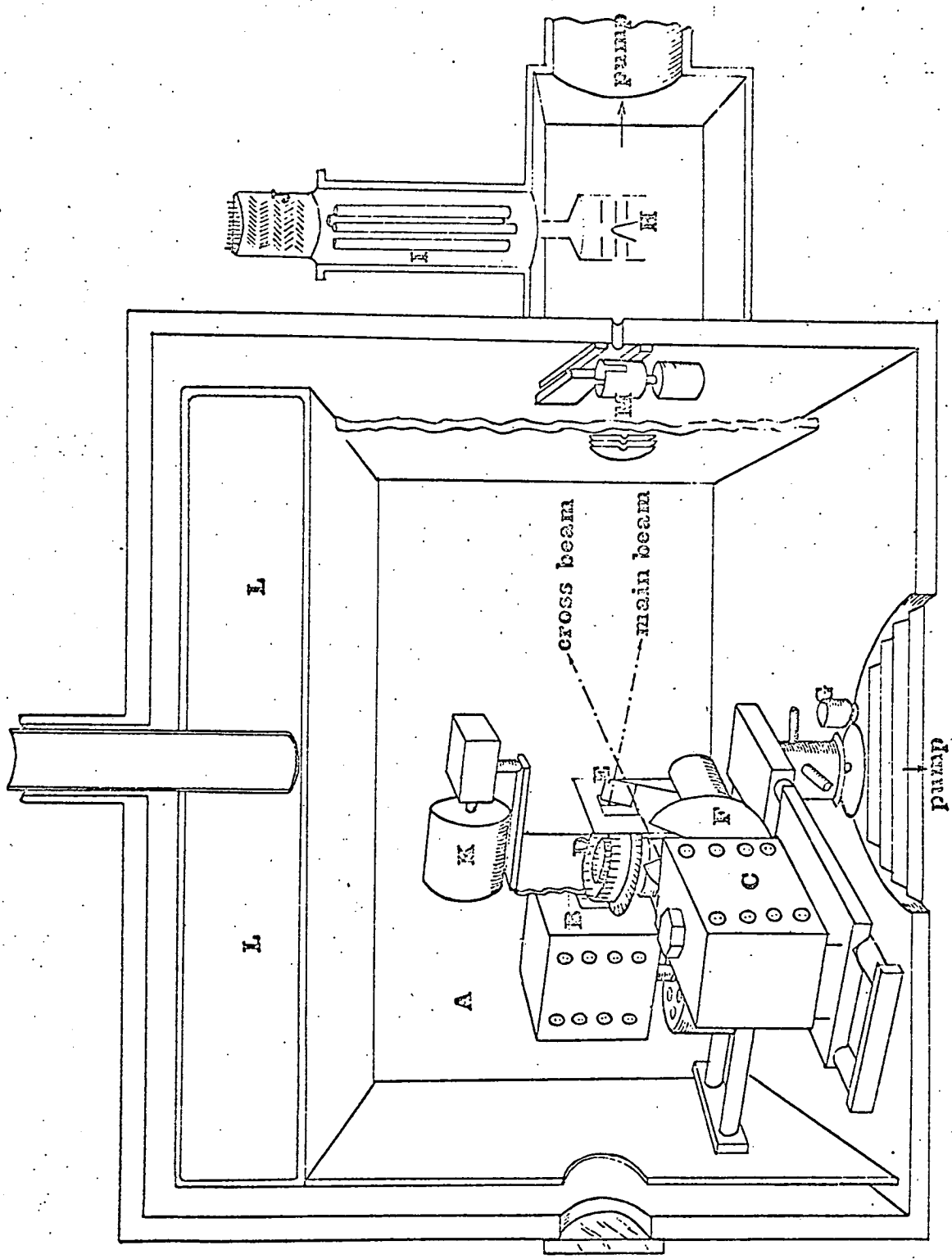

nitrogen cooled curtain wall on all four vertical sides of the main chamber. The trap was automatically filled by blowing LN_2 over from a 250 litre dewar, using an expansion operated device to switch on the filling mechanism for a specifiable period.

The main chamber was pumped by an Edwards 12" oil diffusion pump with a water cooled chevron baffle backed by a single stage Edwards IC450 rotary pump. On the backing line between diffusion pump and rotary pump a liquid nitrogen cold trap prevented corrosive condensibles from contaminating the rotary pump.

During a run a Pirani gauge indicated the backing line pressure while pressures in the scattering chamber were measured on an Edwards 1G2MA ionization gauge. A second Pirani gauge was used in a vacuum interlock system to protect the diffusion pump and oven windings from vacuum failure.

The sources together with the collimating slits and velocity selector were mounted on a rotatable platform which was in turn housed in an aluminium support carriage. Much of the roof of the original carriage was cut away in an effort to achieve greater pumping in the region of the sources. The carriage rested on two parallel bars which enabled it to be replaced in a reproducible position since it had to be removed for oven alignment, reloading or other maintenance.

The rotating platform consisted of two sets of parallel bars fixed at right angles into a central hub. The oven mounts rested on these bars, their distance from the scattering centre therefore being alterable without loss of alignment. The hub also contained a four-way rotating seal through which cooling water was piped in and out. The other two channels were intended for supplying gas ovens. The seal worked well providing the rubber 'O'-rings were kept well-greased.

Rotation of this turntable in increments of 0.05° was achieved using a 'Slosyn' stepping motor coupled to a 36 : 1 reduction gear-box. The relative position of the turntable was measured by an S. G. Brown 'Minitac' shaft rotation indicator coupled by a rubber tyred friction wheel to the hub. The output from the encoder displayed the turntable position on an electronic counter to an accuracy of 0.05°.

In the original set-up both beams could be interrupted by electromagnetically operated beam flags. Now the cross beam flag has been removed and replaced by a two bladed chopping disc. This was rotated at 1000 r.p.m. by a Smiths M.H.S. 111 three phase motor. The main beam flag was also moved from its position between oven and collimating slit to immediately in front of the final collimating slit after the velocity selector. There were two reasons for doing this. First of all it meant the overall length of the main beam oven mount could be contracted and the oven therefore brought slightly closer to scattering centre, increasing the beam by approximately $\frac{1}{3}$. The second reason was slightly more involved. Between the oven aperture and collimating slits a cloud of gas is generally trapped. A beam flag moving through this cloud cuts of the main beam but the cloud itself acts as a secondary source, leading to a spurious scattered signal when the main beam off background is measured. In the flag's new position this spurious signal was avoided since the beam flag cut cleanly across a beam well collimated by two sets of slits and a velocity selector.

The main beam oven was of the two-chamber type thus enabling beam energy to be varied independently of source pressure. Two layers of corrugated Zacharias nickel foil formed the beam orifice. Both upper and lower chambers were heated using nichrome wire threaded through fused alumina tubes. Typical running conditions for sodium were a boiler temperature of 400° C

and a superheater temperature of 450 - 500 °C. The temperatures required for Potassium were 100 °C below these values in both cases.

The velocity selector used was that designed by L. T. Cowley for his Na/K measurements (COW 69). This was of a rather unusual design in that the beam passes across a crenellated disc in a direction perpendicular to the rotation axis, instead of passing through rotating slits in a direction parallel to the shaft as in the conventional Bernstein type.

Detection and Modulation System.

Chamber and Pumps.

The separately pumped detector chamber could be isolated from the main chamber by a gate valve on the scattering chamber side. Made from a single piece of stainless steel, the flange surfaces of the original chamber were milled flat for gold O-ring seals, all, that is, except the ion pump flange which had a knife-edge and copper gasket seal.

Pumping, at this time, with an 80 l/s ion pump produced pressures in the detector chamber of the order of 5×10^{-8} torr. In order to reduce this pressure and it was hoped the alkali metal background in the detector chamber, a cross piece equipped with a 1000 l/s titanium sublimation pump and cold trap was fitted between detector chamber and ion pump. The cold trap was specially designed so that there was no optical path between detector and ion pump nor between detector and T.S.P. filaments. This system succeeded in reducing the detector chamber background pressure to $\sim < 10^{-9}$ torr as measured by the ion pump current. It did little, however, to reduce the count rate from background alkali metal which still remained of the order of 2 - 5 KHz at this stage. The reduction in pressure will certainly be much more useful should an electron bombardment detector ever be fitted to this machine.

Scattered particles entered through an $\frac{1}{8}$" diameter hole in the sideplate to which the detector chamber was bolted. This hole was further limited to 0.03" wide x 0.125" high by a pair of adjustable knife-edge slits. The gate valve, which was operated externally by a wormwheel drive arrangement, also carried a beam attenuator.

This was only used in the region of the main beam in an attempt to preserve a low detector chamber background. At wide angles, however, it was moved to one side, again using the gate valve drive mechanism. A cylinder, with four slots, the beam passed perpendicular to the axis of rotation. To prevent this acting as a velocity selector one of each pair of diametrically opposite slits was made twice as large as its partner. The attenuator motor was also a Smiths MHS 111 mark three , three phase motor and was run at its rated speed of 12,000 r.p.m. The attenuation factor, fixed by the ratio of slit width to cylinder circumference, was approximately 12. It was, however, calculated on every sweep since its value varied slightly, with attenuator position, this depending upon whether the beam passed diametrically across the cylinder or not.

An Atlas AMP3 quadrupole mass spectrometer formed the basis of the detector but the original electron bombardment detector had been replaced by a rhenium filament surface ionization detector. In this design particles entered through a hole in the outer cylindrical electrode and struck the hot ribbon where they were ionized. Those which missed the filament remained trapped in the lens system possibly undergoing ionization at some later time and contributing to the measured background. To improve the pumping in the neighbourhood of the filament and allow the unwanted material to escape after a first pass of the filament, the outer solid electrode was replaced by a stainless steel mesh cylinder. The extraction portion of this lens

was also modified in an attempt to increase the transmission of the lens assembly. Due to leakage currentsit proved impossible to measure this factor after modification.

Because it was feared that a cooler filament would greatly increase the transmission time from atom arrival to ion detection, the 30 x $1\frac{1}{2}$ thou. Rhenium filament had been run at 3.5 amps. The temperature this gave was not measured since the slits leading to the scattering chamber through which it could be observed defined an area too small for accurate pyrometer measurements to be made. It was observed, however, that lowering the current to the filament had little affect on the signal though it decreased the background observed by at least a factor of 20. But by lowering the current to 1.5A the detector could be made so slow that it took 10 - 15 seconds to recover from opening the beam flag.

Nothing longer than a millisecond could be tolerated. Where was the optimum level of filament current that gave the best S/N ratio with this reasonable time constant? The value was arrived at by observing the pulses of ions passing through the attenuator. This ran at 12,000 r.p.m. giving four pulses per revolution, i.e. with a time separation of 1.25 msecs. With a filament current of 1.5A all these pulses merged into one. By 1.7 Amps definitely separate pulses were observable while by 1.9A their tail was only 1 - 2 tenths of a msecs. longer than the sharp edge they possessed at currents greater than 2.5 Amps. The optimum current level arrived at in this manner was 2.1 Amps. This was used initially for potassium and subsequently checked to be suitable for sodium. This step alone probably gave the greatest reduction in alkali metal background. For running at the higher temperature heated up the lens elements surrounding the filament boiling off any beam material capable of condensing on them during a run.

The lower temperature did not perform this operation though the condensation was still taking place. Consequently before any run the filament was flashed at 4 amps overnight to clean both it and the lens elements.

One unfortunate result of lowering the filament current was that it now became more susceptible to 'burst' noise especially with sodium as the main beam, periodically giving bursts of up to 7 or 8 hundred counts over a period of milliseconds. Their randomness and infrequency enabled these to be fairly readily rejected in the initial stages of data analysis.

Following these slight changes in the apparatus and operating conditions the background in the detector chamber is now typically of the order 100 - 150 Hz. Of this value an obstinate 10 - 15 Hz is contributed by the ion pump discharge in spite of this now being separated by 18" of optically blind path. Some of this also arises from the multiplier dark current and efforts are now going ahead to reduce this contribution by cooling the multiplier.

The rest of this chapter is concerned with the introduction and use of modulation of the cross beam.

Why modulate?

The combination of modulation techniques with atomic and molecular beam techniques seems to have been recognized independently by a number of workers as a means to improve signal-to-noise ratio in a variety of experiments. The earliest use of the combination seems to be in the work of Foner and Hudson (FON 53) who studied the constituents of flames by forming a beam and detecting the particles by electron impact ionization and mass analysis. With the neutral beam chopped the ions produced by neutrals from the flame gave an AC signal while those from ionization of background gas gave DC signals, thus the ion signals could be separated. Further early examples are provided by Wessel and Lew (WES 53) who modulated the beam of an

otherwise conventional r.f. spectroscopy experiment and by Fricke (FRI 55) in his development of a universal detector for neutral beams.

In the introductory chapter to this thesis, the scattered intensity observed at an angle θ was written as

$$I(\theta) = n_a n_b Q V d\Omega \qquad (1)$$

where n_a, n_b, are the intensities of the beams, Q is the differential cross-section and $d\Omega$ is the solid angle subtended by the detector.

This ideal state of affairs of the signal at the detector corresponding to the scattered flux alone is never realized. At any given angle the signal can be made up of a number of contributions from the following.

(A) Ions formed from background atoms in the two chambers and filament impurities.

(B) At small angles, the primary beam.

(C) Primary beam material scattered by background gas in the chamber.

(D) Electronic noise from multiplier and ion pump.

(E) Main beam atoms scattered from the cross beam.

If one could assume that everything remained constant with time to within a percent or so, there would be no difficulty; switching the cross beam on and off in a DC fashion would eliminate only E, the desired measurement, which could then be obtained by subtraction.

Unfortunately not one of the above quantities is constant with time. Each of them varies, some rapidly, some slowly, some regularly, some randomly.

Consider first the electronic noise from multiplier and ion pump and include with it the burst noise from the filament; the effects of these, being random are averaged out over a large number of measurement cycles so

that, though a large proportion of the remaining background, their presence is less troublesome than some.

The scattered signal, E, is directly proportional to the intensities of both main and cross beams. Though the ovens were left to stabilize at the operating temperatures for several hours after being brought to them, drifts in power and hence in signal are bound to have occurred during the 20 to 30 hours each run occupied. These drifts were, however, slow as attenuations in successive sweeps at the same velocity showed. The failure to introduce a time normalization process is, therefore, probably unimportant.

This leaves the effect of the background gas on the scattered signal, arising not only from beam material scattered by the background molecules but also from the attenuation of the beams by the background gas present in both chambers. Fluctuations, sometimes large, in background and hence in noise level occur because diffusion pumps do not pump steadily. Fortunately every vacuum system has a pressure time constant, τ, given by V/S where V is the volume of the chamber being pumped and S is the pumping speed. In a system employing modulation, the pressure fluctuations are handled by the vacuum system similarly to an RC electrical filter's handling of voltage fluctuations i.e. for a uniform pressure fluctuation input spectrum, the amplitude of the actual fluctuations is proportional to $1/\sqrt{1+\omega^2\tau^2}$ where ω is 2π times the moduation frequency. Thus while there can be large DC drifts, higher frequency fluctuations are attenuated and noise problems are reduced.

The experimental solution is thus clear. Rather than turning the cross beam on and off every few seconds or minutes as in a DC experiment, it should be turned tens or perhaps hundreds of times a second.

The scattering chamber of our apparatus has a volume of 125×10^3 C.C's. while the diffusion pump has a pumping speed of 1500×10^3 C.C's

per sec. giving a time constant of V/S = 0.08 sec. Fluctuations in the detector chamber background are equally important. Here the time constant is about 0.1 sec, so that one has only to sample faster than 10 or 12 times a second to begin to smear out the effects of pressure fluctuations. Our chopping speed of 66⅔ cycles per sec. should therefore be ample.

Experimental Set Up.

The signals associated with the scattering of the main beam from the chopped cross beam are AC at the modulation frequency and in specified phase while those arising from the interaction of the main beam with the background gas are DC. Thus one is presented with a modulated signal intensity profile as shown in Fig. 4. 2. Since digital information is more convenient and the signal level is very low, counting rather than current measurements are made. Two separate counters are employed (ideally they should be identical), one of them counting signal + noise during the cross beam open period, the other counting noise only when the cross-beam is closed.

The two bladed chopping disc is rotated in front of the cross-beam at a speed of 1000 r.p.m. by a Smiths 113 MHS/3 hysteresis motor. The blade also chops between a lamp/photocell arrangement providing a reference signal for the gating system. The geometry of the existing cross-beam oven and mounting prevented the photocell being placed diametrically opposite the oven collimating slit. Hence the pulse from the photocell has a geometrically calculable advance of 2-3 milliseconds on the end of the open period of the cycle. After amplification by a Schmidt trigger, the pulse is then fed into two chains controlling the gating of the counters. Each chain consists of a pair of pulse width delay units (AIM PWD 103) and a pulse amplifier (AIM PPA 104). The first of the delays controls the start of a counting period while the second controls its length. The amplifier merely makes

Fig. 4.2. Block diagram of detector electronics.

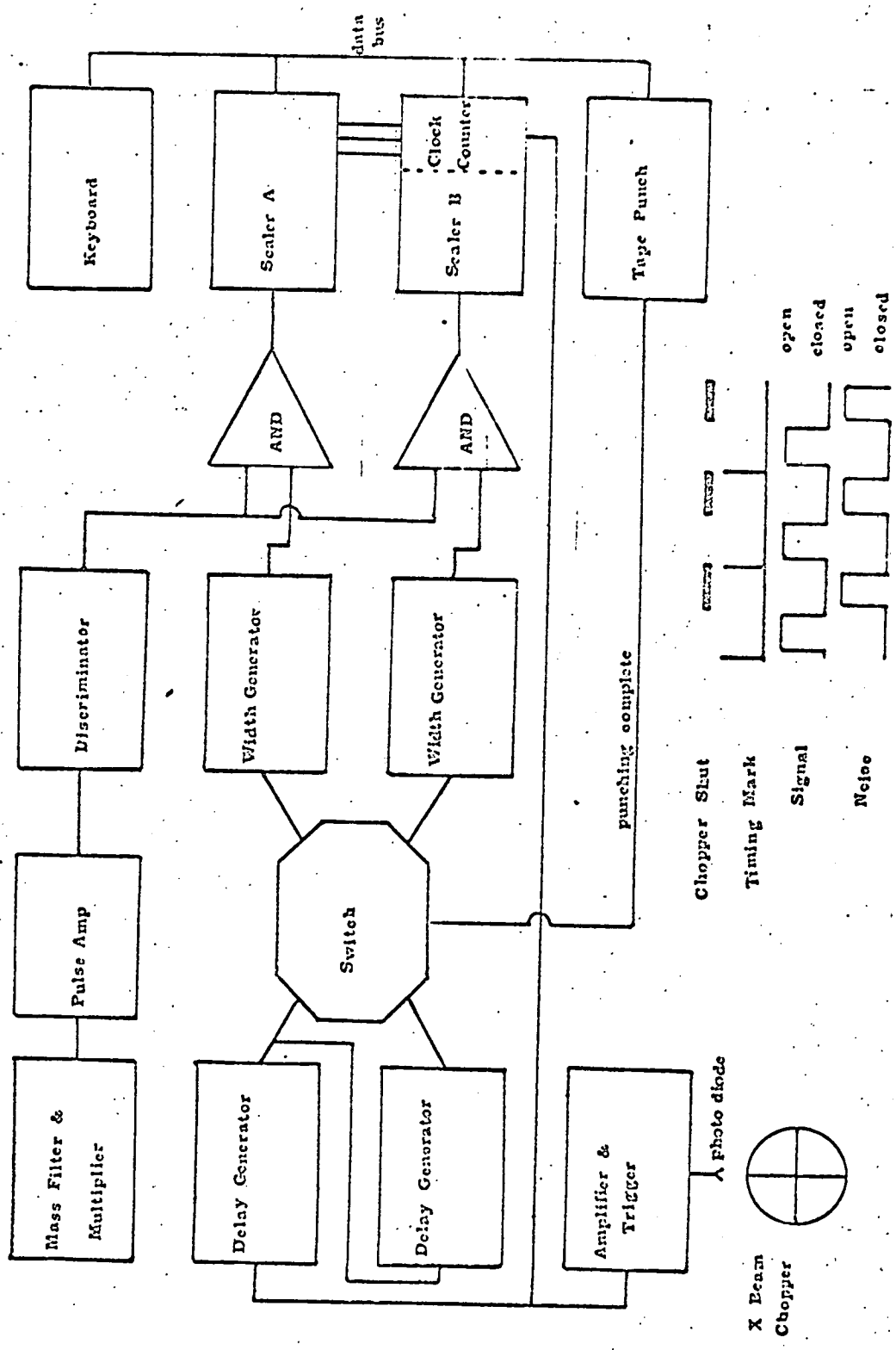

sure that the voltage is of the correct size and sign to operate the 'and' gate. The gating periods are purposely made somewhat shorter than the half-period of the modulation cycle to eliminate any jitter in the modulation. Also to compensate for the transit time of the molecules into the detector, an appropriate phase shift is introduced into the gating circuits. Thus starting from the photocell pulse, chain one which counts noise only has an aggregate delay of 5 milliseconds and a counter open time of approximately 12 milliseconds. Chain two which counts S + N has an aggregate delay of ~19 milliseconds and the same open time. The respective delays are adjusted using a Solartron double beam oscilloscope. The lengths of the two open times are approximately set up using the same instrument and then equated by obtaining, to within 0.1%, the same count rate on both counters using pulses from a Solartron pulse generator. After 100 such measurement cycles (the clock is also fed from the photocell output), the aggregate counts are displayed and simultaneously punched on paper tape.

Ideally in such a system both chains of electronics and both counters should be identical. In our case the counters are not. We have two Hewlett Packard counters, one, an HP 5245L is a very powerful and versatile unit with a pulse-pair resolution of ~20 nSecs. The other, an HP 3734A is a cheaper model with a dead time in the region of 280 nSecs. The dead times are emphasized because although the pulses emerging from the home-made pulse height discriminator are stretched to 200 nSecs, the integrated circuit 'and' gates cause some ringing in the cables. The slower 3734A does not see these pulses whereas the 5245L with its shorter recovery time does, although many of them are filtered out by adjusting the level of the 5245L's own discriminator. In view of the possible errors arising from this

source and to compensate for any drifts in the widths of the counter open periods, the roles of the counters was automatically switched after every 100 modulation periods. Thus on one 3-sec. (100 cycle) period the 3734A, say, would count S + N whereas on the next it would count N only, the 5245L complementing it on both occasions. Along with the counts a special code is also punched on tape indicating the mode of operation of each counter for any given pair of numbers. After this switch, the counters and clock are reset to zero and the process begins again.

A block diagram of the complete detector/counting system electronics is shown in Fig. 4.2.

Preliminaries and Data Acquisition Procedure.

After checking out and oiling the velocity selector bearings and greasing the O-rings in the turntable rotating seal, the ovens were loaded, the main beam with either sodium or potassium, the cross beam with iodine. The wiring up completed and all systems checked and rechecked, the carriage was lowered into the scattering chamber, the lid put on and the system pumped down. After the diffusion pump had been on for 1 - 2 hours, the pressure was checked to be around 5×10^{-5} torr. and the cooling water to the turntable turned on. The backing line cold trap was filled with liquid nitrogen and the ovens left on overnight to slowly warm up to within 100 - 150 degrees of their operating temperatures. Overnight also the detector filament was raised to 3.5 amps to drive off surface impurities from it and the surrounding lens elements.

The following morning the liquid nitrogen cold trap in the lid of the scattering chamber was filled and set to automatic filling. This lowered the scattering chamber pressure to approx. 1×10^{-6} torr. The detector chamber cold trap was also filled and two to three blasts of the T.S.P. given

at half hourly intervals while the ovens were raised to temperature and left to stabilize. The detector filament current was lowered to 2 Amps, its normal running value. Next the counter gating system was set up as outlined earlier.

The alignment of the velocity selector was checked by observing that the transmitted intensity was the same for both directions of rotation. This was done for several speeds. The machine was now ready to produce results with the detector lens system tuned up and the mass filter set at low resolution to either sodium or potassium. The time is now early afternoon of the second day.

Because of its high angular resolution this beam machine can also be used to measure relative total cross-sections by looking at the energy dependence of the attenuation of the cross-beam as well as measuring differential cross-sections. The procedures for acquiring and analysing the data are somewhat different in both cases and will therefore be treated separately.

Total Cross-Sections.

The method of measuring total cross-sections consisted of measuring the attenuated intensity over a range of main beam velocities, with many measurements interspersed at one particular velocity for normalization purposes. The measurements were taken in the same manner as for a single angular position in the differential cross-section case. In this instance the angle corresponded to the main beam peak. No attempt could be made to monitor the cross-beam or map its profile, so that all measurements are relative.

Differential Cross-Sections.

Angular sweeps commenced by rotating the turntable to about 0.5°

beyond the main beam peak(i.e. so that after crossing the beam, scattering measurements were made in the internal quadrant.) The turntable position was zeroed at this angle. With the selector run up to the speed required for the desired transmitted velocity, the attenuator was moved into position until passage across the main beam was completed. Also because the 3734A counter was overloaded by count rates greater than 100kHz, the count rate was further decreased by increasing the resolution of the quadrupole.

With the punch interface unit set on 'manual', the angle count was punched onto tape - in the 'auto' mode these digits receive the output from the 3734A counter. After several such counts, the unit was switched to auto and eight to ten counts were taken with the primary beam flag open after which three to four counts were taken with it closed. These numbers varied depending on the size of the scattered signal. At wider angles, for example, the numbers would be as large as 20 to 30. Each such count was composed of the output from both counters after a three second period (each consisting of 100 modulation cycles.) During this time the next angle had been dialled up on the interface unit, and after enough counts had been thought to have been obtained, the unit was switched to manual, to record this angle, the turntable being rotated 0.05 by the stepping motor. After waiting till the signal stabilized, the unit was switched to auto and data counts recorded for this angle.

This process was repeated at each angle out to about 0.5° past the primary beam peak into the internal quadrant. To proceed to larger angles, the higher count rate obtainable with the attenuator removed and the mass filter resolution lowered was desirable. With special codes to warn the computer the following procedure was carried out. First of all the attenuated/detuned main beam and background were recorded. Following

the entry of a second code the main beam intensity and background with the attenuator removed was punched. It proved necessary to note both beam and background since although the attenuator reduced the main beam intensity by a factor of twelve, the background was only halved. A third code was then used to indicate that the numbers following were obtained after the mass filter resolution had been lowered to the normal running value of 400. By taking the ratio counts recorded at stages two and one, the attenuation factor could be calculated while the ratio of three and two gave the mass filter detuning factor; During the first state of data analysis these factors were used to multiply up all averaged counts taken during passage across the main beam. The turntable remained stationary during all of the above process.

Taking measurements at each angle as before, the sweep was then continued out as far as scattered counts could be observed or be thought to be observed above noise fulctuations. The length of sweep depended, however, on the intensities of both beams. On good days, measurements could be extended out to three or four degrees. These were seldon, however, and most sweeps did not go out much further than two degrees. A single sweep carried out in the above manner took between 1 and 2 hours; at the end a separating code was punched on tape and a new sweep was started. The punch was left running throughout an experiment to act as a clock for subsequent time normalization of the intensities.

CHAPTER V.

RESULTS AND DISCUSSION.

Treatment of Results.

In these experiments data analysis was carried out in two stages, the intermediate results being stored on magnetic tape. Such an arrangement allows the bulk of the data to be boiled down prior to the more elaborate stages which may require to be run several times with different filtering processes.

Fig. 5.1a shows a flow diagram for this first program. An elaboration of this chart follows.

After each detector period of 100 modulation cycles the punch produced on paper tape a sentence of the format

nABCDnEFGHIJKnLM

The characters ABCD corresponded to the angular position of the turntable when the unit was in the manual mode. For certain codes, recognisable to the program, they also indicated the beginning/end of a sweep as well as the use of the attenuator, quadrupole detuning etc. In the 'auto' mode, ABCD and E were the five digit output from the HP3734A counter. The characters GHIJK were the five least significant figures of the HP 5245L counter, so that our count rate was never allowed to exceed 99999. L was used as a main beam flag indicator (zero for closed, one for open); M indicated the mode of the switching unit i.e. which counter was giving signal + noise and which noise, this only whilst counts were being recorded. M also indicated the mode of the interface unit.

Because of the possibilities of punch malfunction and operator error, each character was read in as a binary number. Having read in 16 characters without error, the program checks to see if these form a sentence of the correct format. If they do then the counts (ABCDE and GHIJK) are recorded in the proper arrays indicated by the character M. If they do not, then the

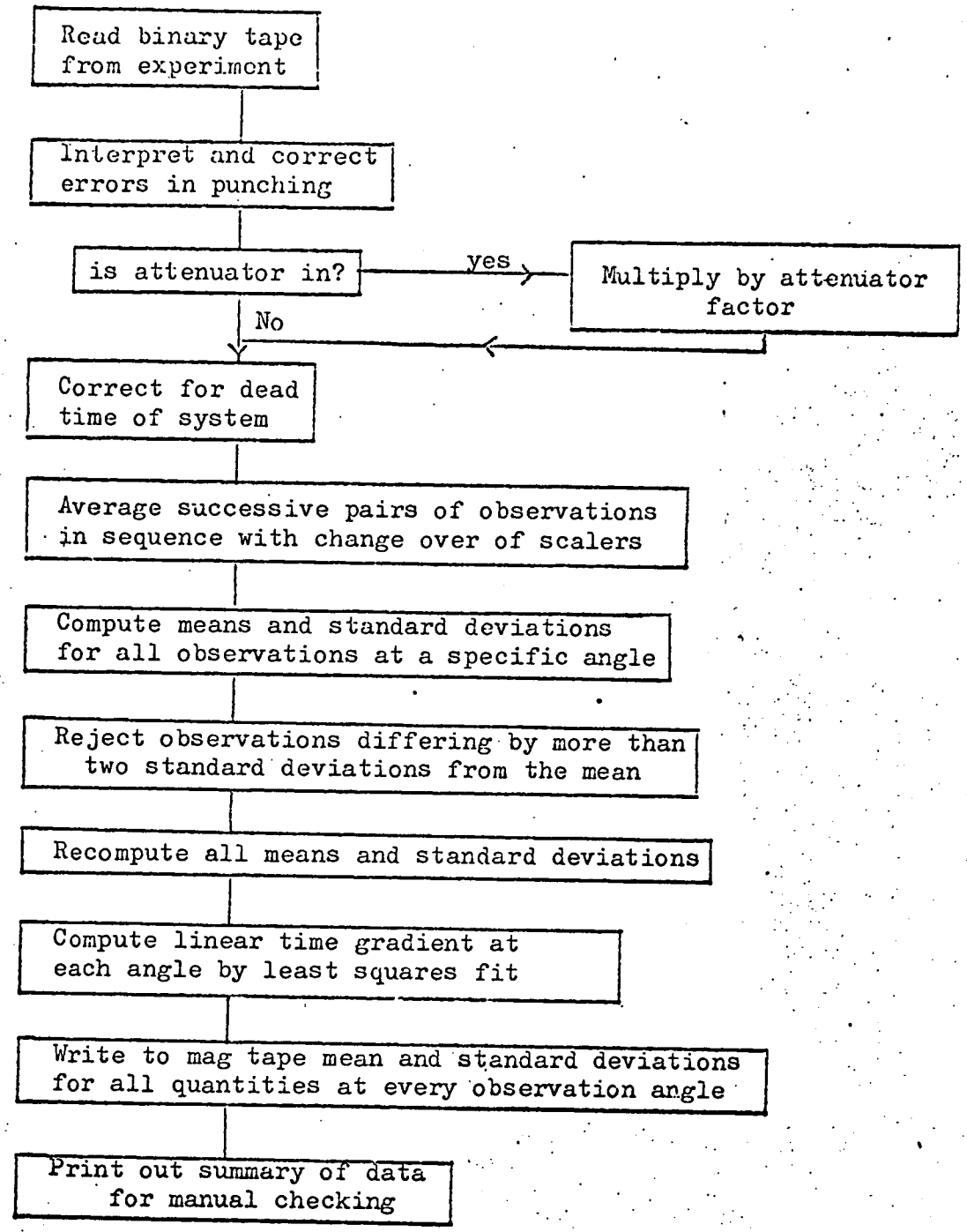

Fig. 5.1a. Flow diagram for first stage of data analysis.

reading continues until 16 characters have the correct format to form a sentence. If an 'illegal' character is encountered, the whole process begins again with the succeeding character.

This data collection is continued until a 'manual' coding indicates that the turntable has been moved to the next angle.

Before the tape is read further all the data accumulated for this angle is analysed. If the beam attenuator has been used for this part of the sweep, each count is multiplied up by the approximate attenuation factor. If the attenuator has not been employed, then the computer jumps to box 5 of the flow chart. Here each intensity count (multiplied up if necessary) is corrected for the finite pulse pair resolution time of the counting electronics using the relationship.

$$N' = N/(1 - \tau N) \qquad (1)$$

where N was the original count, τ the 'dead-time' of the system, and N' the corrected count. The attenuation has to be taken into account since the attenuator is a mechanical stop, the actual count rate being unaltered by its use. After correction, those counts which had been multiplied up by k are divided by this factor.

Each count was then sorted into a particular pair of arrays depending on whether the main beam flag was open or closed. Each successive pair of observations was then averaged in sequence with the changeover of scalers, to remove any possible bias in the counting chains. Means and standard deviations of noise, signal + noise and signal were then computed from these averages for both positions of the main beam flag. This computation was repeated rejecting observations differing by more than two standard deviations from the first guess at the mean. In this way filament burst noise affecting only one or two counts was removed. Following this the

linear time gradient for the angle was computed by least squares.

At some stage during the sweep, the manual coding indicates removal of the attenuator and tuning up of the quadrupole. By comparing successive averages from these channels the true attenuation factor and mass filter detuning factors are calculated, as are their standard deviations. After this the sweep continues as before.

At the end of an angular sweep, the summarizing array is read to magnetic tape. This contains the means and standard deviations for all quantities at each observation angle, the attenuated and detuned values being corrected for these points where applicable.

Following this summary, with line-printer graphs, is printed out for manual checking.

Though this system is time saving and allows vast amounts of data to be handled, its main disadvantage is lack of immediate feed-back to the operator enabling experimental conditions to be optimised. In fact, if on-line facilities had been available, angular sweeps which appeared during the experiment to have run out of steam, would have been continued since subsequent analysis showed plenty of signal-to-noise ratio still on hand.

The flow diagram for the second analysis program is shown in Fig. 5.2a. This program initially was planned to carry out a time normalization procedure for all observations greater than 1 . At smaller angles the signal changes so rapidly with angle that small changes in turntable position make the process unstable. In general this correction for time drifts in main and cross-beam intensities is only necessary for very wide angle scans taking more than an hour to complete. When required both the time gradients and the repeated observations at normalizing angles were to be used. The gradients are first smoothed and then integrated stepwise, the resultant

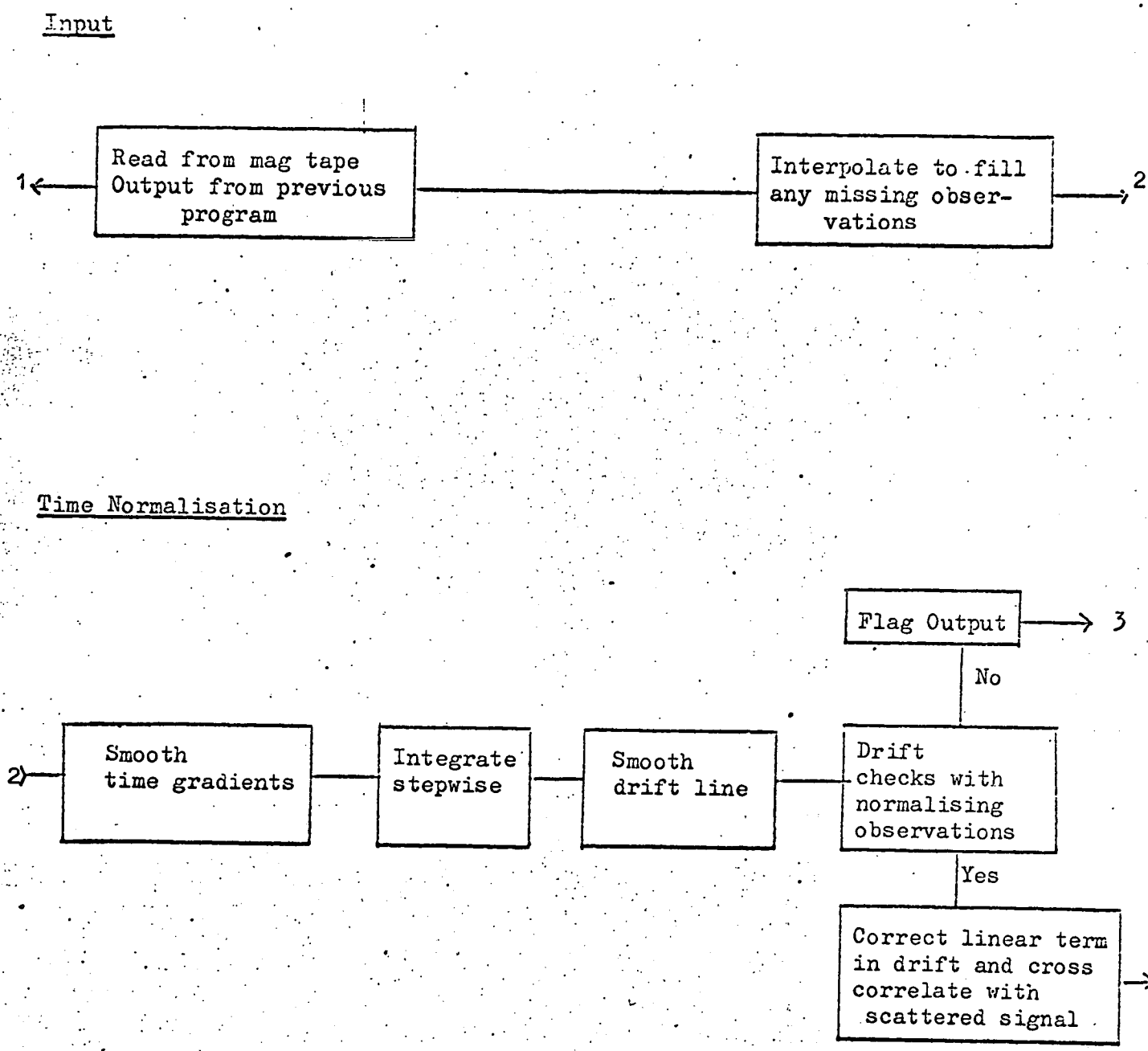

Fig. 5. 2a. Flow chart for second data analysis stage
(See also next page)

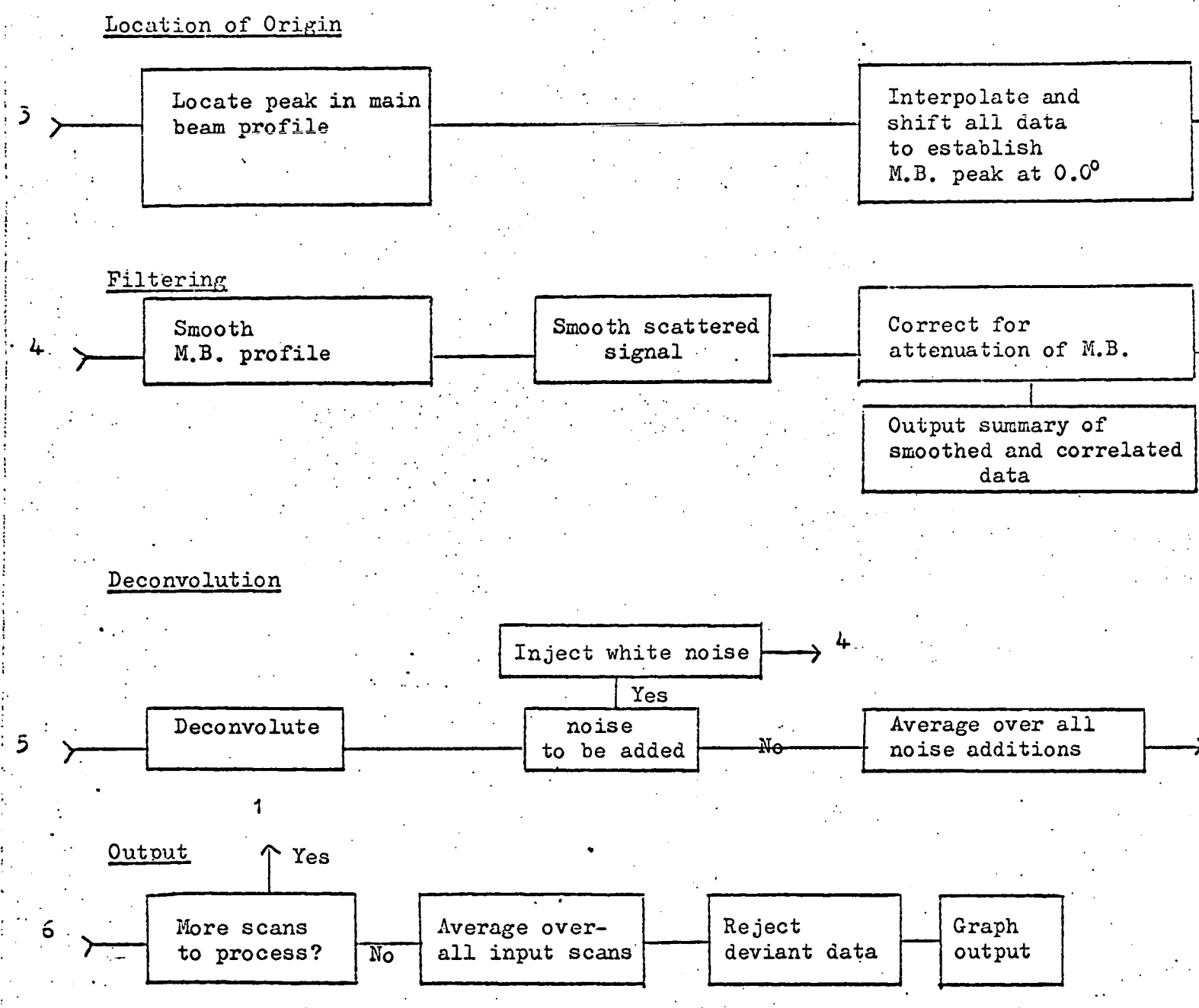

Fig. 5. 2a. Flow chart for second data analysis stage (continued).

drift line being then further smoothed by fitting to a cubic polynomial. The predicted drift is compared with the observed change between repeated angles and the linear term in the drift expression corrected to obtain concordance. If the required adjustment is too large, the output is flagged for manual investigation.

It proved rather difficult to bring this planned normalization into operation. Moreover attenuation measurements for repeated sweeps at the same energy showed only slight drifts. The time normalization procedure was therefore never used. The rest of this program is concerned with smoothing and deconvoluting the crude scattered signals.

The convolution equation

$$h(x) = \int_{-\infty}^{\infty} f(y) \cdot g(x-y)\, dy \equiv f * g \qquad (2)$$

can often be used to describe experimental broadening or loss of resolution. Here h (x) is the measured spectrum, f (y) is the corresponding ideal spectrum and g (z) is the apparatus or resolution function. The observed spectrum would be identical to the ideal if g (z) were a delta function i.e. if the experiment had no broadening effects. In a beam experiment, g (z) may be taken to be the observed distribution of the primary beam and h (x) the observed scattered signal. Solving eq. (2) for f (y) will then give a distribution corrected for the spreading due to the finite extent of the primary beam (in angle and in energy, if necessary).

The most potent manifestation of the main beam angular spread is seen in the values of the scattered signal in the neighbourhood of its maximum. Here the scattered signal is negative because the attenuation of the edges of the main beam profile is also being detected. At larger angles the scattered signal passes through a positive maximum before rapidly falling

with increasing angle.

The second half of the second stage of data analysis consists of solving equation (2). The method of solution has been described by Morrison (MOR 63) and subsequently employed in a similar problem by Ioup and Thomas (IOU 67).

These authors make it clear that in general, smoothing, or the removal of incompatible noise, is necessary before unfolding. In this case the program has been written to employ Morrison's iterative method of smoothing,

$$I_1(\theta) = I(\theta)_{obs} * f$$
$$I_i(\theta) = I_{i-1}(\theta) + [I(\theta)_{obs} - I_{i-1}(\theta) * f] \quad (3)$$

This technique is first applied to the main beam profile using a fixed trapezoidal filter function 0.4° full width. The iterated values are constrained to be within four standard deviations of the observed intensity. The resulting smoothed profile is then used as the convolution function to filter or smooth the scattered signal. At this stage the cross beam attenuation of the main beam is removed; the scattering in and out of the detector cone at each angle being computed iteratively until convergence is obtained. The corrected and smoothed scattered signal is finally deconvoluted using the main beam profile and Van Cittert's iterative method of unfolding (CIT 31).

$$I_1(\theta) = I(\theta)_{SMOOTHED} + [I(\theta)_{SMOOTHED} - I(\theta)_{SMOOTHED} * f]$$
$$I_i(\theta) = I_{i-1}(\theta) + [I(\theta)_{SMOOTHED} - I_{i-1}(\theta) * f] \quad (4)$$

For most of this work the number of smoothing iterations varied from 60 to 100. The necessary number of applications of the unfolding equations

also varied, usually 20 to 30 being required. Only a small amount of computer time was required to process each set of data in this way. In Fig. 5.1. the results of applying this procedure to data from a typical angular scan are shown.

The program then averages several such scans and graphically outputs the results.

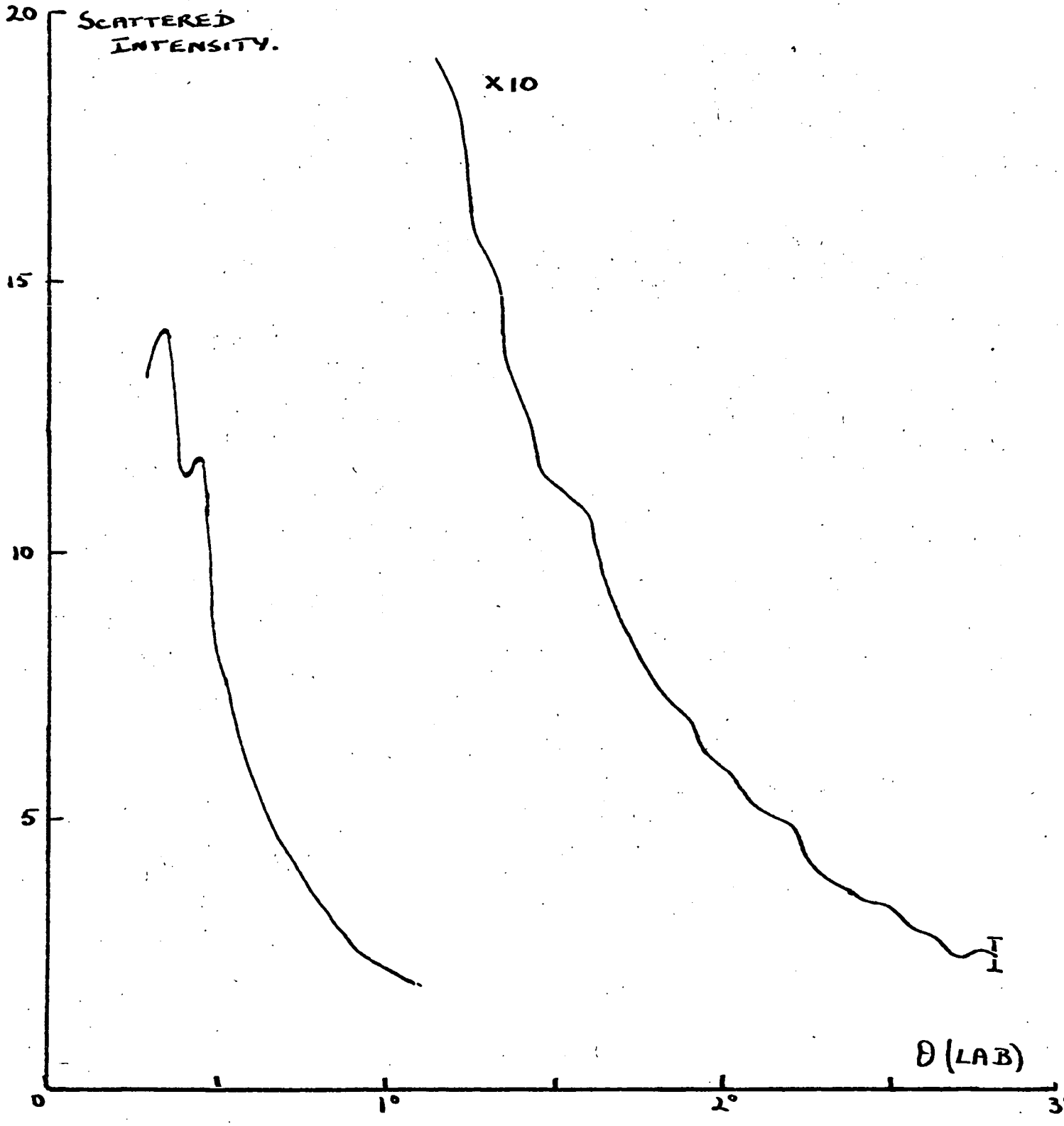

Fig. 5.1. Crude Scattering Results before deconvolution.

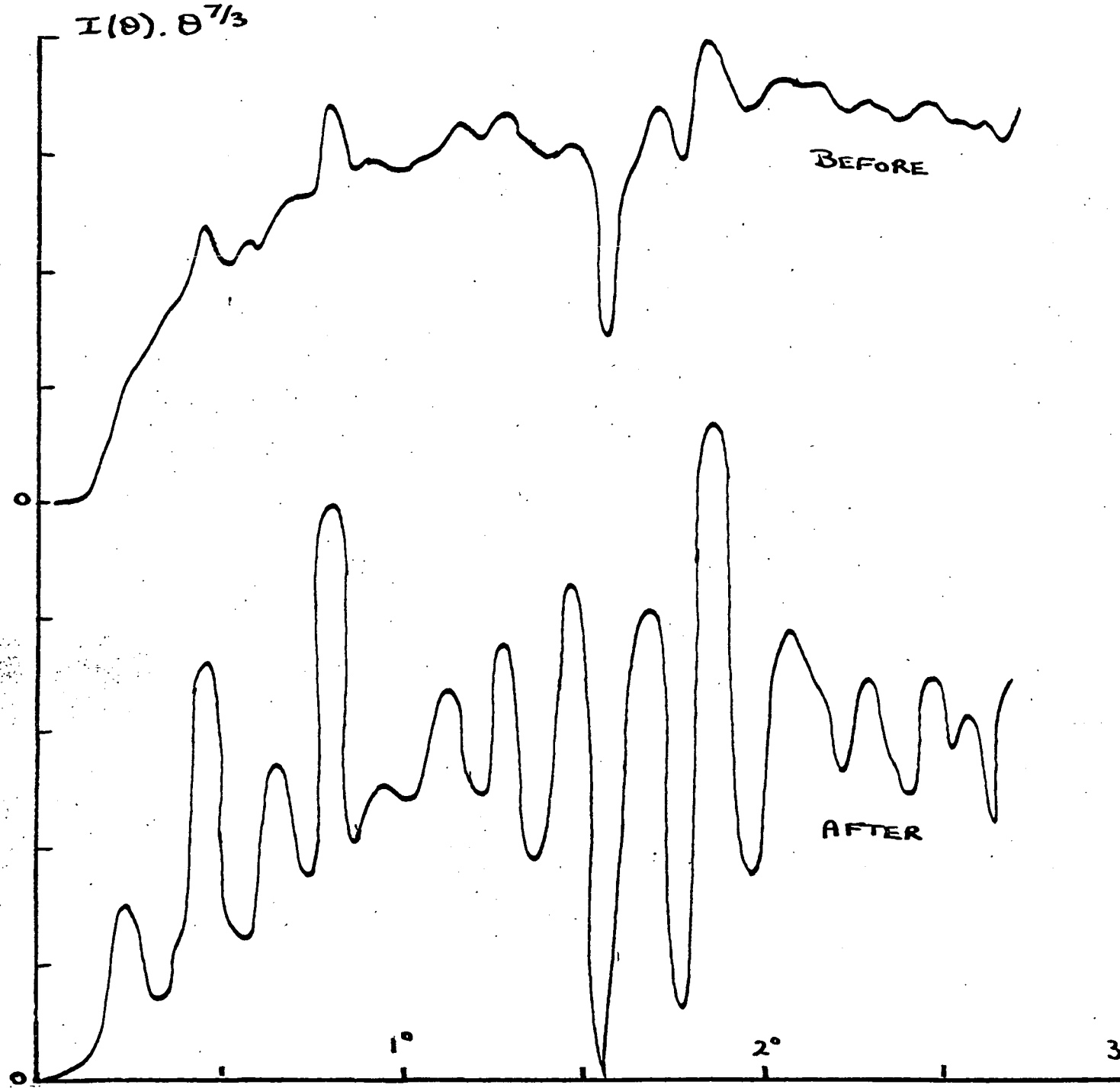

Fig. 5.1. Sample Sweep before and After Deconvolution.

Results.

Scattered intensity measurements as a function of angle were obtained as described in the previous chapter at three different potassium velocities for each of the systems K/I_2 and K/I. Attempts were also made to take measurements at these same velocities for the Na/I system. The main beam velocities were $5.41\alpha 4$, $8.07\alpha 4$ and $10.77\alpha 4$ cm/sec. Taking the most probable velocity of an iodine atom beam at 800 °K, these gave mean relative energies of 0.098, 0.188 and 0.315 $\mu\mu$ergs respectively. The iodine molecule beam was run at 100 °C and in this case, for the same potassium velocities, the mean relative energies were 0.091, 0.193 and 0.331 $\mu\mu$ergs. Sweeps were also carried out in the K/I_2 case with a main beam velocity of $6.7\alpha 4$ cm/sec i.e. a mean relative energy of 0.135 $\mu\mu$ergs.

The crude scattering measurements were processed in the manner described and sweeps made at the same relative velocity were then normalized and averaged. The final results for each relative velocity are shown in Figs. 5.2. to 5.4. for K/I, 5.6 to 5.9. for K/I_2 and 5.10. to 5.11. for Na/I. Values of $S(\Theta).\Theta^{7/3}$ have been plotted as ordinates here rather than $S(\Theta)$ to reveal more clearly any quantum oscillations. The error bars which are 95% confidence limits are considered to arise from errors in angle measurements, error bars in individual sweeps before deconvolution being negligible (See Fig. 5.1.)

In view of the uncertainties in the overall shapes of the averaged, unfolded scattering curves, only the positions of the peaks were used to determine the interactions. Whenever there was any uncertainty as to the existence of a peak on these curves, an examination of all sweeps making up that average was made. Fig. 5.12. shows the peak positions for all six sweeps comprising Fig. 5.2., together with the peaks given by Fig. 5.2. As can be

seen most of these averaged peaks appear on all individual plots. Such a peak summarizing plot gives an experimental positioning error of less than 1 step i.e. 0.05° for each peak.

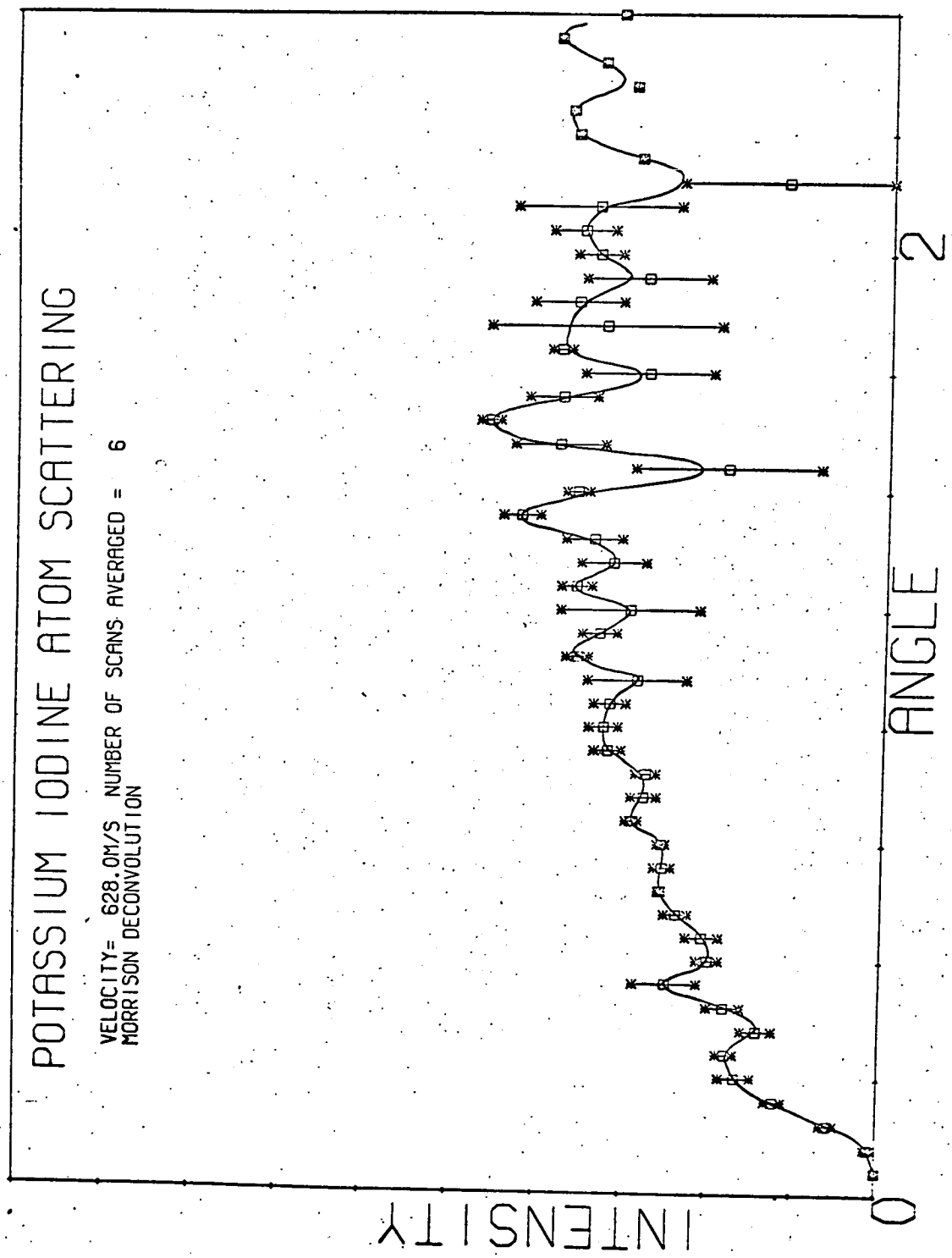

Fig. 5.2. Experimental cross-sections for K-I collisions.

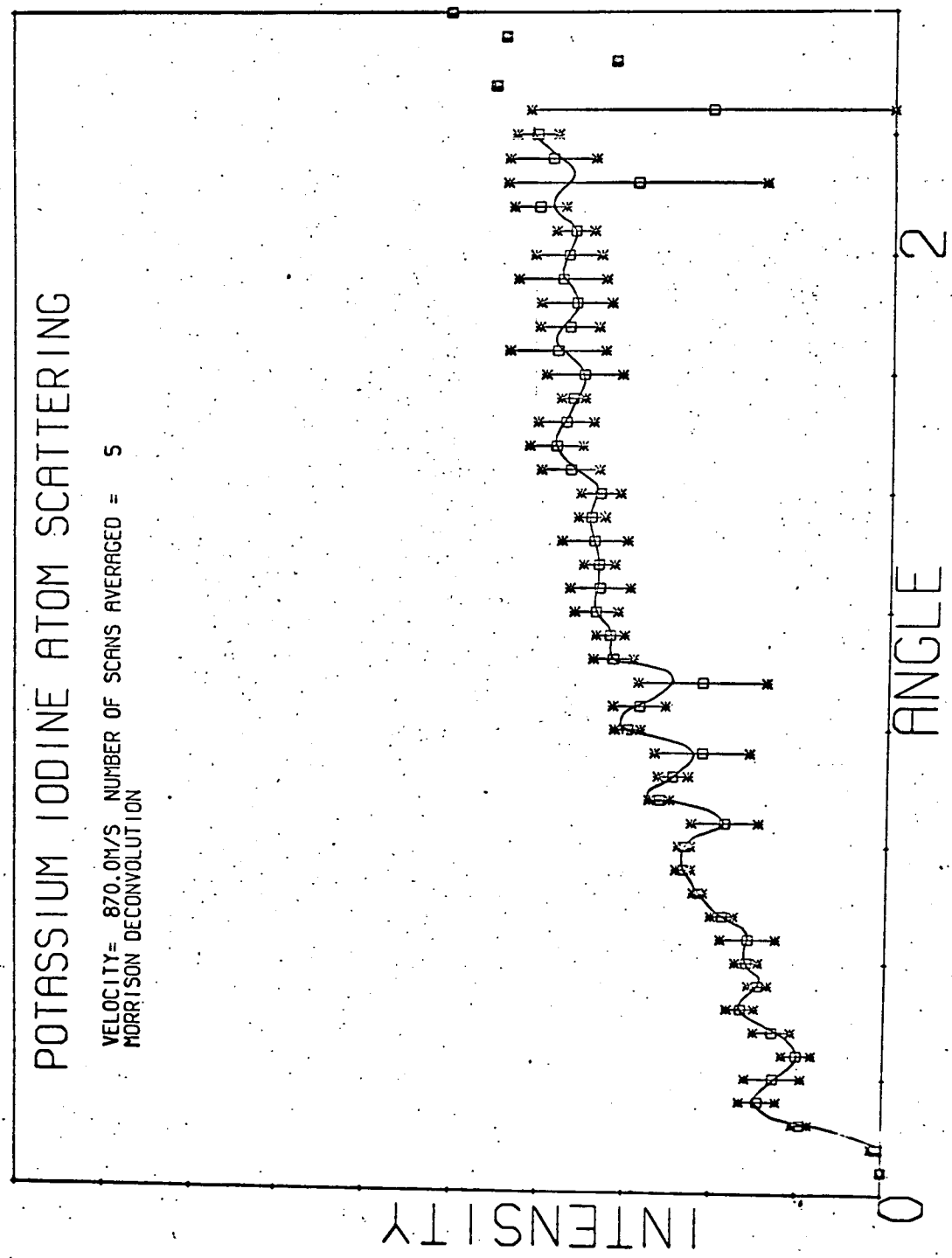

Fig. 5.3. Experimental cross-sections for K-I collisions.

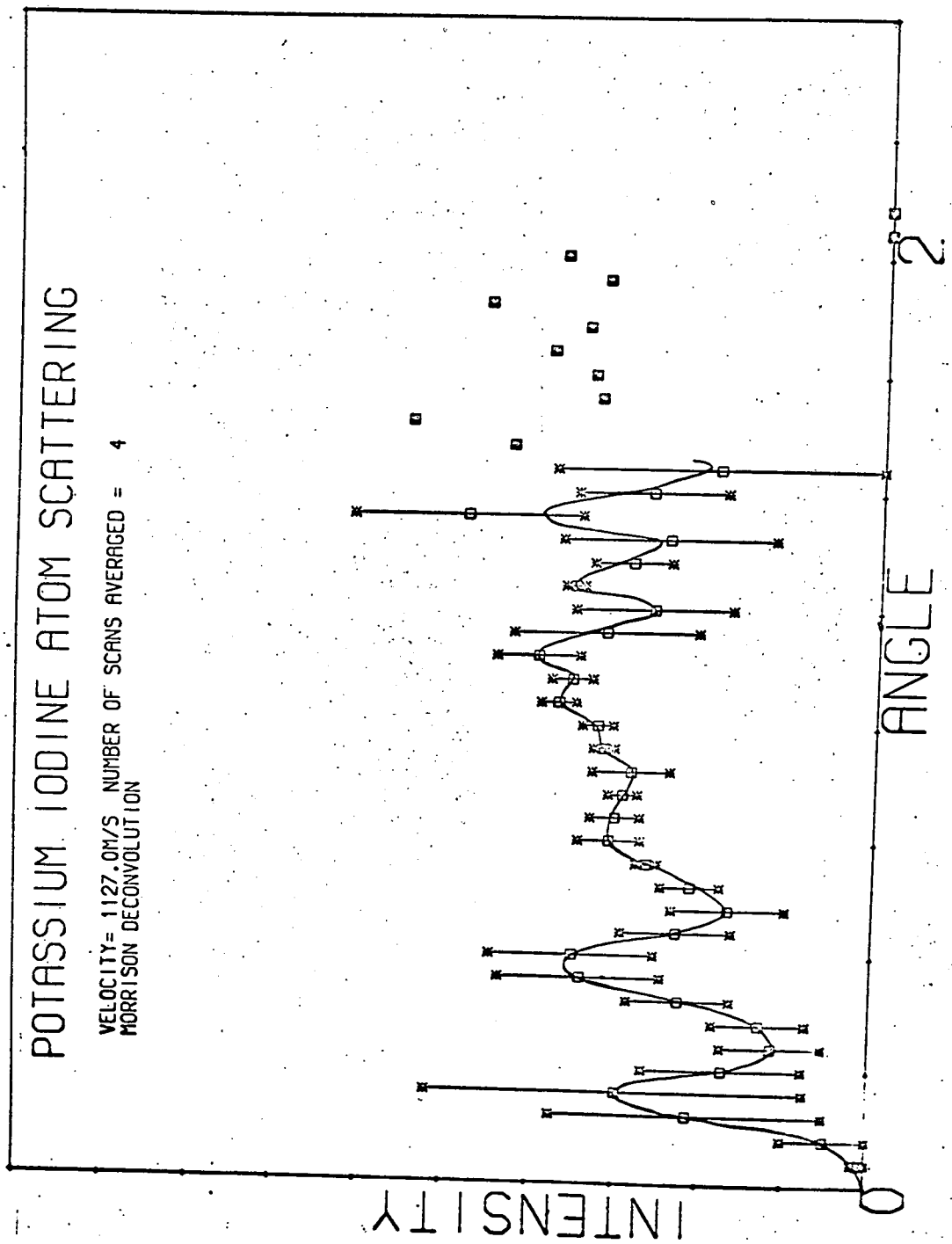

Fig. 5.4. Experimental cross-sections for K - I collisions.

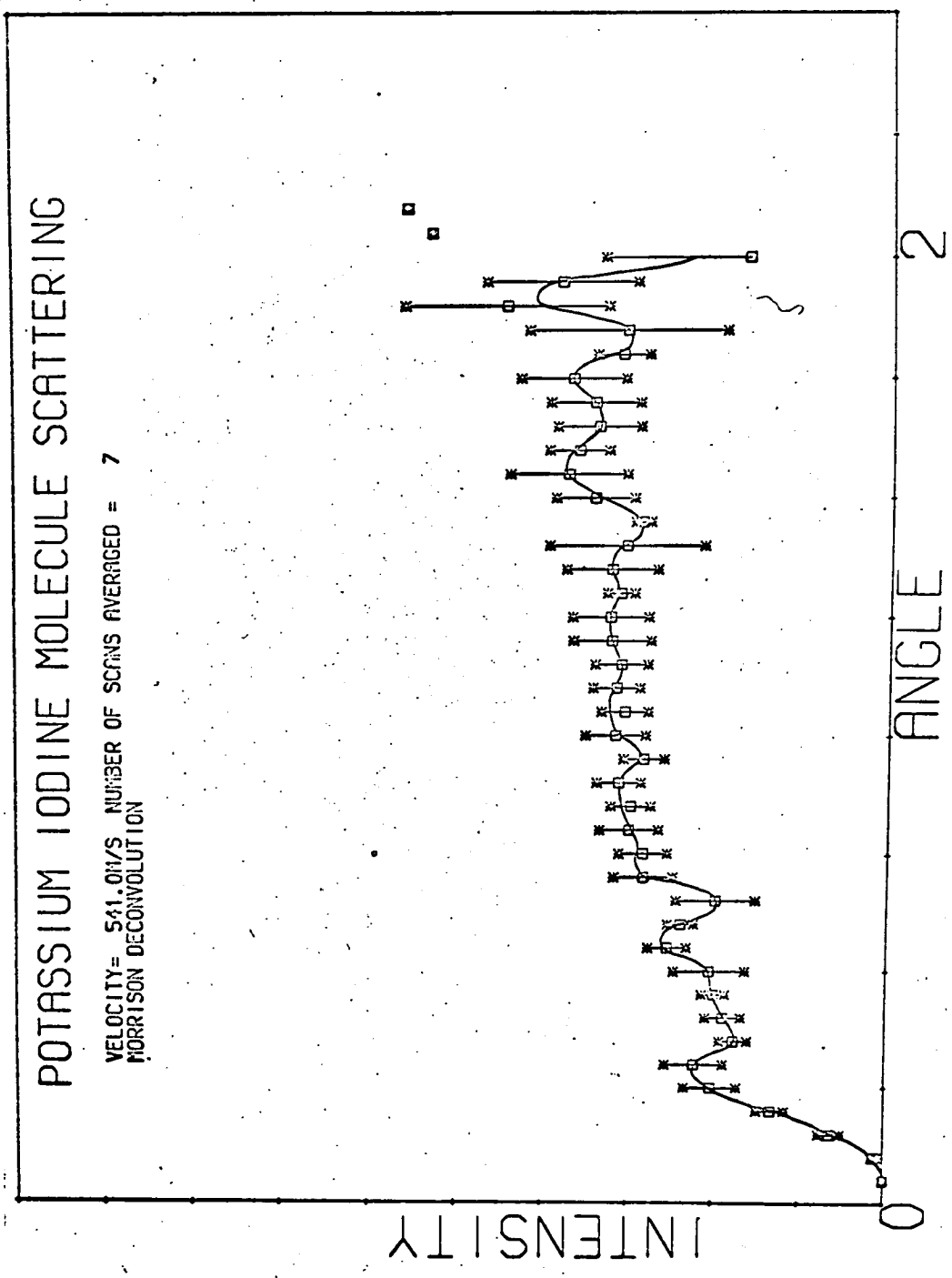

Fig. 5.6. Experimental cross-sections for K-I_2 collisions.

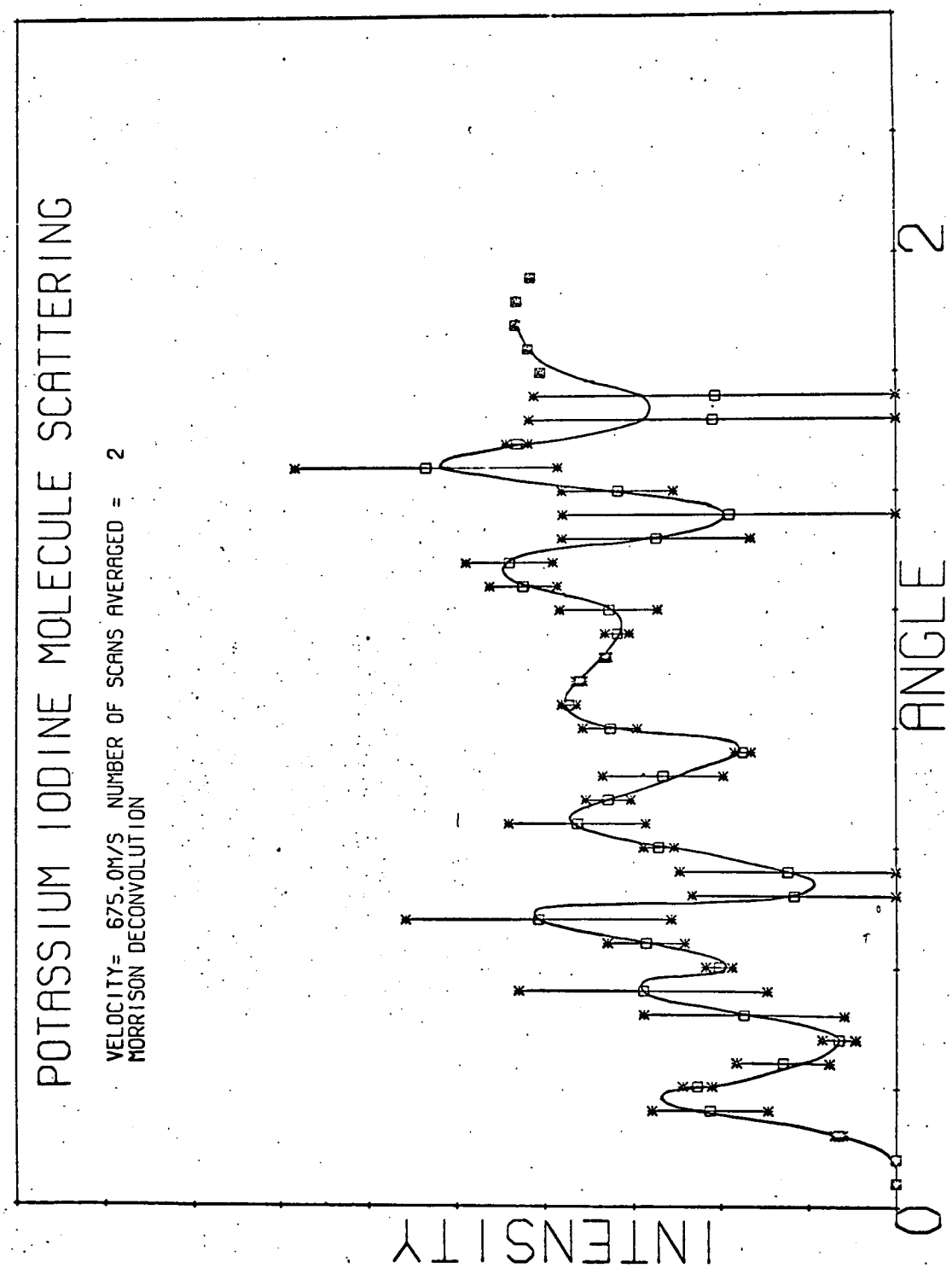

Fig. 5.7. Experimental cross-sections for $K\text{-}I_2$ collisions.

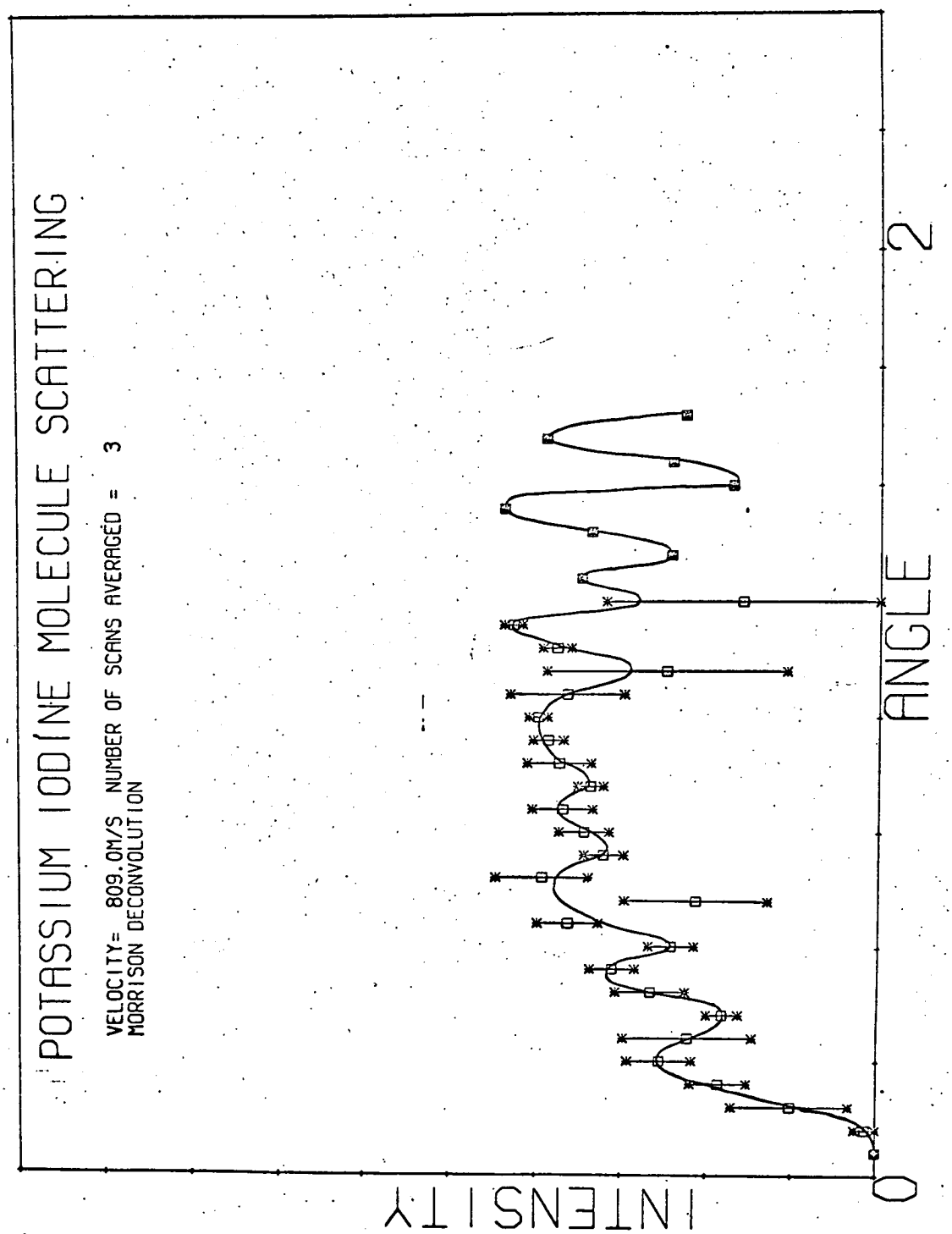

Fig. 5.8. Experimental cross-sections for $K-I_2$ collisions.

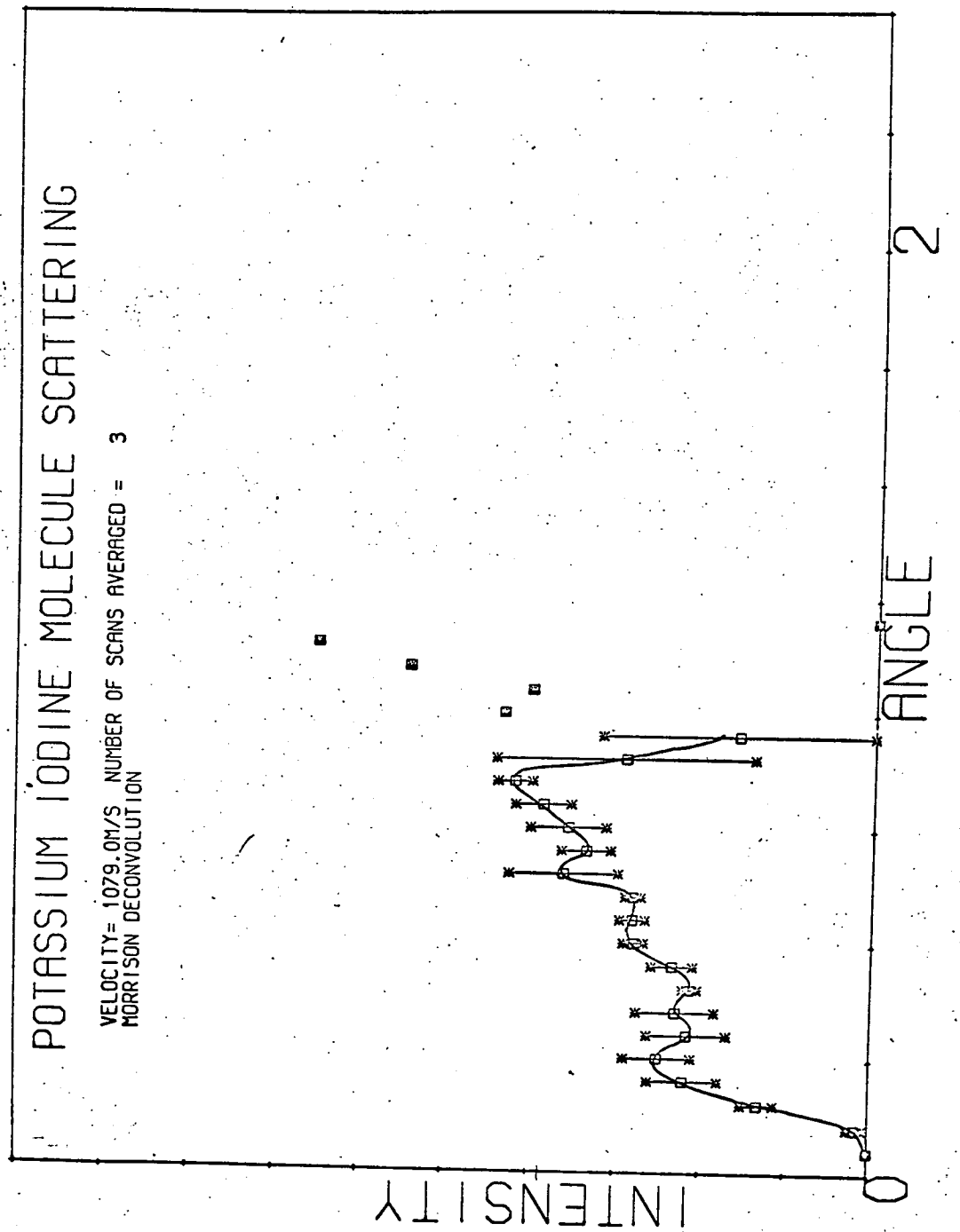

Fig. 5.9. Experimental cross-sections for $K-I_2$ collisions.

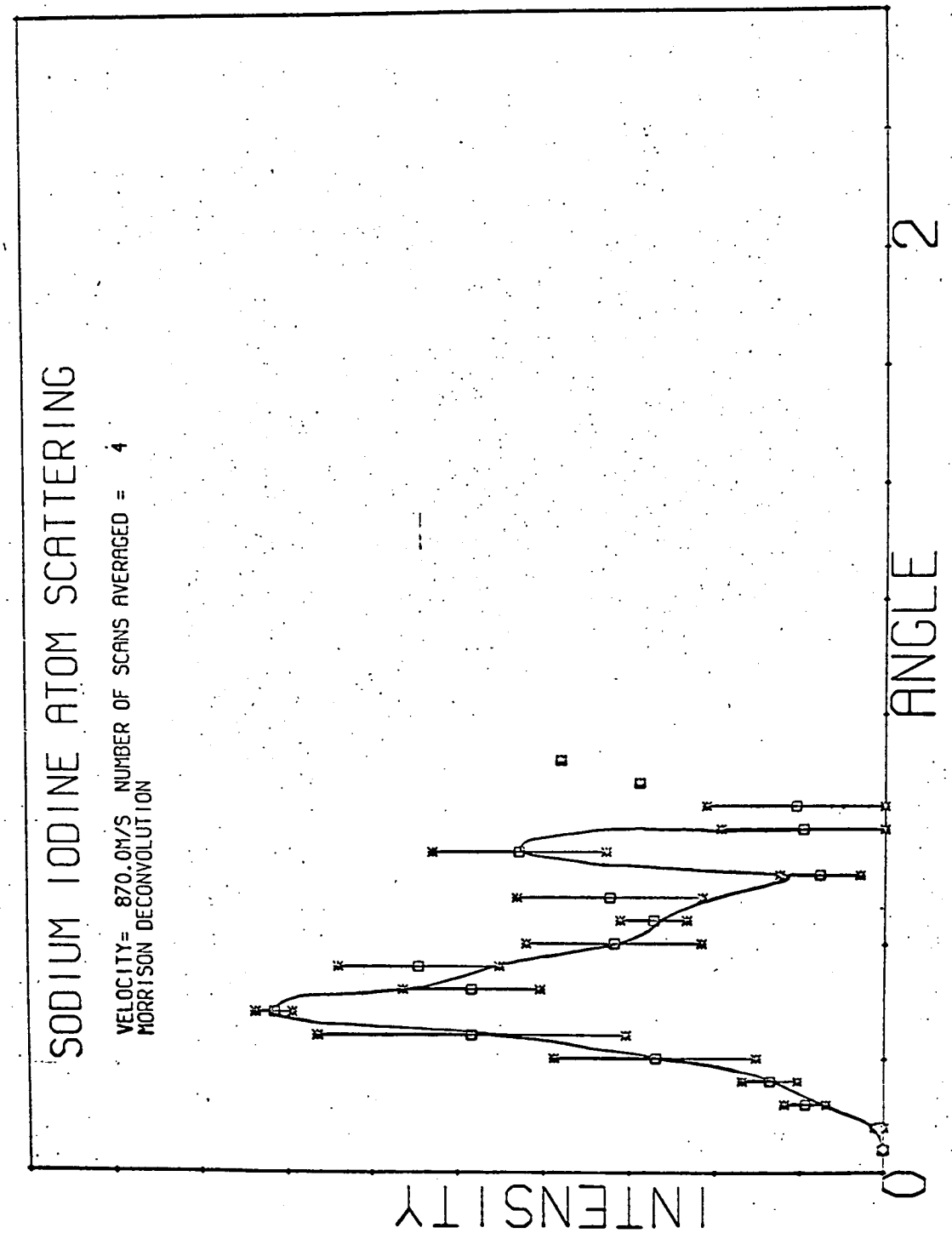

Fig. 5.10. Experimental cross-sections for Na - I collisions.

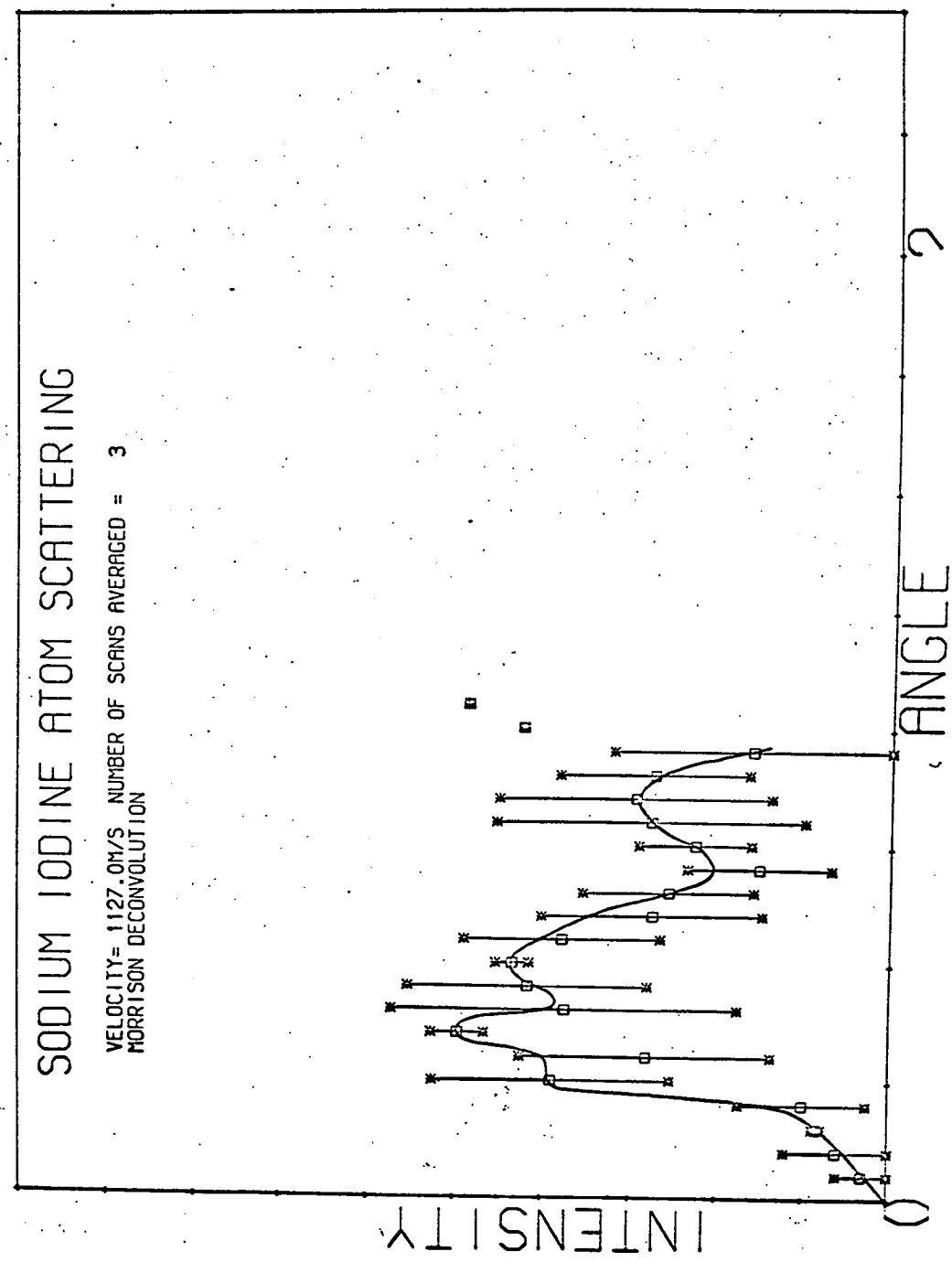

Fig. 5.11. Experimental cross-sections for Na - I collisions.

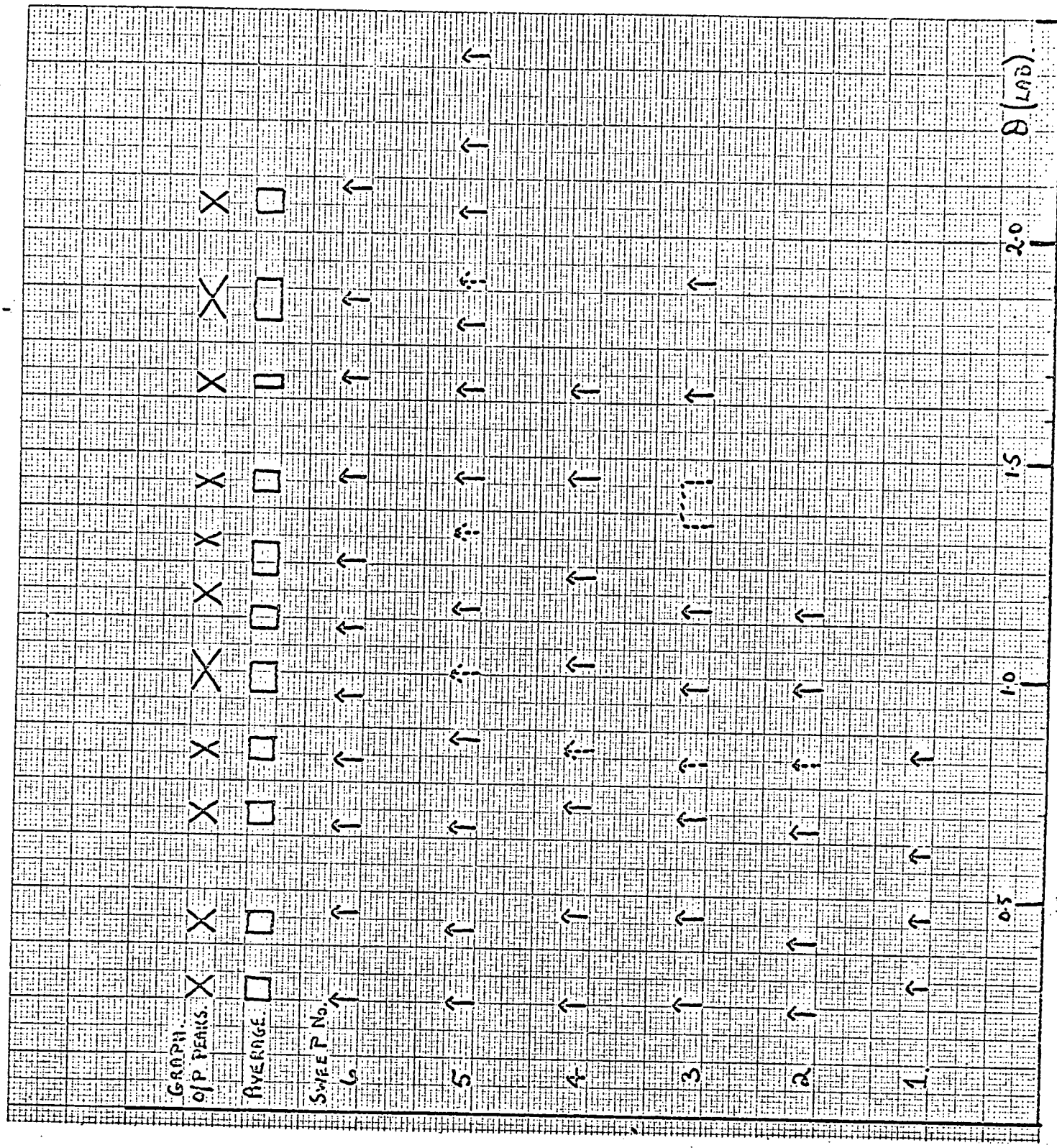

Fig. 5.12. Peak position plot for individual K-I sweeps at 0.098 μergs.

Total Cross-Section Results.

Crude total cross-section measurements were also made for the K/I and Na/I cases.

As defined in Chapter 1, the main beam intensity is attenuated by the cross-beam according to the Beer's Law relation

$$I(0) = I_0(0) \exp(-n \sigma_{tot}(g) L) \qquad (5a)$$

where n is the particle density of the cross-beam, L is the length of the scattering volume and $\sigma_{tot}(g)$ is the total cross-section. The latter is a function of g the relative velocity. Thus by comparing the log of I/I_0 against g, we are able to map out the energy dependence of the relative total cross-section.

$\sigma_{tot}(g)$ is related to the differential cross-section by

$$\sigma = \int I(\Theta, \Phi, g)\, d\Omega \quad \text{where } d\Omega = \sin\Theta\, d\Theta\, d\Phi \qquad (5)$$

According to this equation all scattered particles contribute to the total cross-section. This is not entirely true in a real apparatus with a beam and detector of finite dimensions where the measured effective cross-section is too small by an amount which depends on the resolving power of the apparatus. The error in σ is given by

$$\Delta\sigma = \int_{\Delta\Omega} I(\theta, \phi)\, d\Omega \qquad (6)$$

where the integral extends over the solid angle characterizing the apparatus resolution. Because long range attractive forces lead to a concentration of scattering in the forward direction, the elastic differential cross-section rises rapidly with decreasing angle but becomes nearly independent of angle at angles smaller than a characteristic limiting angle, α_0. Obviously if the error in the total cross-section is to be minimized the apparatus

resolving power must be less than this limiting angle which corresponds to the quantum mechanical uncertainty in the position of the particle during the collision event. In the centre-of-mass system α_0 is approximately given by

$$\alpha_0 = \frac{\hbar}{2\mu g}\sqrt{\frac{\pi}{\sigma}} \qquad (7)$$

If we take the total cross-section, σ, as 1000Å^2, this leads to a critical angle of 3 minutes of arc for our lowest experimental velocity. According to Pauly and Toennies (PAU 65) if the resolving power of the apparatus is of the order of magnitude of this limiting angle (transformed into the laboratory system) the error in the measured total cross-section is of the order of 5 to 10%. In order to measure the total cross-section with an error smaller than 1% they advocate that the angular resolution ought to be 1/10 of the LAB critical angle.

Since our apparatus uses rectangular beams with beam height much greater than beam width, the Kusch criterion (KUS 64) for calculating the resolving power may be used. In Kusch's calculations the efficiency of the detector is defined by $\eta = I'/I$ where I' is the intensity, measured at the detector, of beam molecules that have been scattered through an angle, θ while I is the detected intensity of these same molecules without scattering. For example $\eta(\theta) = 1$ implies that none of the molecules that have been scattered through an angle θ are counted as having been scattered. The resolving power θ_0 is then defined as the smallest scattering angle for which $\eta(\theta)=\frac{1}{2}$. For the particular geometry of our apparatus, the resolving power is approximately 8 mins. of arc.

Thus α_0 is less than θ_0 i.e. the critical angle at which $I(\theta)$

becomes independent of angle is less than the resolving power of the apparatus so that our measurements of total cross-section will be too low by some percentage depending on I (θ). Looking at the results on total cross-section as a function of resolving power quoted by Pauly (PAU 59), it is however doubtful if this error will be much greater than around 30%. Though the error itself will be a function of relative velocity our measurements ought to give some idea of the velocity dependence of the total cross-section. Certainly they ought to reveal any deviation from a -0.4 slope as large as a - 2 slope in the log-log plot.

The equation 5.5a , also applies only to the ideal situation in which the scattering gas is stationary before collision and the primary beam molecules have the same velocity. By velocity selecting our main beam we have achieved one of these conditions but the secondary beam has a thermal velocity spread. It is necessary, therefore to replace equation 5.5a , by

$$I(0) = I_0(0) \exp\left(- n \sigma_{tot(eff)}(v_1) L \right) \qquad (8)$$

This effective scattering cross-section, $\sigma_{tot(eff)}(v_1)$ where v_1 is the main beam velocity, can be calculated by averaging over the velocity distribution in the cross-beam provided the velocity dependence of the total cross-section is known. A correction factor can be defined by the equation

$$\sigma_{tot(eff)}(v_1) = \sigma_{tot}(v_1) F(x). \qquad (9)$$

where $x = v_1 / c_2$ and c_2 is the most probable velocity in the cross-beam. Such correction functions have been calculated by Berkling et al (BER 62) for a velocity dependent cross-section of the type

$$\sigma_{tot}(g) \sim g^{-2/s-1}$$

These functions have been tabulated for values of S as low as 3 where F (x) is constant and equal to unity, but no such calculations were done for a g^{-2} dependence as is possible in the K/I system. In view of the resolution

errors inherent in our results, no attempts were made to calculate a correction function F (x) for the S = 2 case. Instead no corrections were made for the cross-beam velocity spread. Theory outlined in Chapter 2. predicts that the thermal energy behaviour of the K/I total cross-section will be different from that of the Na/I case if the former system follows the adiabatic potential. The same theory also predicts that the Na/I total cross-section will show a velocity dependence characteristic of an r potential at these energies. A comparison of even the crude results should therefore reveal the potential dominating in the K/I case.

For each system the attenuated intensity was measured over as wide a range of velocity as possible with many measurements interspersed at one particular velocity for normalization purposes. Having rotated the turn-table to the main beam peak, data was recorded as for a single angle during a cross-beam sweep. These numbers were divided into arrays of cross beam on/cross beam off signals and the ratio of array averages taken as I/I_o.

Since the attenuation is a ratio of main beam intensities any drifts in the main beam will cancel out. Because log (I/I_o) is, however, a linear function of the cross-beam intensity, normalization corrections were made to this rather than to the direct ratio.

Plots of corrected log (log (I/I_o)) versus log (v_1) where v_1 is the main beam velocity are shown for both Na/I and K/I in Fig. 5.13. The gradient in the K/I case is almost but not quite the same as that in the Na/I case. Certainly they lie outside experimental error.

A least squares analysis yields for the gradients

For K/I Gradient $= -0.564 \pm 0.038$

For Na/I Gradient $= -0.468 \pm 0.012$

[Errors are 95% confidence limits].

Fig. 5.13. Total Cross-Sections. Plots of log Q v log v for Na/I and K/I.

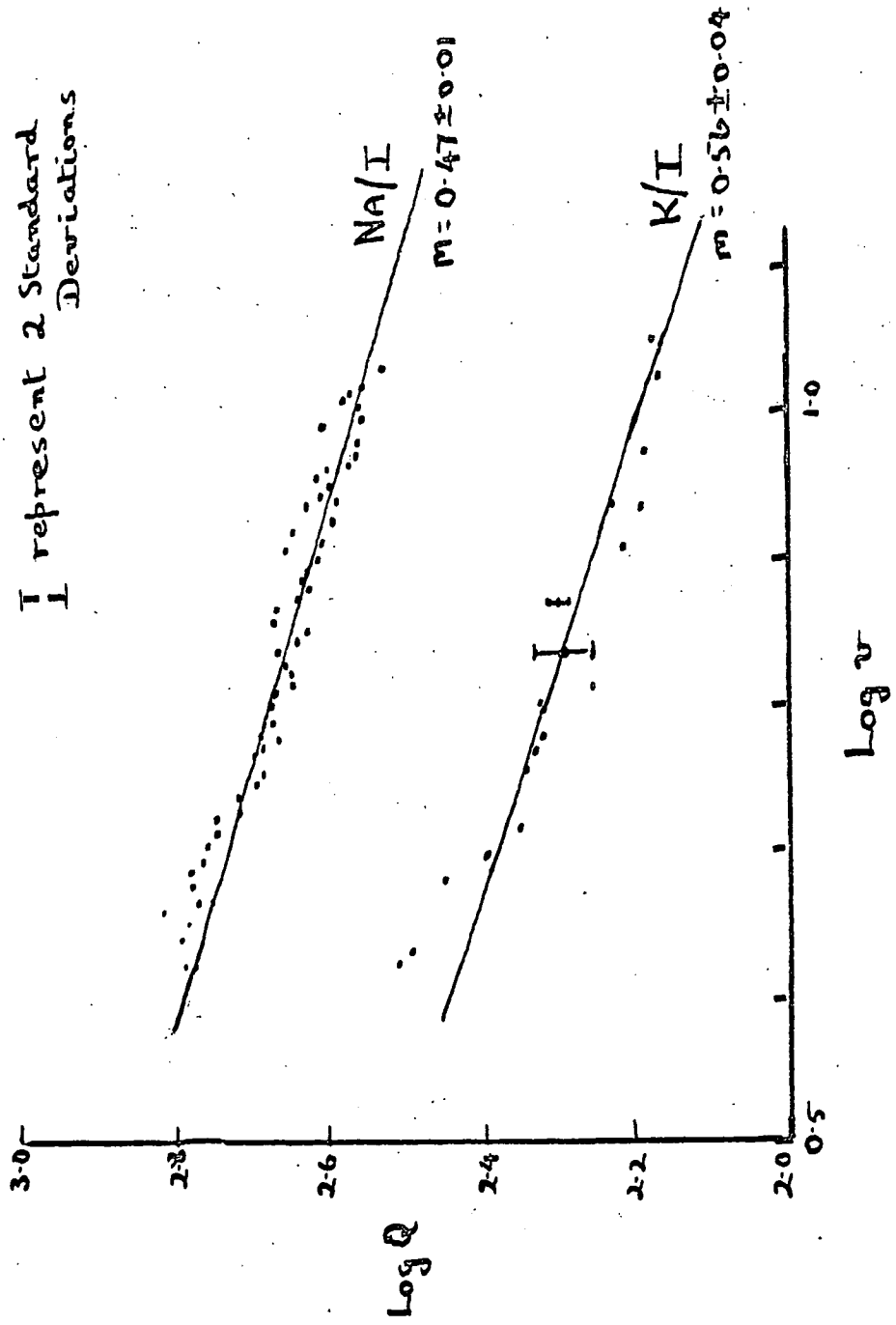

A full analysis of the Na/I results did not seem justified but assuming the velocity dependence was for an r^{-6} potential some approximate calculations were made.

These gave a gradient of -0.35 for the log-log plot. This leads to a value of 6.7 for S, which may be taken as 6 in view of the crudity of our results.

Crude though they may be, these measurements reveal that the K/I interactions are dominated by an r^{-6} dependence. The fact that the K/I gradient is larger than the Na/I one could be taken as a deviation from the -0.4 slope meaning some of the interactions were taking place along the adiabatic curve but I do not feel the data justifies this conclusion.

Potassium + Iodine Atom Scattering.

In Chapter 2, the following models were suggested for the K-I collision process.

(i) A single Lennard-Jones (n,6) potential.

(ii) A single adiabatic potential switching from r^{-6} to Coulombic at the crossing point.

(iii) A familty of covalent potentials.

(iv) An adiabatic potential plus one or more (12,6) potentials to account for the other possible interactions.

(i) and (iii) suggest a small interaction constant between the two states involved in the curve-crossing while (ii) and (iv) suggest a large interaction constant. A fifth model gives the interaction constant some intermediate value.

For any of these models to be acceptable they must reproduce the peak position plot shown in Fig. 5.15. this being obtained from Figs.5.2. - 5.4.

That model (ii) the single adiabatic potential is unacceptable is immediately obvious. The sharp and rapid oscillations (Fig. 2.7.) produced by this potential have proved to be almost independent of both the long range C_6 coefficient and the Coulombic potential model (Fig. 5.16). Monoenergy calculations which varied the width of the switching region from 0.1A downwards also had no great affect on peak positions in the angular range 0 to 2 degrees. Though the positions were altered slightly in all these cases, no change in angular frequency was ever observed. That the number of peaks produced by such a model is insufficient to account for those observed can be seen in Fig. 5.17. where the adiabatic peaks (as circles) are superposed on the experimental peak position plot.

Model (i) can just as readily be dismissed by the following argument.

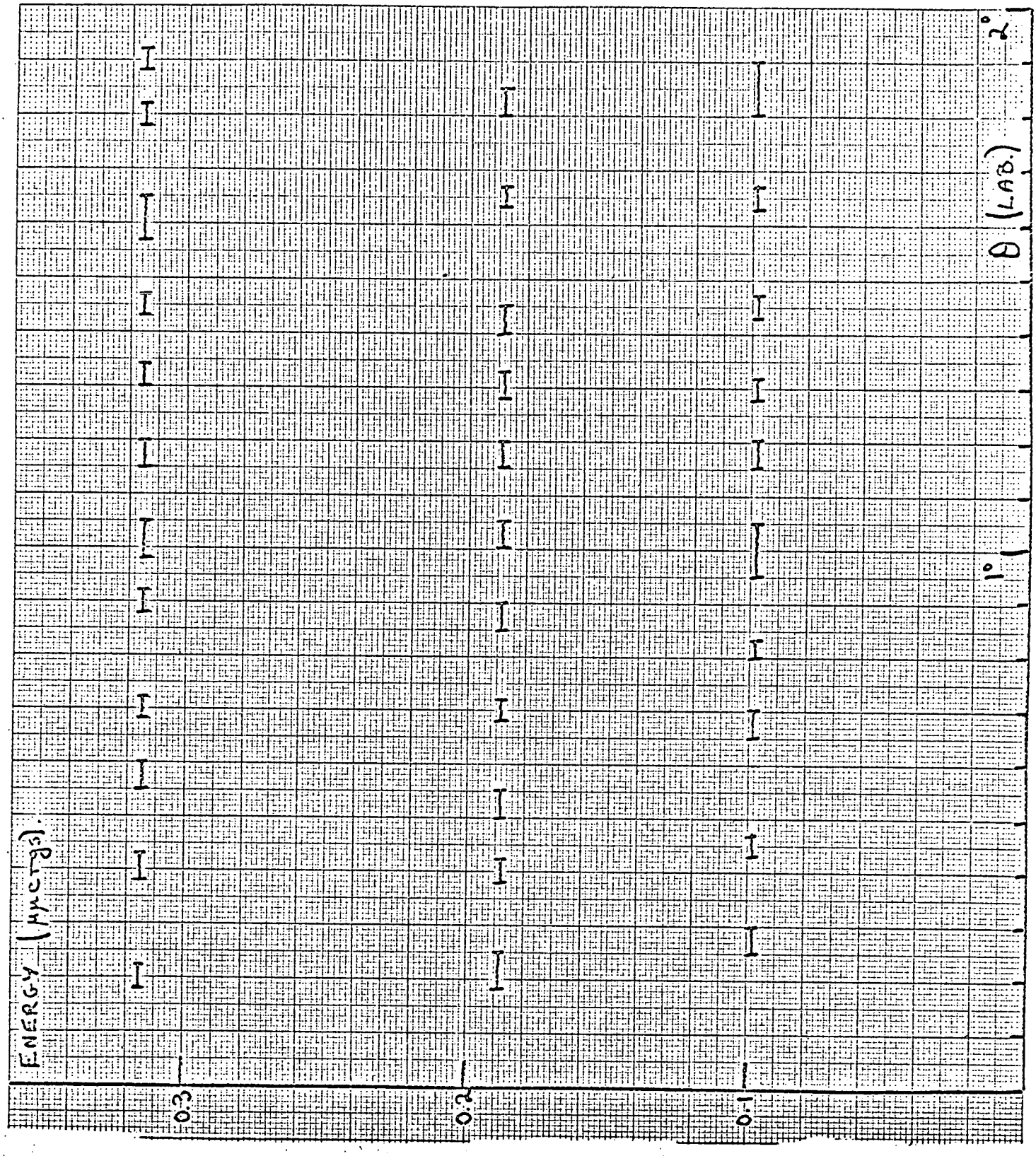

Fig.5.15. Experimental peak positions for K-I collisions.

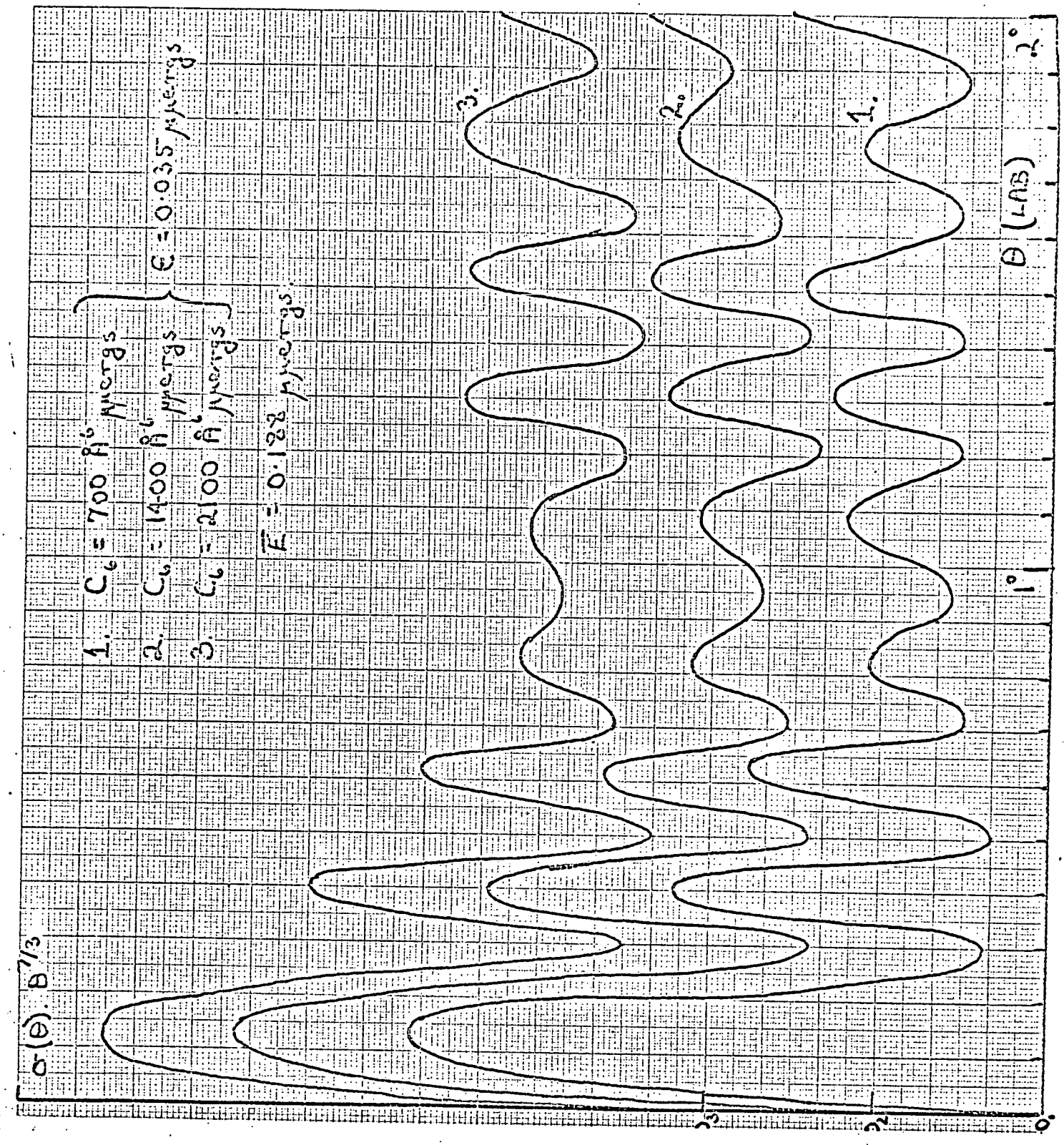

Fig. 5.16a. Variation of adiabatic potential dxsects with C_6 coefficient.

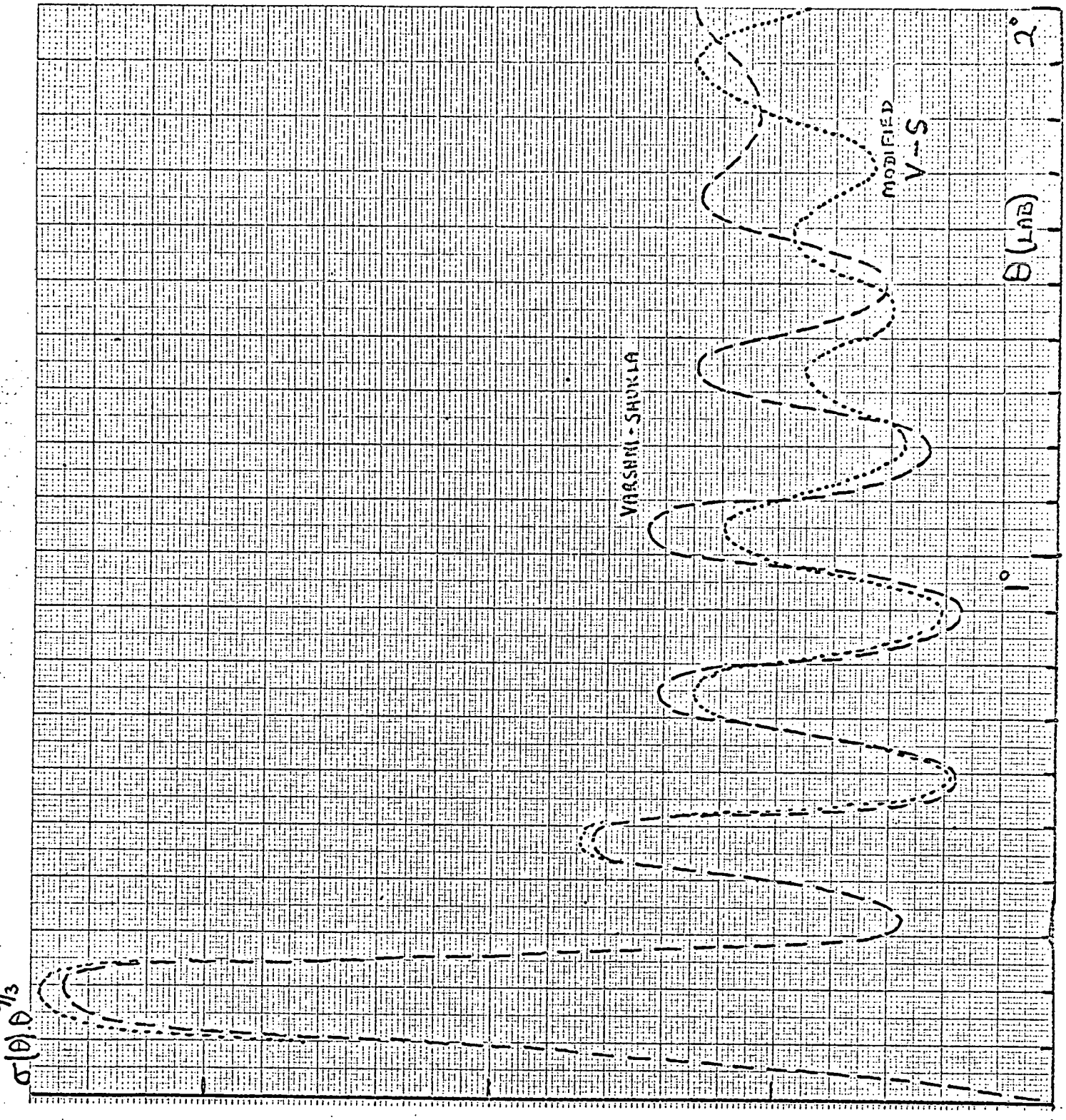

Fig. 5.16(b) Variation of adiabatic d x sects. with ionic potential model.

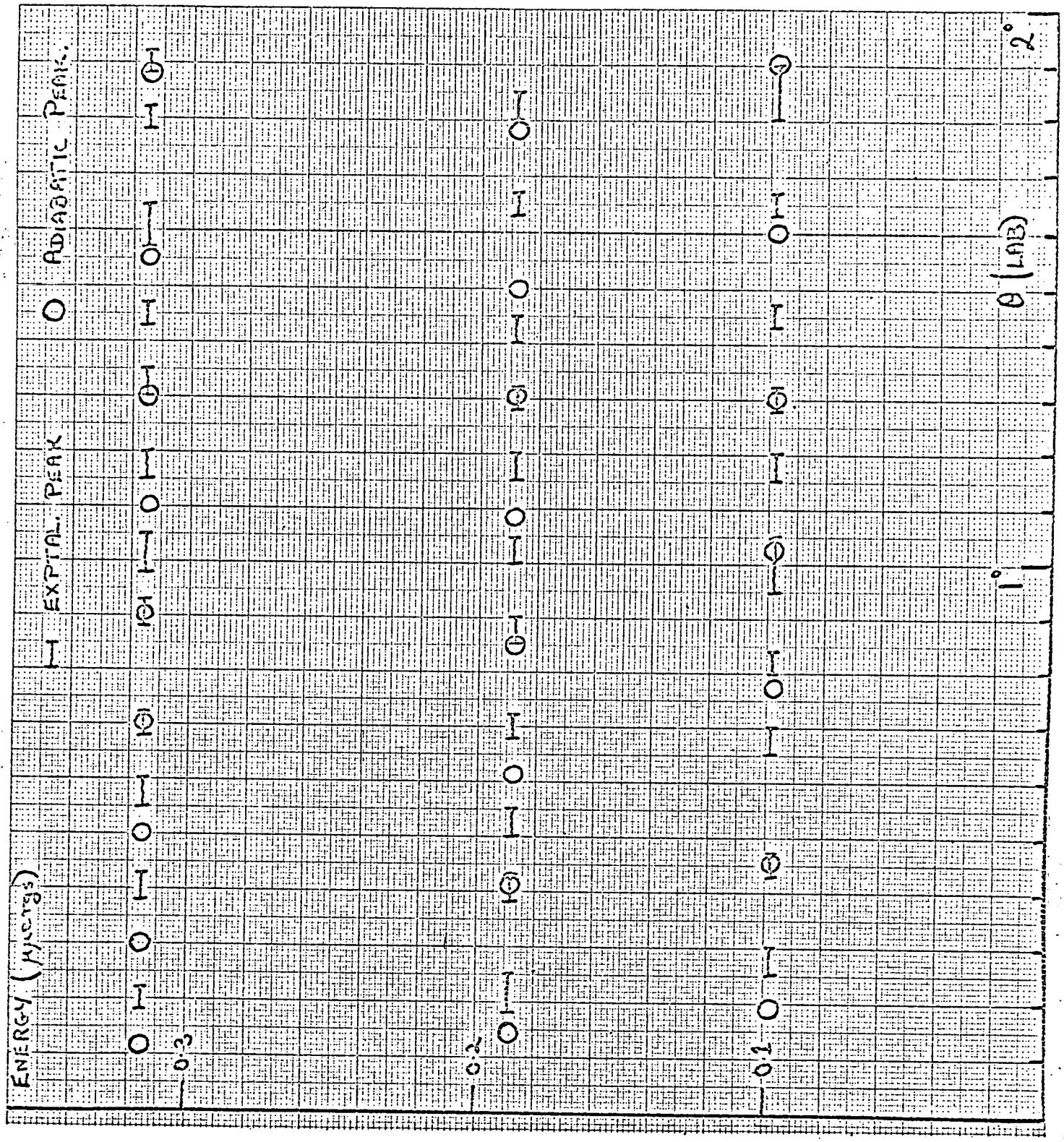

Fig.5.17. Comparison of experimental and adiabatic potential peak positions.

The angular spacing of the quantum oscillations can be simply related to a range parameter of the potential through the relations (COW 69)

$$\Delta\theta_{cm} = \pi/L^*$$

$$(L^* + \tfrac{1}{2})\hbar = \mu v a^*$$

Remembering that for K/I, $\theta_{cm} = 1.33\ \theta_{LAB}$, the experimentally observed peak spacings lead to values of a^* (in Å) of 26, 21 and 18 for the three experimental energies (lowest first). These values are based on the average peak spacings for as Table 5.1. shows the spacings can vary by up to 0.1 of a degree.

It seems most unlikely that any potential between potassium and atomic iodine would have a range parameter as large as 18Å. Both this and the somewhat irregular peak spacings lead to the conclusion that the K/I interactions are sufficiently different to require more than one model potential to represent them.

The same formulae applied to the peak spacings of the adiabatic potential lead to range parameters of 15,13 and 12Å at the three calculation energies. In this case also the successive peak spacings do not vary by more than 0.03 of a degree from the average at any energy.

Moving on to the next model (number 3), it was attempted to fit a family of covalents to the observed peak positions, ignoring the statistical weightings of each individual member for the moment. Accepting the long range spin orbit coupling as being of the JJ type, gives a choice of up to three states if the 0^+ and 0^- states are taken together. It was also felt that the long range behaviour of these states could as a first approximation be taken as sufficiently similar for these three states to be described by a

Table 5.1.

K/I Peak Positions & Spacings

	Position	Spacing		Position	Spacing
$\bar{E}$ = 0.098	0.27	0.18	$\bar{E}$ = 0.188	0.22	0.18
	0.45	0.22		0.40	0.12
	0.67	0.14		0.52	0.18
	0.81	0.19		0.70	0.17
	1.00	0.17		0.87	0.16
	1.17	0.13		1.03	0.14
	1.30	0.15		1.17	0.13
	1.45	0.20		1.30	0.12
	1.65	0.20		1.42	0.23
	1.85			1.65	0.17
				1.82	

	Position	Spacing
$\bar{E}$ = 0.315	0.20	0.20
	0.40	0.17
	0.57	0.13
	0.70	0.20
	0.90	0.11
	1.01	0.16
	1.17	0.15
	1.32	0.13
	1.45	0.16
	1.61	0.19
	1.80	0.10
	1.90	

single C_6 coefficient. This was given our accepted value of 1400Å^6 $\mu\mu$ergs. The three potentials differed therefore only in the well-depth assigned to them.

Using the program 'Delilah', since the calculations were for direct comparison with experiments, energy averaged differential cross-sections were computed for a grid of LJ (12,6) well-depths ranging from 0.001 to 0.1 $\mu\mu$ergs at the three experimental energies. At first no covalent potential could be found which would produce the second experimental peak. However, by continually decreasing (and also increasing r_m since C_6 is constant), this peak was obtained with a well-depth of around 0.001 $\mu\mu$ergs, this corresponding to an r_m value of about 9Å. Even this well depth is not entirely satisfactory since the energy dependence of the peak is somewhat less steep than is observed experimentally.

However, accepting this potential as a strong candidate, the remainder of the grid was scanned to find a possible second and third series of peaks whose introduction would account for all the experimentally observed peaks. It was found that several combinations of two well depths, 0.001 and another, accounted for all of the peaks at the two higher energies but provided insufficient peaks for the lowest energy. The third potential was therefore necessary, making up the total spectroscopic series 0, 1 and 2. with the 0^+ and 0^- assumed similar enough to be represented as 0. Again several choices presented themselves though not as many as might first be thought, since, though a potential must help to account for the observed peaks, it must not introduce peaks where there are none. Fig. 5.18. shows that between them the well-depths 0.001, 0.003 and 0.008 or 0.001, 0.008 and 0.01 $\mu\mu$ergs provided peaks corresponding to the experimental ones at the three energies. No claim is made that these are the only possibilities for the three well depths for doubtless many more could be found at the expense of a great deal of

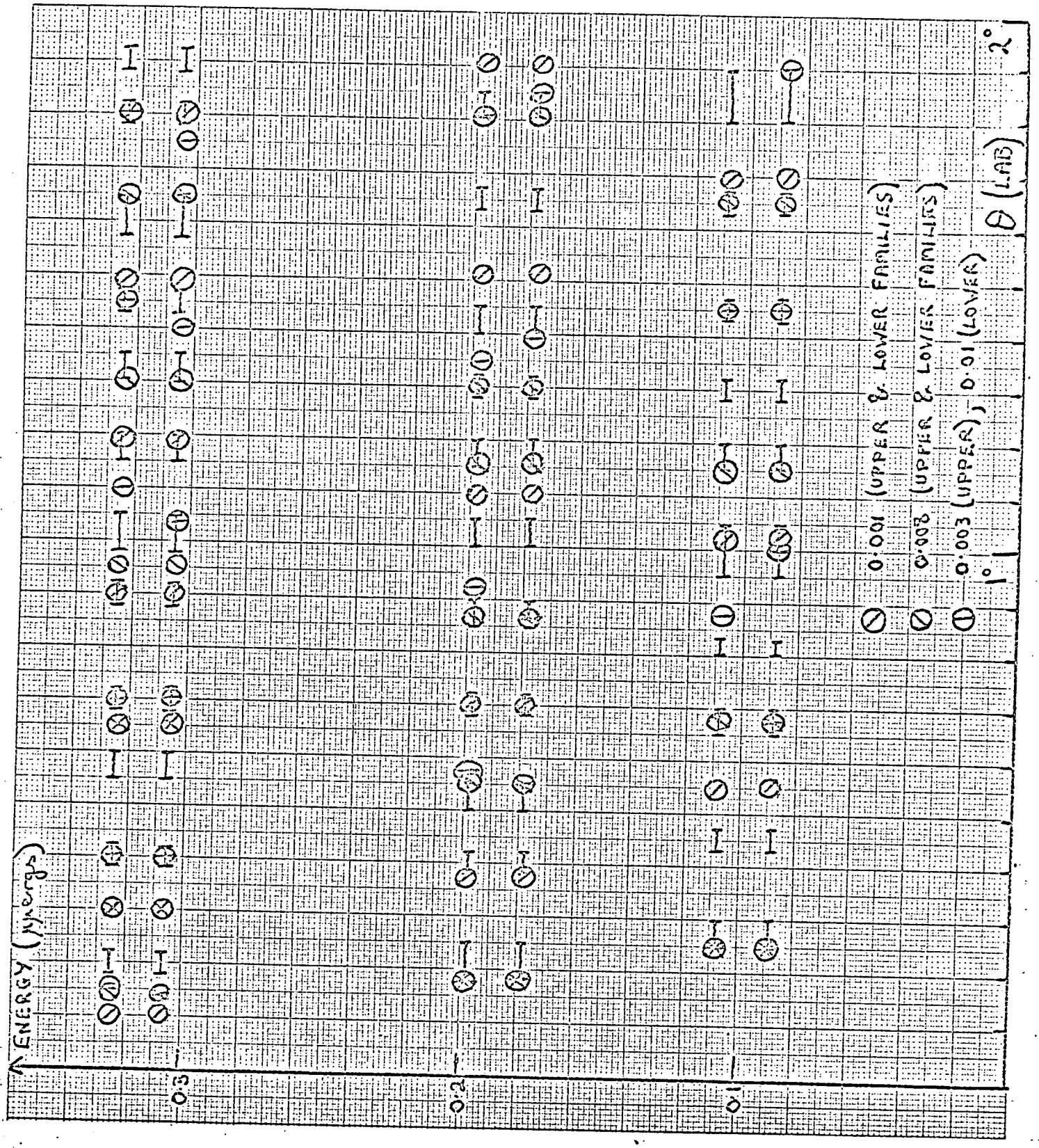

Fig. 5.18. Comparison of experimental and covalent peaks. For each family of potentials the energy ordinate has been displaced. Exptal. peaks are shown thus ⊢⊣

computer time.

With the first family appearing the more promising, it only remained to see if all of these peaks were prominent when the contributions to the 'observed' calculated differential cross-section were averaged, weighted according to the jj coupling scheme. The answer to this is that some were enhanced or widened but unfortunately some were smeared out entirely. Fig.5.19. shows what happened at the lowest energy when this averaging was carried out. The result is a curve similar to any of its contributions and could probably be obtained from the same LJ (12, 6) potential model with a suitable well-depth. Similar graphs were obtained at the other energies (Fig. 5.20. and 5.19.)

Though this family model failed because the number of peaks it produced was insufficient to account for the total seen in experiment, it was also unsatisfactory for a more physically appealing reason. This was the necessity of invoking a shallow-welled potential with a hard sphere radius of approximately 8 Å, a most unlikely value for the sum of two atomic radii.

One general point emerging from these calculations is that in cases where more than two potentials are operating the small angle scattering can at most hope to give the parameters for an 'effective' potential for the collision event. In view of this model (iv) which involves an adiabatic potential with a number of covalents to make up the spectroscopically possible series was treated as one with an adiabatic potential and an 'effective' covalent potential to account for all three possible excited state interactions (0^-, 1 and 2).

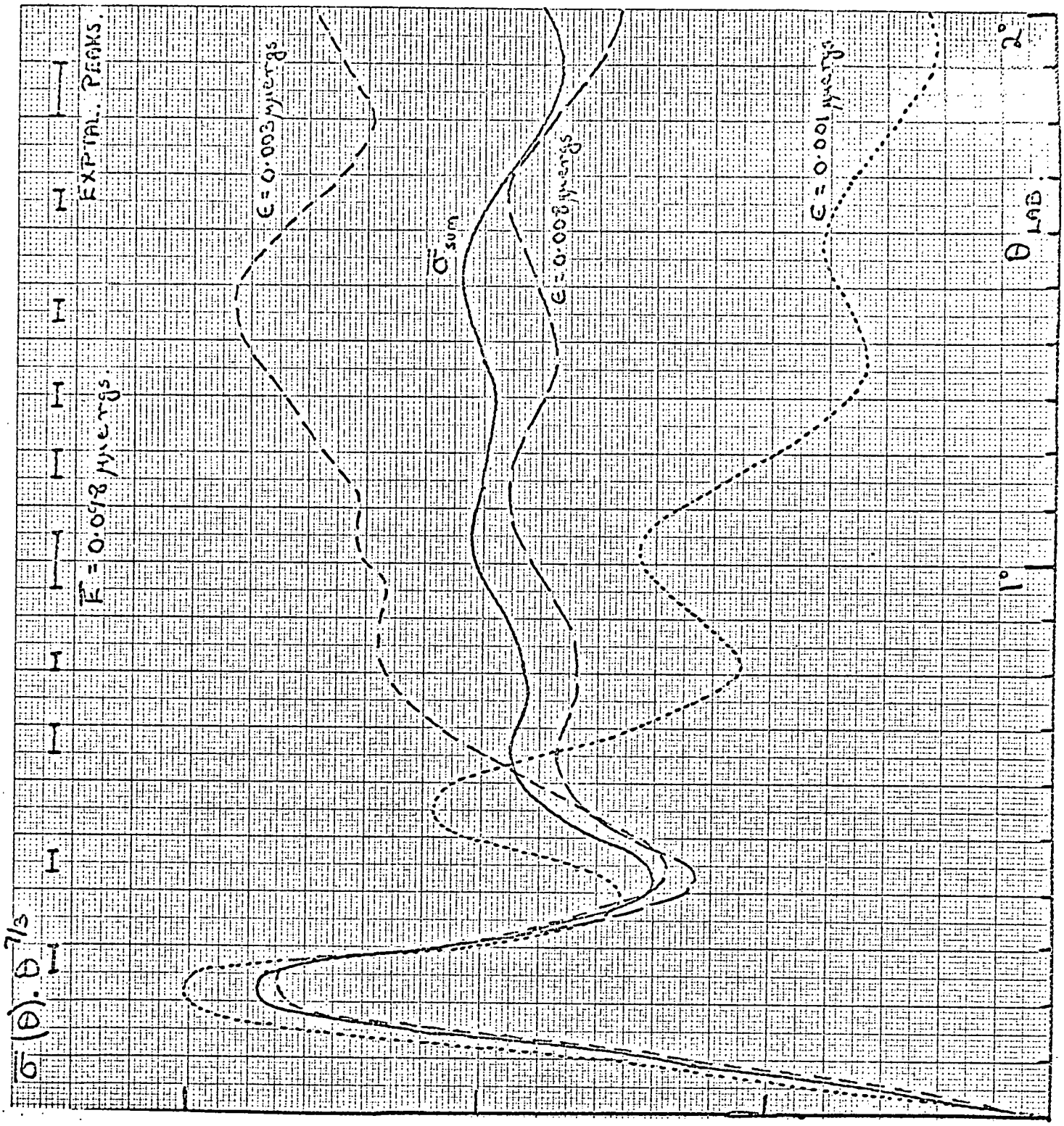

Fig. 5.19. Energy averaged cross-sections for K-I Collisions. First family of covalent potentials (ϵ = 0.001, 0.003 and 0.008 μergs).

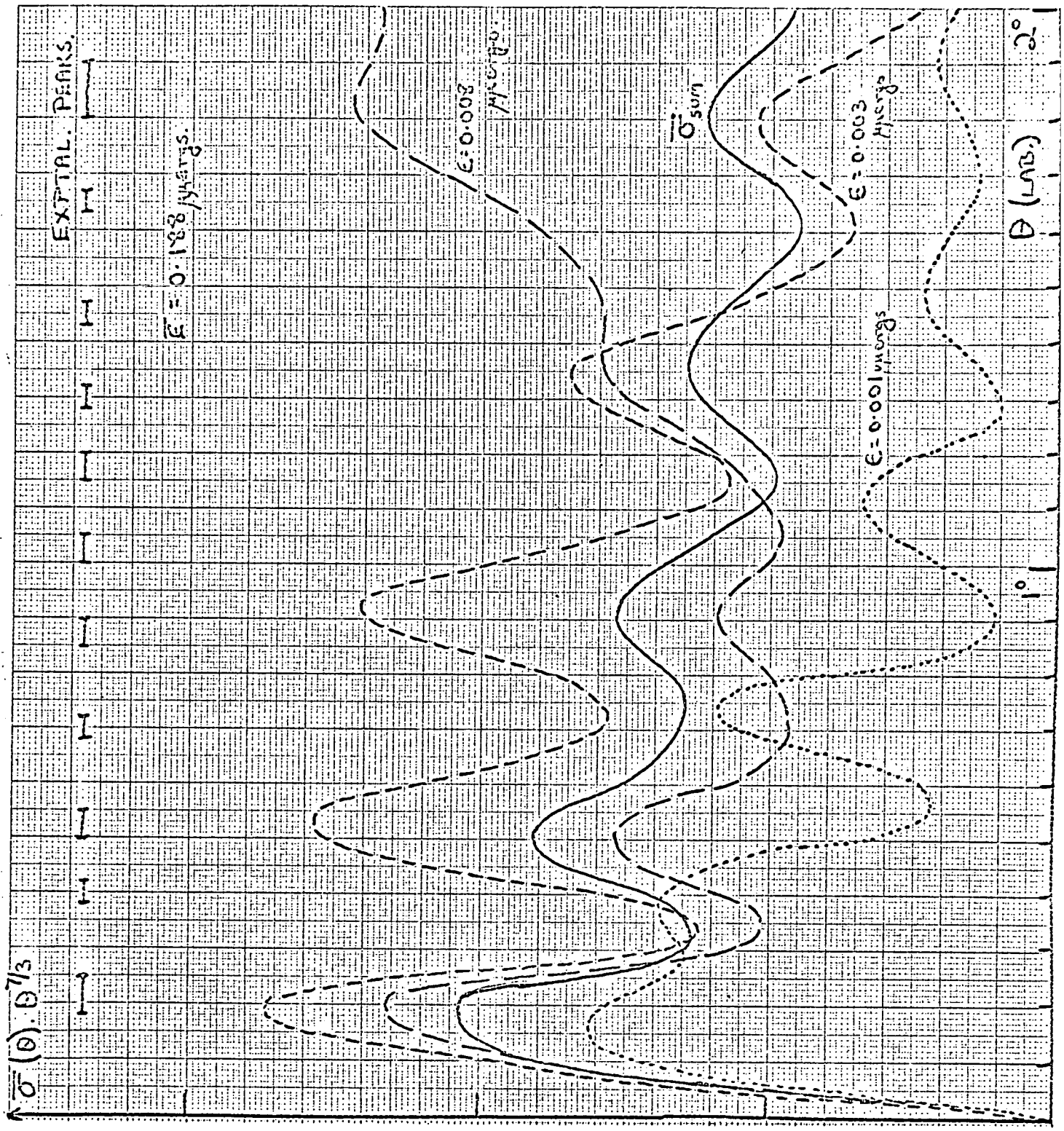

Fig.5.20. Energy averaged cross-sections for K-I collisions. First family of covalent potentials (ϵ = 0.001, 0.003 and 0.008 ergs).

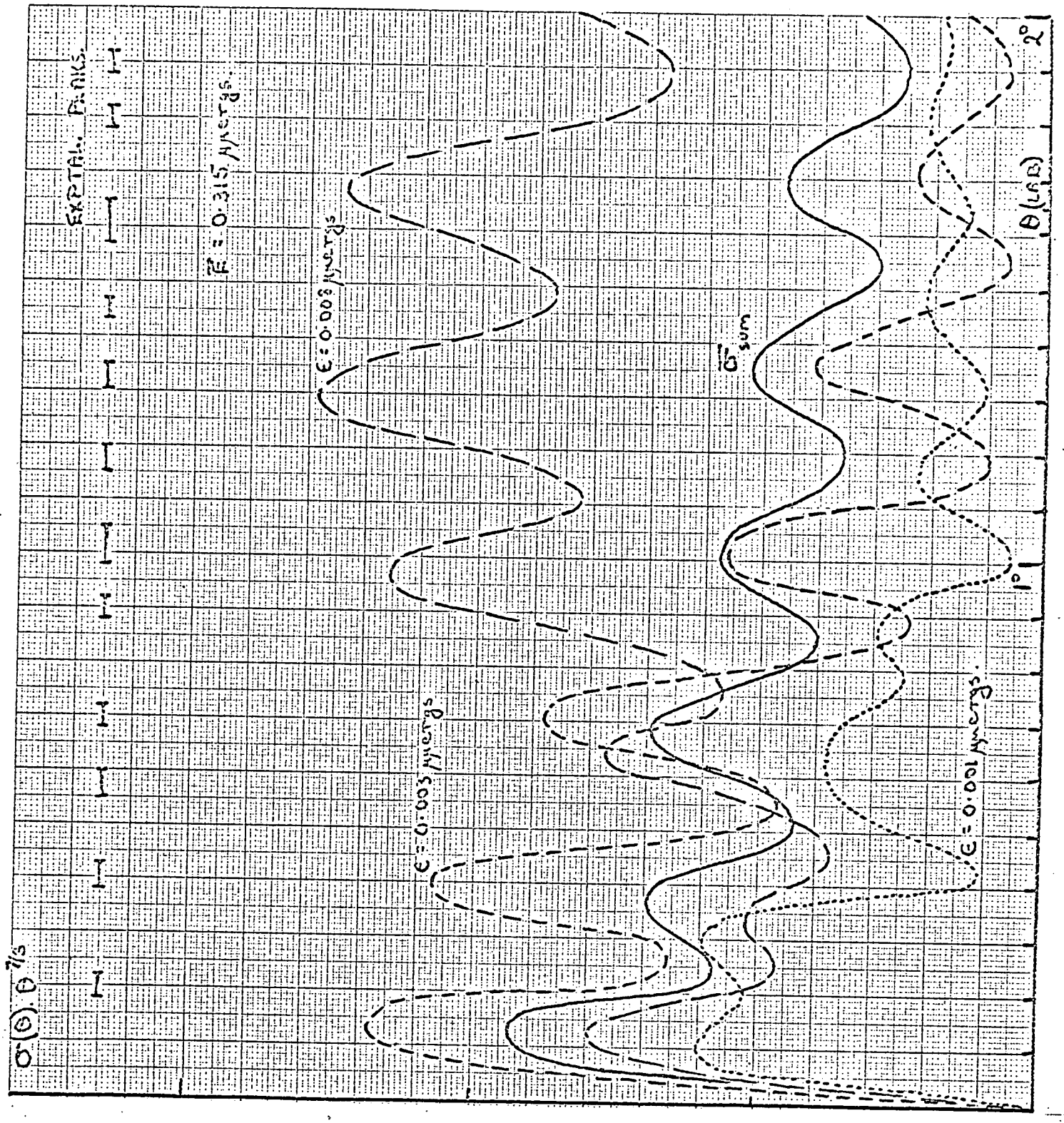

Fig.5.21. Energy averaged cross-sections for K-I collisions. First family of covalent potentials (ϵ = 0.001, 0.003 and 0.008 μergs).

This model was attractive from the first involving as it did the strong high frequency oscillations obtained with the adiabatic potential. Moreover the energy dependence of the experimental second peak was matched exactly by that of the corresponding adiabatic peak. Again initially ignoring the weightings of the contributions, a covalent potential (model LJ (12, 6) with $C_6 = 1400$) was sought to account for all of those peaks not accounted for by the adiabatic interaction. The results of calculations obtained for the previous model proved useful in this respect and well depths of 0.01, 0.02 and 0.05 $\mu\mu$ergs appeared as suitable candidates, with as is shown in Fig. 5.26, 0.05 appearing the strongest.

The question of weighting the relative contributions of the two potentials to the differential cross-section now arose. Theoretically transfer to the ionic curve can occur only from a state of the same symmetry and this is in this case an 0^+ state. The 0^+ state has a weighting of 1/8, the other covalents taking $\frac{7}{8}$ of the colliding pairs. Thus, if the spin quantum number S is a good quantum number in this situation, a maximum contribution of $\frac{1}{8}$ can be anticipated from the adiabatic curve. Should spin not be conserved then the weightings of the two states must be found by trial and error. Figs. 5.27 - 5.29. show what happened at the three experimental energies when the contributions were added together with statistical weighting. Also shown above on these graphs are the experimental peak positions. From these it can be seen that though the two potentials account for most of the observed peaks, exceptions occur on both the lowest and middle energy. Thus the peaks at 1.45° on the lowest and at 1.65° in the middle energy are not among those produced by the fitted potentials. We have not yet, however, optimised on the value of the C_6 coefficient and it may be that variations here will eventually produce the complete spectrum of peaks.

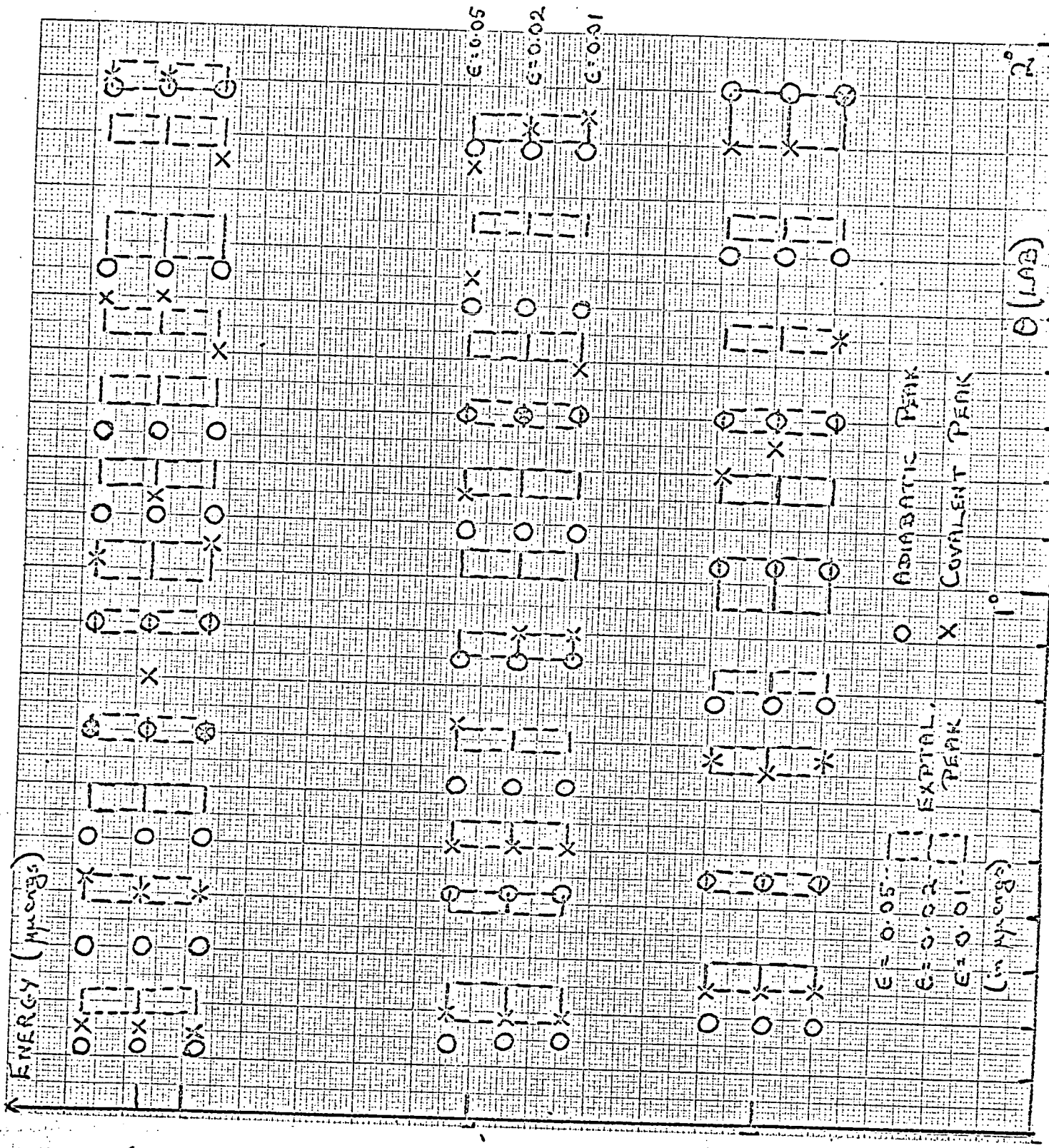

Fig.5.26. Comparison of experimental and theoretical peak positions for three different covalent well-depths. The energy ordinate has been displaced for clarity for each well-depth/adiabatic combination.

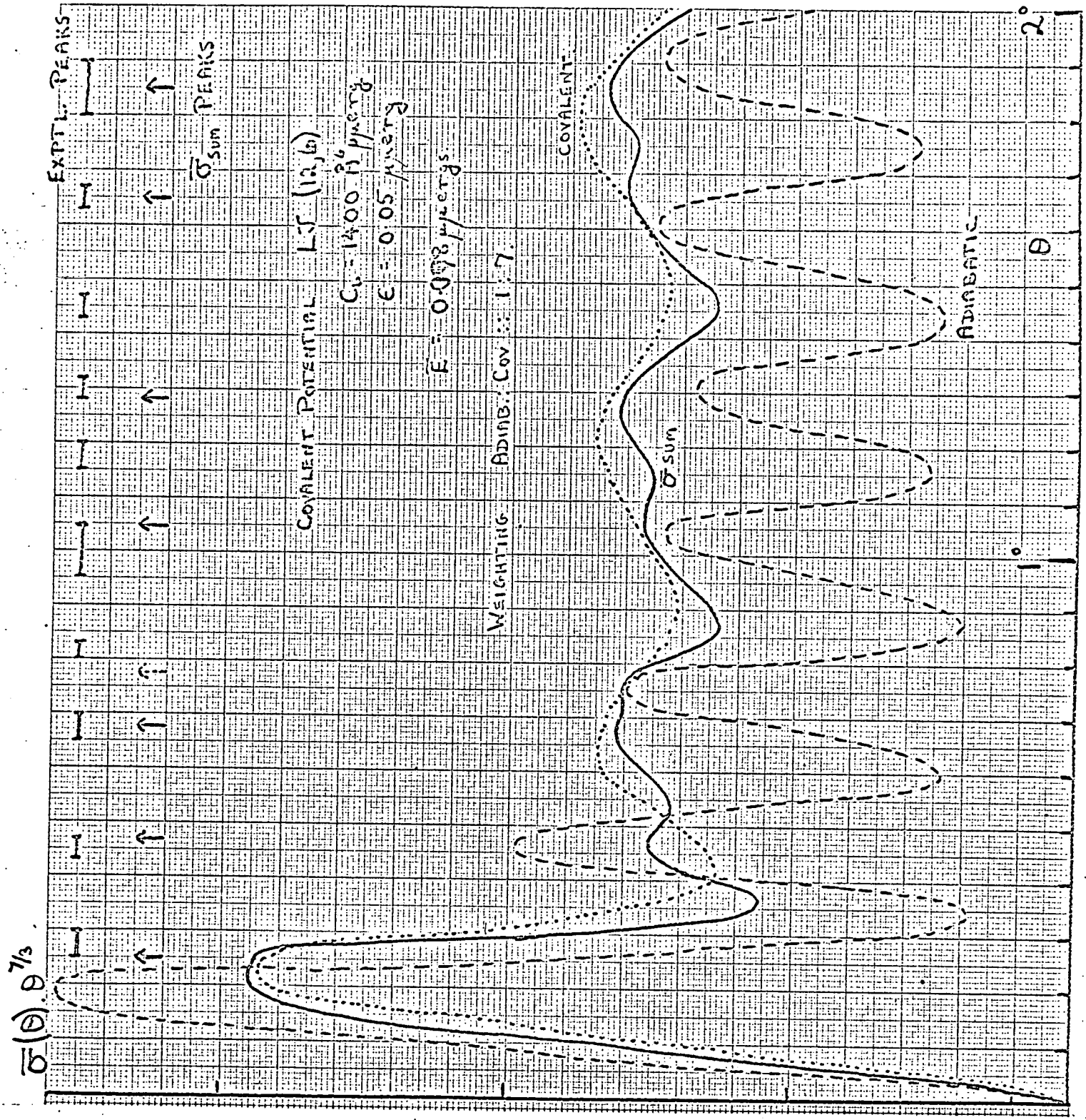

Fig. 5.27. Energy averaged cross-sections for K-I collisions

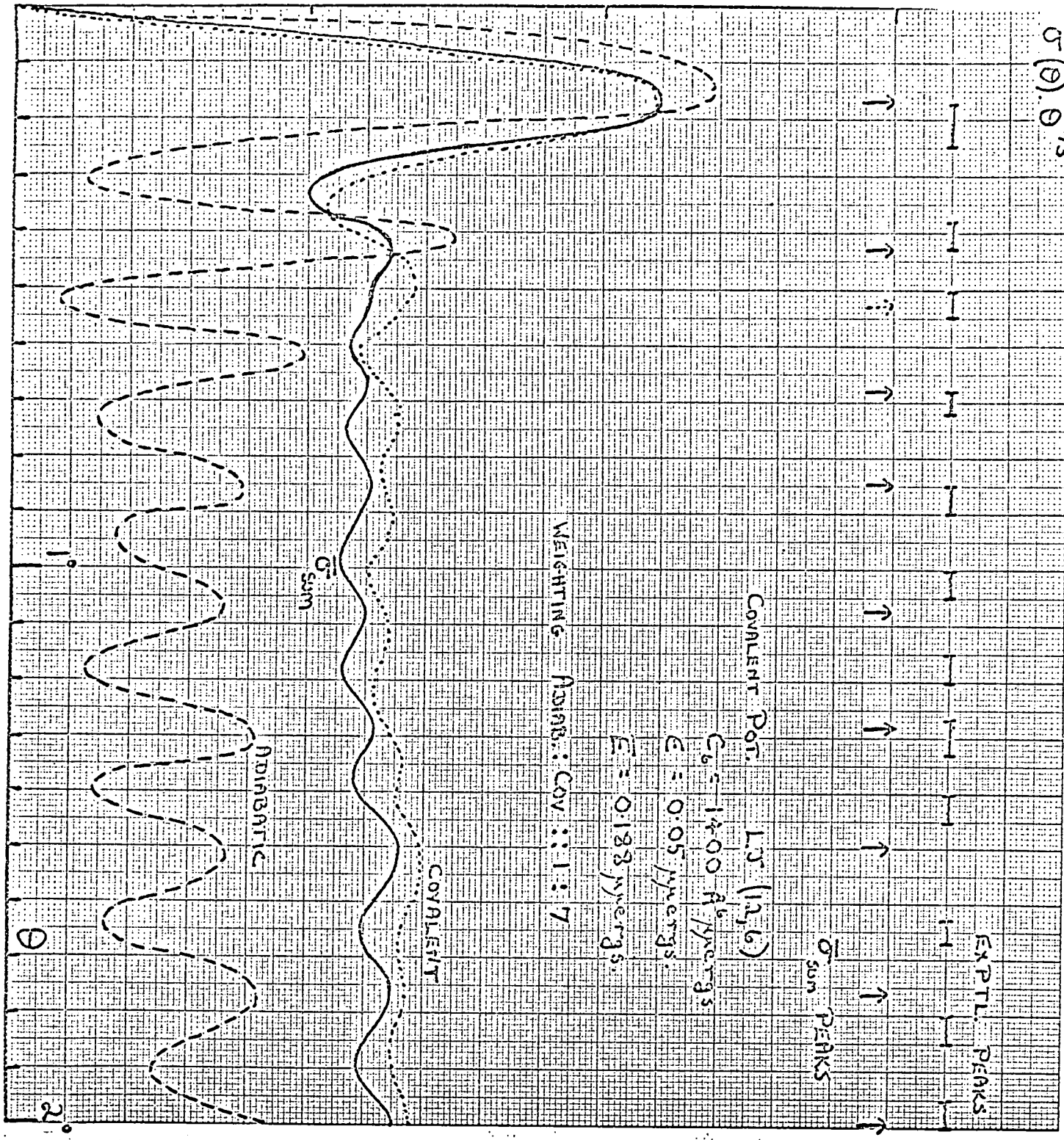

Fig. 5.28. Energy averaged cross-sections for K-I collisions.

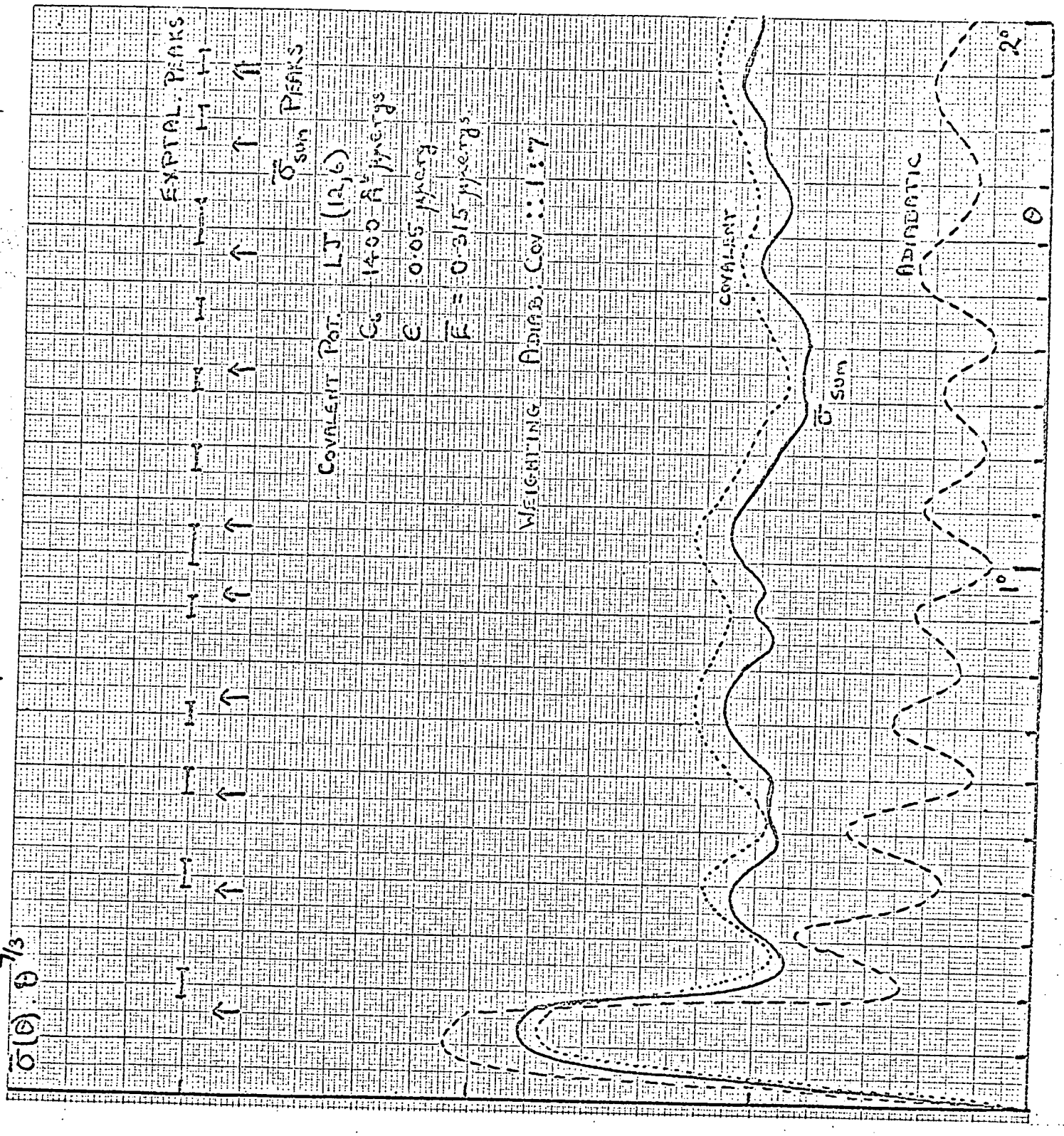

Fig. 5.29. Energy averaged cross-sections for K-I collisions.

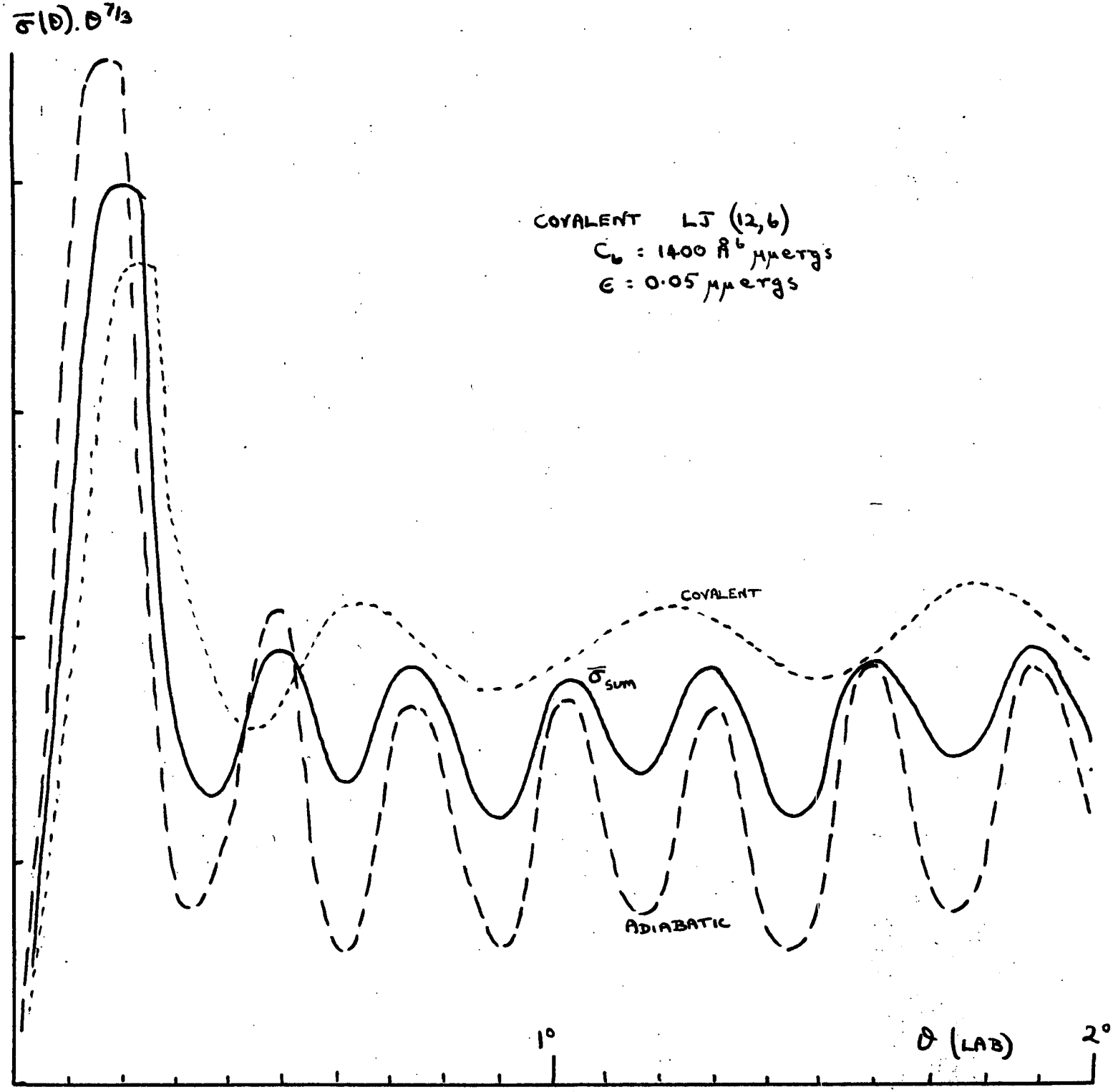

Fig. 5.30. Adiabatic + Covalent potential cross-sections (1 : 1 weighting)

Thus it would appear that the differential cross-section results are best fitted by an adiabatic potential plus a single LJ (12,6) potential which effectively reproduces the excited state interactions. These two contributions add together with the quantum statistical weights assigned to the states. Any attempt to increase the adiabatic contribution at the expense of covalent state results in the entire removal of the covalent structure, and only spreads the adiabatic peaks slightly. Fig. 5.30. shows the effect of adding the dX sections from the two states with equal weights, so that spin is conserved.

Against this model are two pieces of evidence which have yet to be considered. These are that the total cross-section curve shows a velocity dependence typical of an r^{-6} potential and secondly the model implies a large interaction constant in seeming direct contradiction to the spectroscopic experiments of Berry (BER 57)

The first objection is in fact not really a valid one since the v^{-2} dependence applies only to the adiabatic potential whose proportional contribution to the total cross-section is exactly the same as for the differential cross-section. This weighting factor is only one eighth so that in the (net) velocity dependence of the total cross-section, the v^{-2} part may be outweighed by the larger $v^{-0.4}$ contribution especially since the adiabatic total cross-section is decreasing much faster than the covalent. To test this hypothesis graphs of $Q_1 = 100/v^2$, $Q_2 = 100/v^{2/3}$ and $Q_. = \frac{1}{8} \frac{1}{8} Q_1 + \frac{7}{8} Q_2$ were drawn together with plots of log Q_1, log Q_2 and log Q versus log v. The results are shown in Fig. 5.31, where the gradient of log Q v log v is seen to be very similar to that of Q_2 which has a - 0.4 dependence. It is doubtful if our experimental total cross-sections are

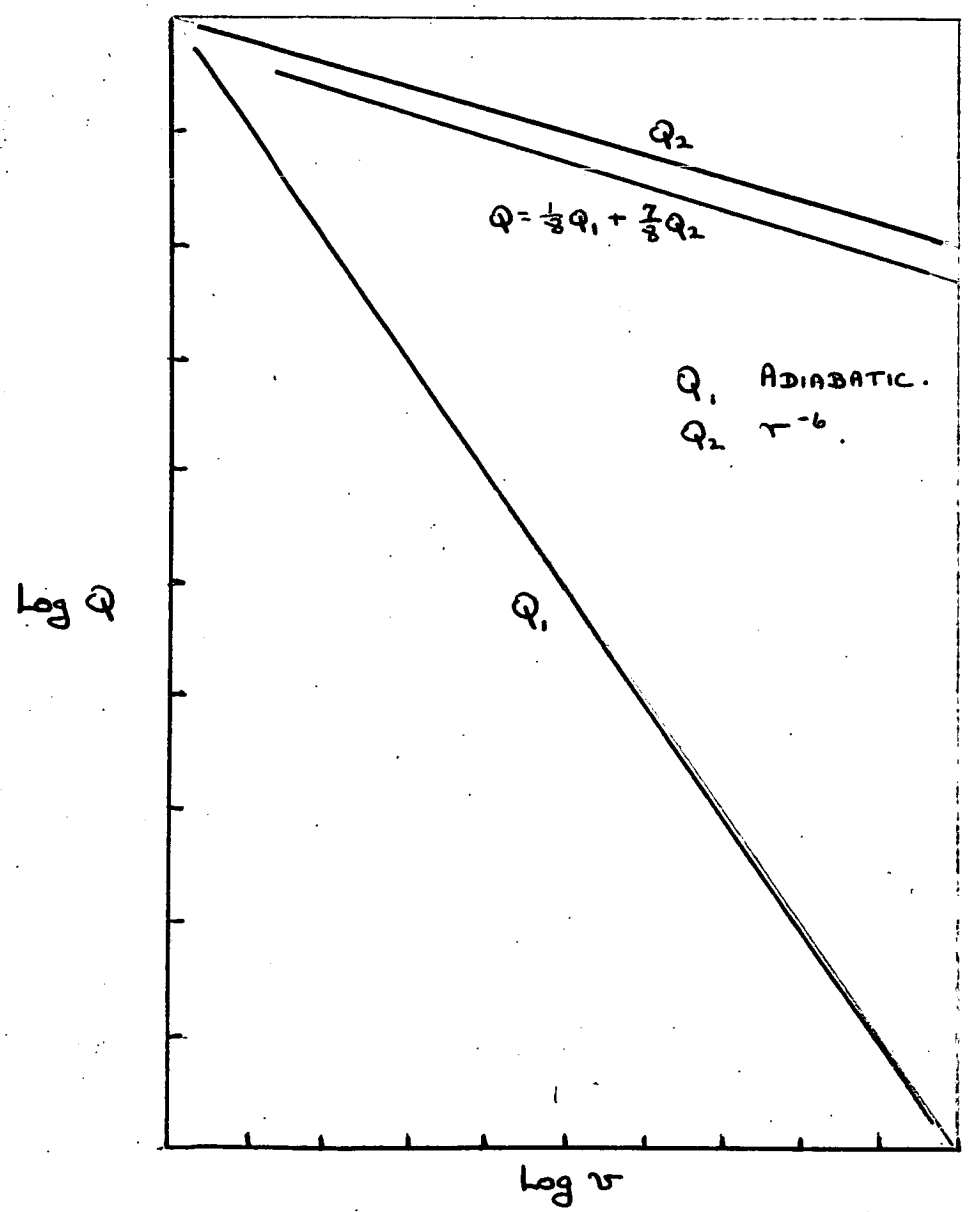

Fig. 5.31. Log-log plots for typical adiabatic and r^{-6} total cross-sections and their weighted sum.

accurate enough to distinguish the two cases.

Berry's experiments and calculations suggested that the interaction constant, A, between the ionic and covalent state was very weak for the K/I system. Child (CHI 69) has shown that the probability of switching is inversely proportional to the relative radial velocity at the crossing point as well as being directly proportional to A. Thus for a given small value of A, the transition probability μ_ℓ will be a function of impact parameter. For small values of L, μ_ℓ will be small but for larger values of L where the classical turning point is approaching the crossing point, $v_\ell \rightarrow 0$ and the probability is increasing. Small angle scattering samples these large impact parameter collision processes whereas Berry's experiments were dealing with the dissociative UV absorption spectra of the alkali halide molecule. The region of impact parameter sampled in these experiments is largely governed by the thermal distribution of rotational states of the ground state molecule and is thus fairly low. Using the simple formula (BRA 64).

$$J_{max} + \frac{1}{2} = \left(kT/2Bh\right)^{1/2}$$

and Honig et al's value of the rotational constant (HON 54) this distribution is peaked around the angular momentum quantum number value, 29, while Fig. 5.32. shows the relative population of the rotational levels.

The transition probability used in Child's calculations is given by the LZ formula.

$$P_\ell = \exp(-2\pi\delta_\ell) - 1$$

where $$\delta_\ell = \frac{k A^2}{v_\ell |f_1 - f_2|}$$

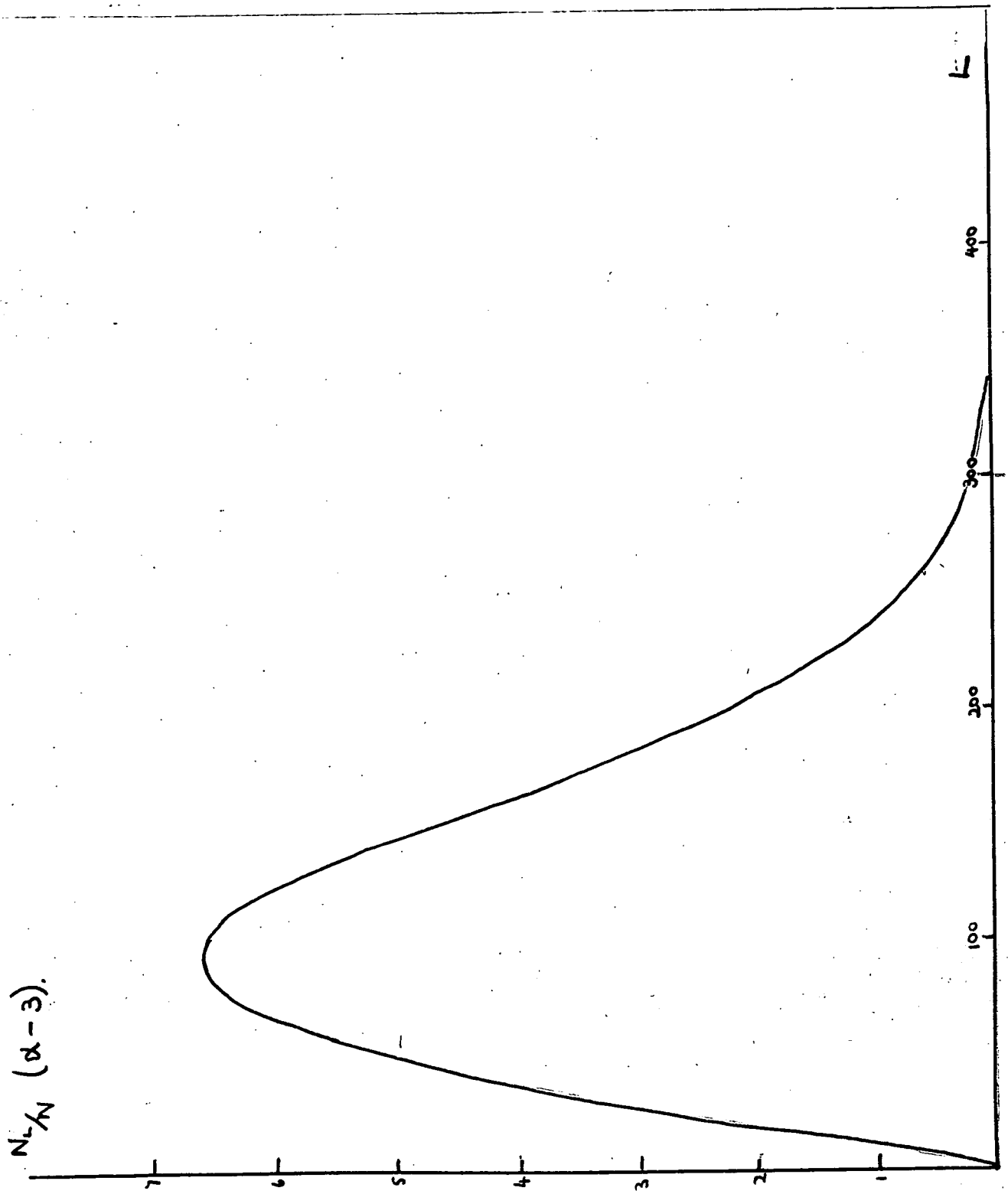

Fig. 5.32. Distribution of rotational levels in molecular KI.

For a value of the interaction constant equal to 0.001, this is shown as a function of L in Fig. 5.33. As can be seen from this figure the transition probability is very low for low L increasing as L increases.

One further point about Berry's results is the calculation of the relevant value of v_e in his case. Though the centrifugal barrier is low, his relative velocity is actually much higher than ours by a factor of three. The KI absorption limit he quotes as 3.83 eV which means that the molecule in the excited state has an excess energy of 0.5 eV (or $\sim$0.8 $\mu\mu$ergs). For his low centrifugal barrier, this energy is virtually all kinetic energy as the molecule passes through the crossing point region.

Berry's results are therefore not exactly comparable to ours. Instead they compliment one another as the two experimental situations in Figs. 5.22. and 5.23. show. His results are for high velocities and low L values whereas in our case we have low velocities and are sampling high L values.

The interaction constant is therefore small enough for the covalent curve to be followed for the lower L values but large enough for the small angle scattering to be partly governed by the adiabatic curve. In view of this both sets of results could be used to bracket the value of the interaction constant by comparing calculated scattering patterns with experiment.

Further experiments might benefit from wider angle measurements to investigate the region of impact parameter.whose contribution to the differential cross-section is determined by neither the covalent nor the ionic curve. These measurements would probably be the most useful of all, especially if carried out using a state selected iodine atom beam, which would alter the weighting in favour of the adiabatic curve allowing it to dominate the differential cross-section. If the $m_j = \frac{1}{2}$ state were selected, the only states possible for the interaction would be 0 and 1 with a 50 : 50 weighting.

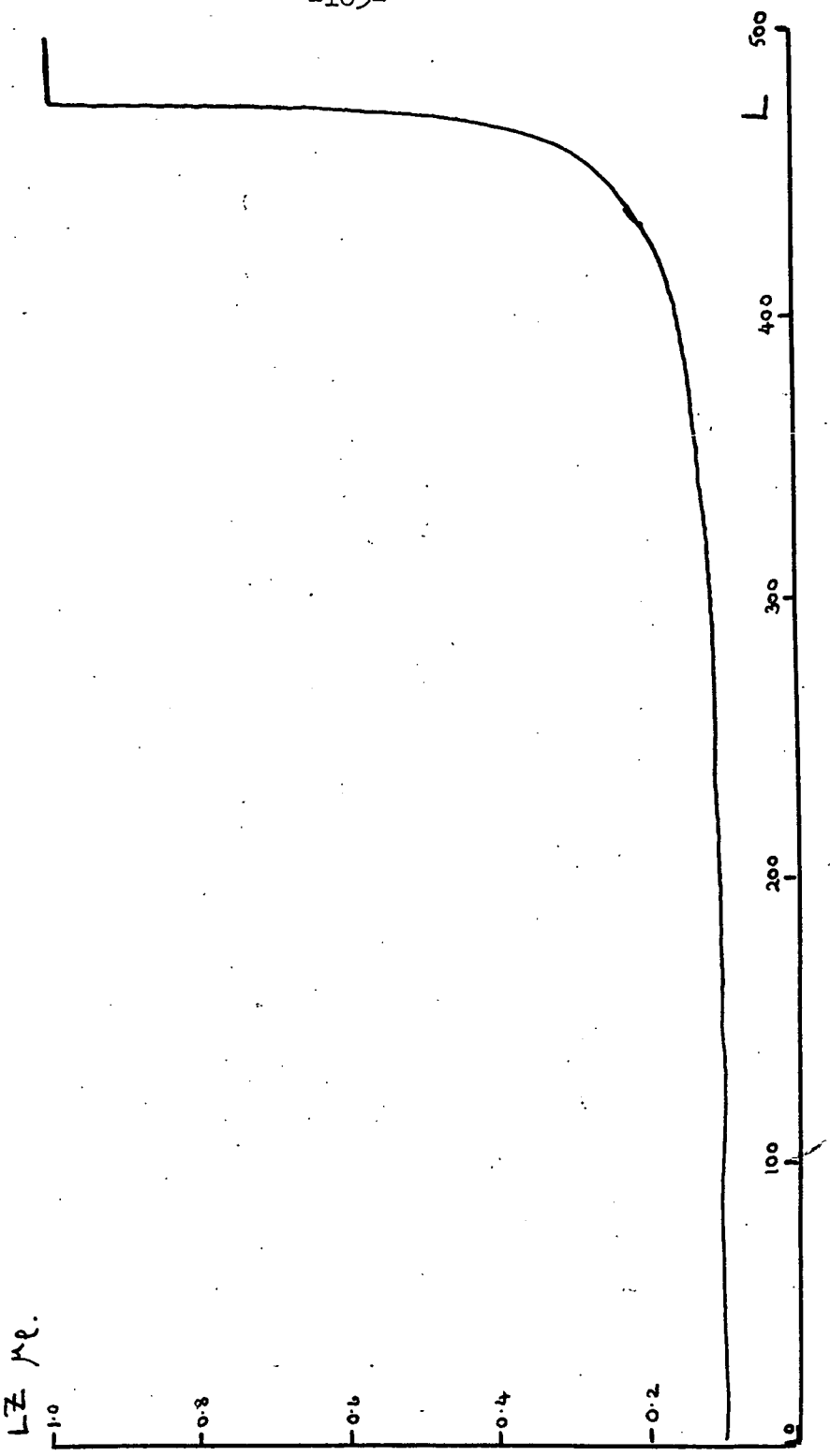

Fig. 5.33. Landau-Zener transition probability as a function of L.

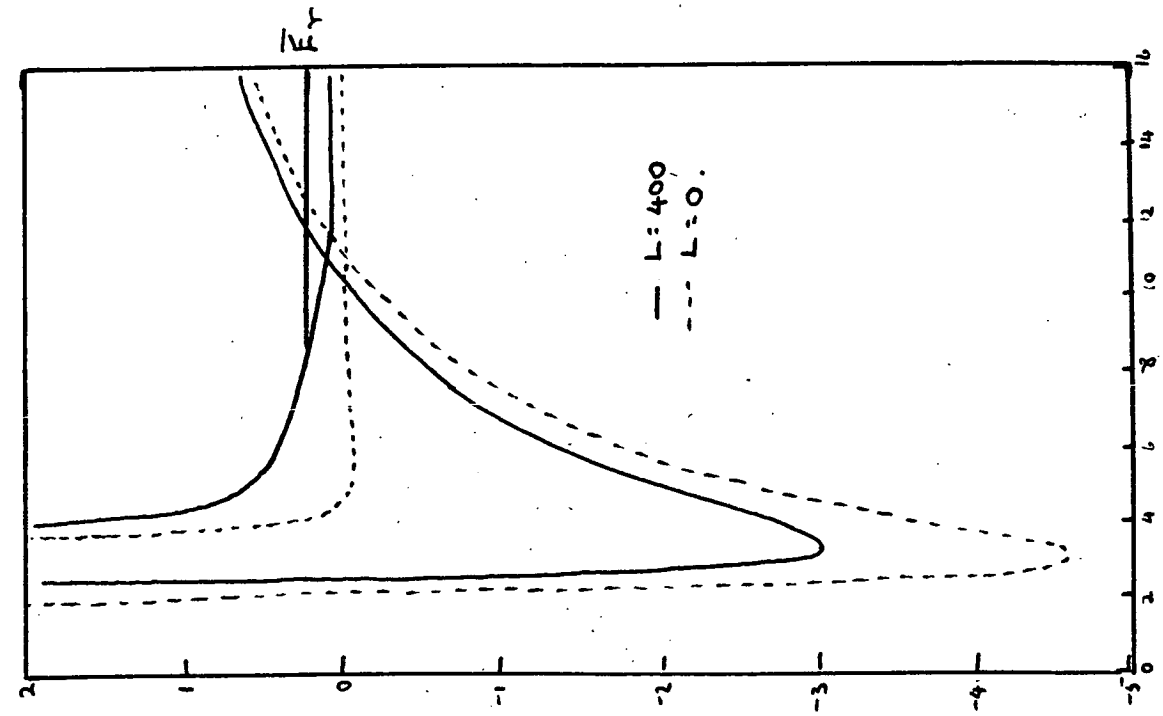

Fig 5.23.

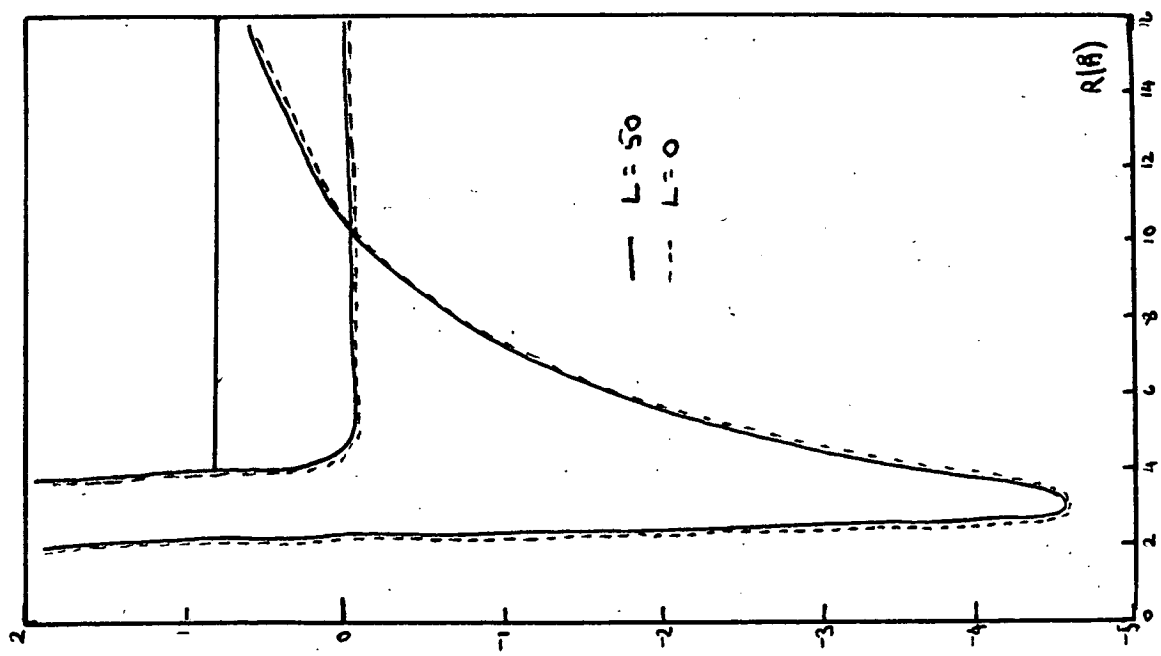

Fig 5.22.

Fig. 5.22. Effective Potential Curves for Berry's experimental situation.

Fig. 5.23. Effective potential curves for our experimental situation.

As has already been shown in Fig. 5.30. with such weighting the adiabatic scattering dominates the small angle scattering.

As far as the total cross-sections are concerned such measurements with spin selected beams altering the weighting might also reveal the v^{-2} dependence predicted for the adiabatic case. With our experimental set up measurements would benefit from sweeping through a small range (say the attenuation range) on either side of the main beam peak. Deconvolution could then be used to make up for what the apparatus lacks in resolving power.

Wider angle measurements of rainbow structure to determine the individual covalent potentials would also benefit from the use of a state selected cross-beam, eliminating or outweighing camouflage of the other interactions. The same could also be said of the small angle measurements where the molecular states which cross the ionic state could just as readily be chosen.

Potassium + Iodine Molecule Scattering.

Identical treatment was meted out to the K/I_2 data as for the K/I. The final averaged results are given in Figs. 5.6. - 5.9, the peak position plot obtained from this plot being given in Fig. 5.34. No attemps were made to measure total cross-sections with this system. In fact the K/I_2 system was studied only briefly in order to eliminate the possibility that what we thought was K/I scattering was not in fact K/I_2. Thus only the data for the lowest velocity is considered completely reliable. More work is needed to confirm the higher energy scattering patterns and their interesting results.

The rhenium surface ionizer detects both the alkali metal and the reaction product, KI, but we have a situation most readily and most simply interpreted by an 'optical model' analysis (see p171). Also although the K/I_2 system ought to involve a three-body, asymmetric and time dependent potential, an effective two body spherical potential of the Lennard-Jones type was adopted for the non-reactive interaction, the parameters of this potential to be obtained by fitting the experimental peaks.

For the optical model, some form of absorption function is required. The one adopted here is that already used in Chapter II, namely

$$p_\ell = 1 - \exp(-4\varepsilon_\ell)$$

$$\text{with} \quad \varepsilon_\ell = 1/\left(1 + \exp\left(\frac{\ell - L^*}{\Delta L}\right)\right)$$

where L^* is some angular momentum quantum number and the parameter ΔL determines the range of L about L^* in which p_ℓ varies between 0 and 1. The form of this absorption function is reproduced in Fig. 2.11. Such a function allows reaction to occur for L values considerably higher than L^* and in no way implies an abrupt electron transfer in the region of the

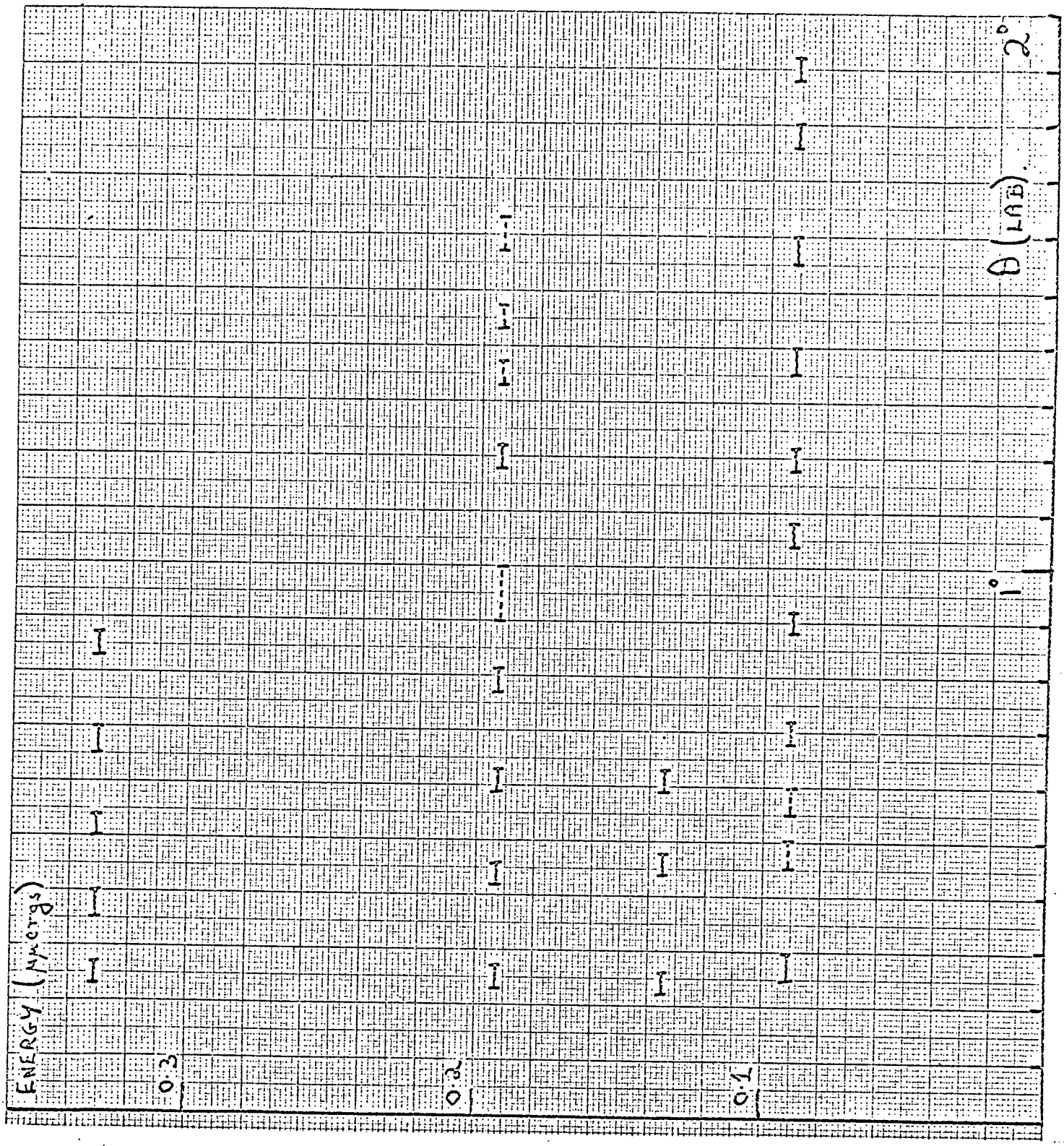

Fig. 5.34. Experimental peak position for K - I_2 collisions.

crossing point. It is, however, analogous to the electron transfer problem if one accepts that no reaction occurs on the covalent curve and that transfer to the ionic curve leads wholly to reaction.

An initial guess at the C_6 parameter for the covalent potential was calculated using the Slater-Kirkwood formula. For this the iodine molecule polarizability was taken as twice that of the iodine atom, this having been empirically estimated in Chapter II. A well depth in the range 0.02 to 0.04 μergs was initially suggested, which with the C_6 value of 1400Å^6 μergs, leads to an r_m value in the region of 5Å.

Monoenergy forward having been modified by A. W. Morris (MOR 68) to take the 'optical model', trial calculations for comparison with experiment were made using these parameters. The value of L^* in the opacity function was taken as that of an impact parameter equal to the crossing point separation. The value of 5.5Å calculated by Mintum, Datz and Becker (MIN 66) from the vertical electron affinity of I_2 was used for this. Adopting a value for ΔL of 25, the monoenergy scattering patterns of Figs. 5.35. to 5.37. were obtained for the experimental relative energies of 0.091, 0.18 and 0.331 μergs. Note that the curves here are for scattering in the centre-of-mass co-ordinate system.

Each figure contains three graphs (i) with symbol □ for $\epsilon_\ell = 0$ i.e. pure elastic scattering from the covalent potential. (ii) with symbol X which has an L^* equivalent to R_c and (iii) with symbol ◇ which has L^* equivalent to $2R_c$, and is probably unrealistic as a reaction model.

Remembering the COM angles are 1.16 times greater than the LAB angles, and comparing the angular frequency of peaks from the pure elastic case with the peak position plot of Fig. 5.34, it is immediately obvious that in this case also no single covalent curve can account for the experimentally

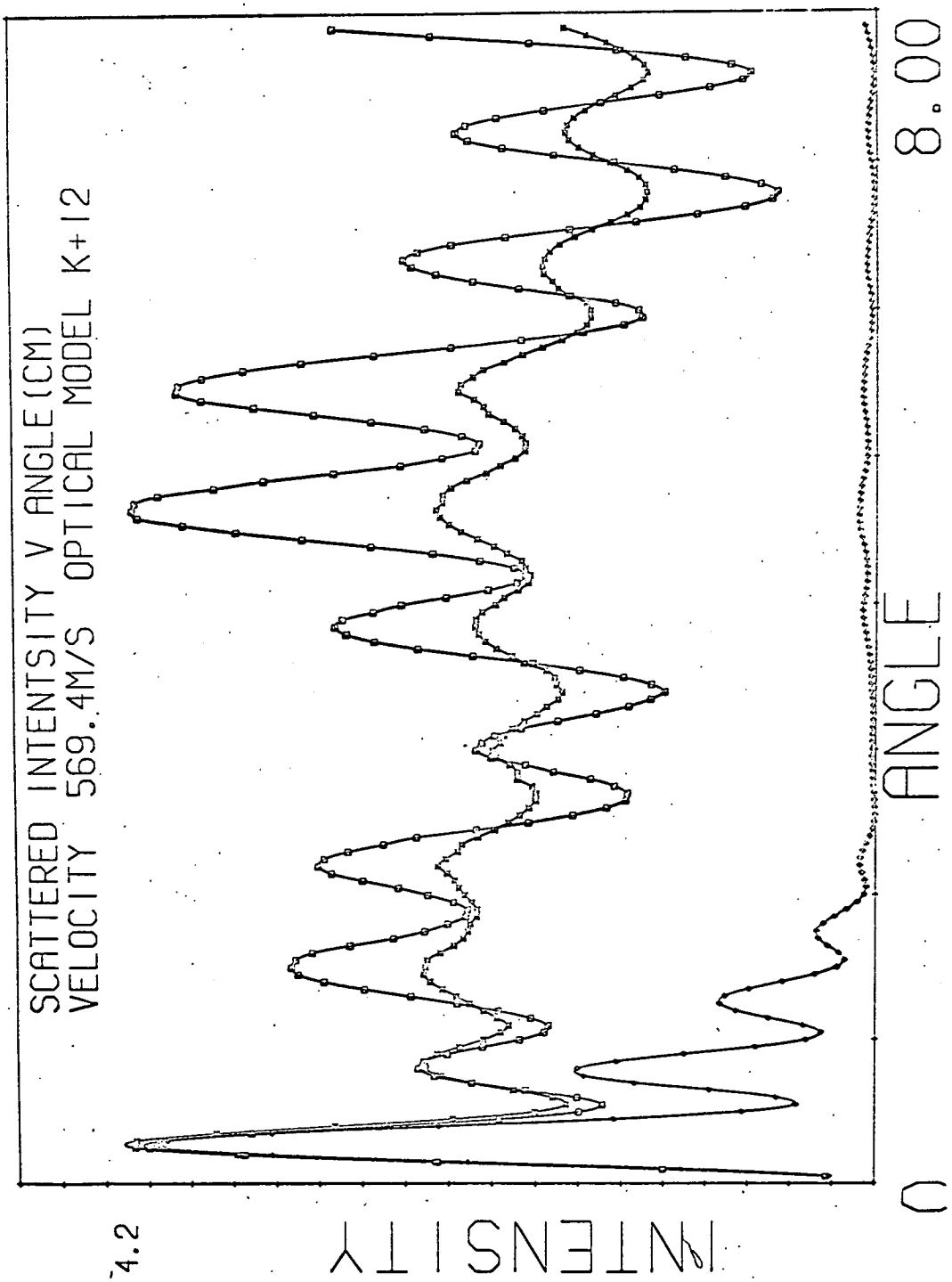

Fig. 5.35. Monoenergy optical model cross-sections.

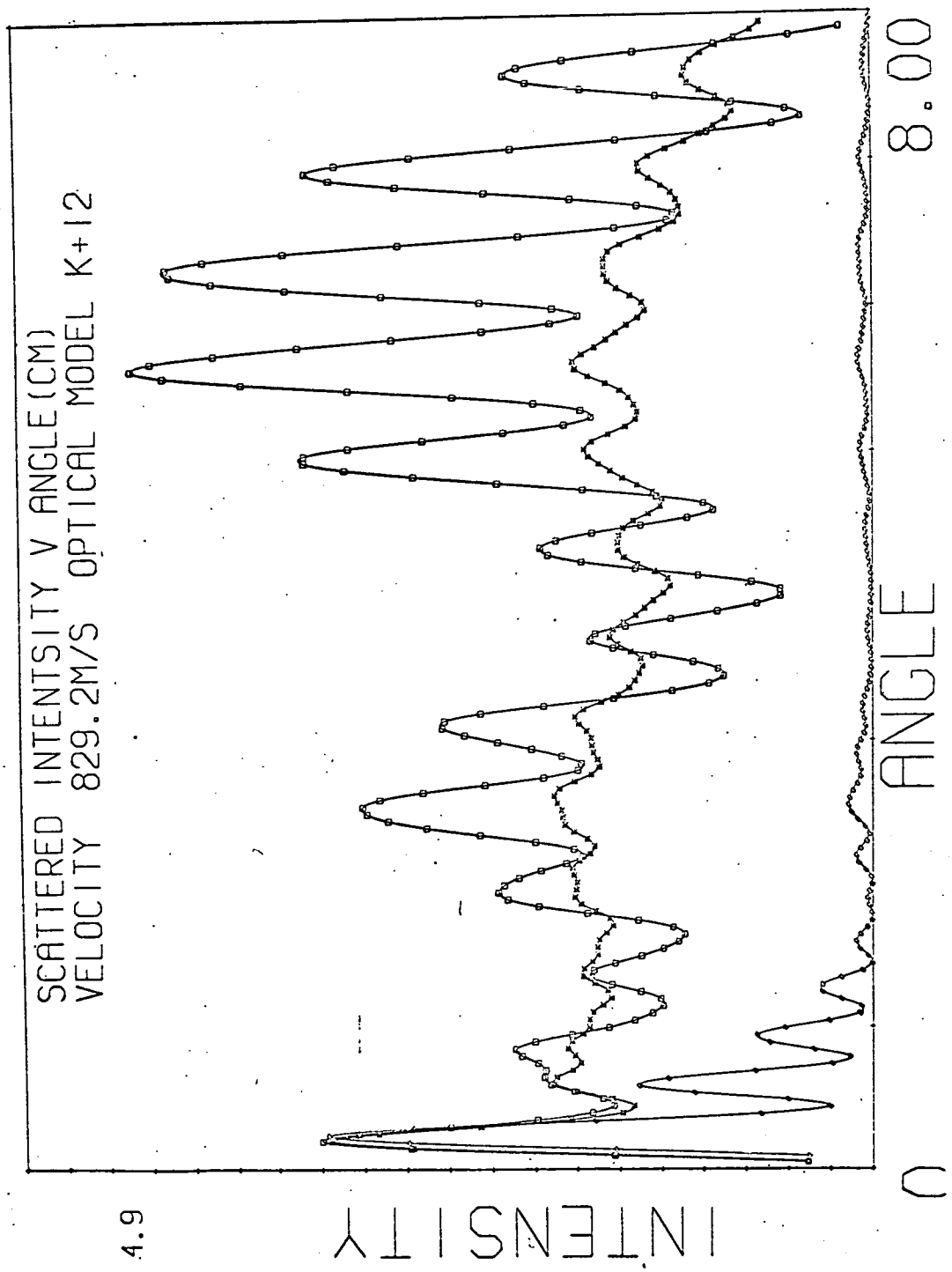

Fig. 5.36. Monoenergy optical model cross-sections.

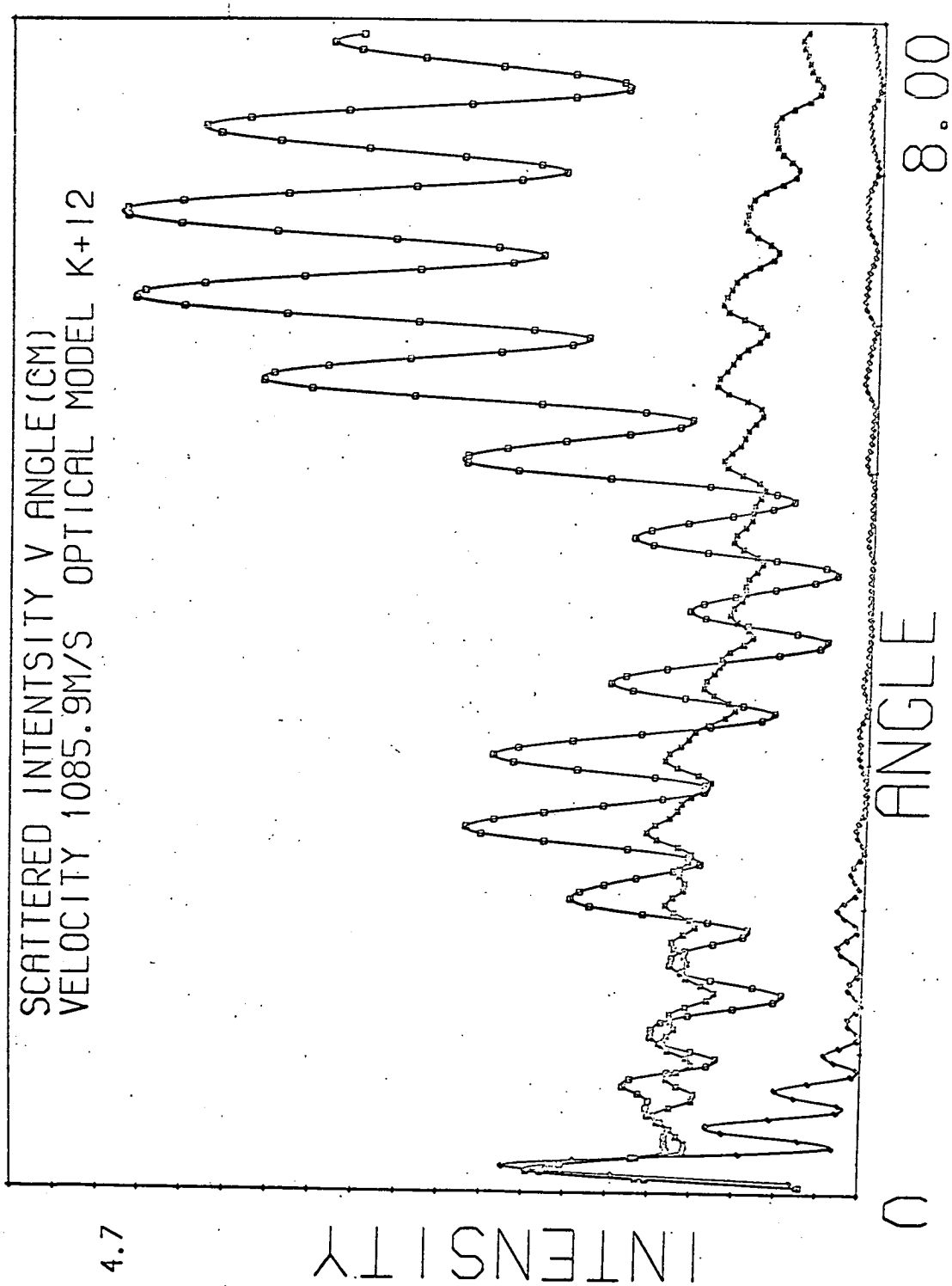

Fig. 5.37. Monoenergy optical model calculations.

observed frequency. The introduction of the optical potential, however, produces another oscillatory pattern which in the case of $L^* \equiv R_c$ superposes itself on the pure elastic pattern.

The peak positions obtained from the theoretical graphs for $L^* \equiv R_c$ are compared with the experimental plot in Fig. 5.38. Here it can be seen that many of the experimentally observed peaks are accounted for by even this first guess. There are, however, some embarrassing gaps in this preliminary analysis. Quite a few peaks are missing from the theoretical plot but notably the second peak still remains unaccounted for at all energies. In view of the lack of confidence in the data, however, no further calculations were carried out. The results are sufficiently interesting though to justify an intensive study of the small angle scattering of the potassium/iodine molecule system. They offer hope that such data will be sensitive to the form and parameters of the reaction probability function. Moreover should the sedond peak's position be confirmed and still remain unaccounted for by such an analysis, it could possibly justify the introduction of an alternative elastic channel in the system. This alternative channel would allow all of the colliding particles to switch to the adiabatic curve at the crossing point. An optical potential analysis could then be applied with this interaction as the 'reference' case. Since the parameters of the adiabatic curve are virtually fixed in that they do not alter the scattering pattern peaks, the fitting would be confined to the parameters and form of the opacity function.

Note: In the small angle scattering measured, the product KI may be neglected because

(i) it is detected with considerably less efficiency

(ii) its distribution has been observed to be peaked at $\sim 20°$

(iii) its scattering is incoherent with that of the potassium.

Fig. 5.38.
Comparison of experimental and optical model peaks for K-I collisions.

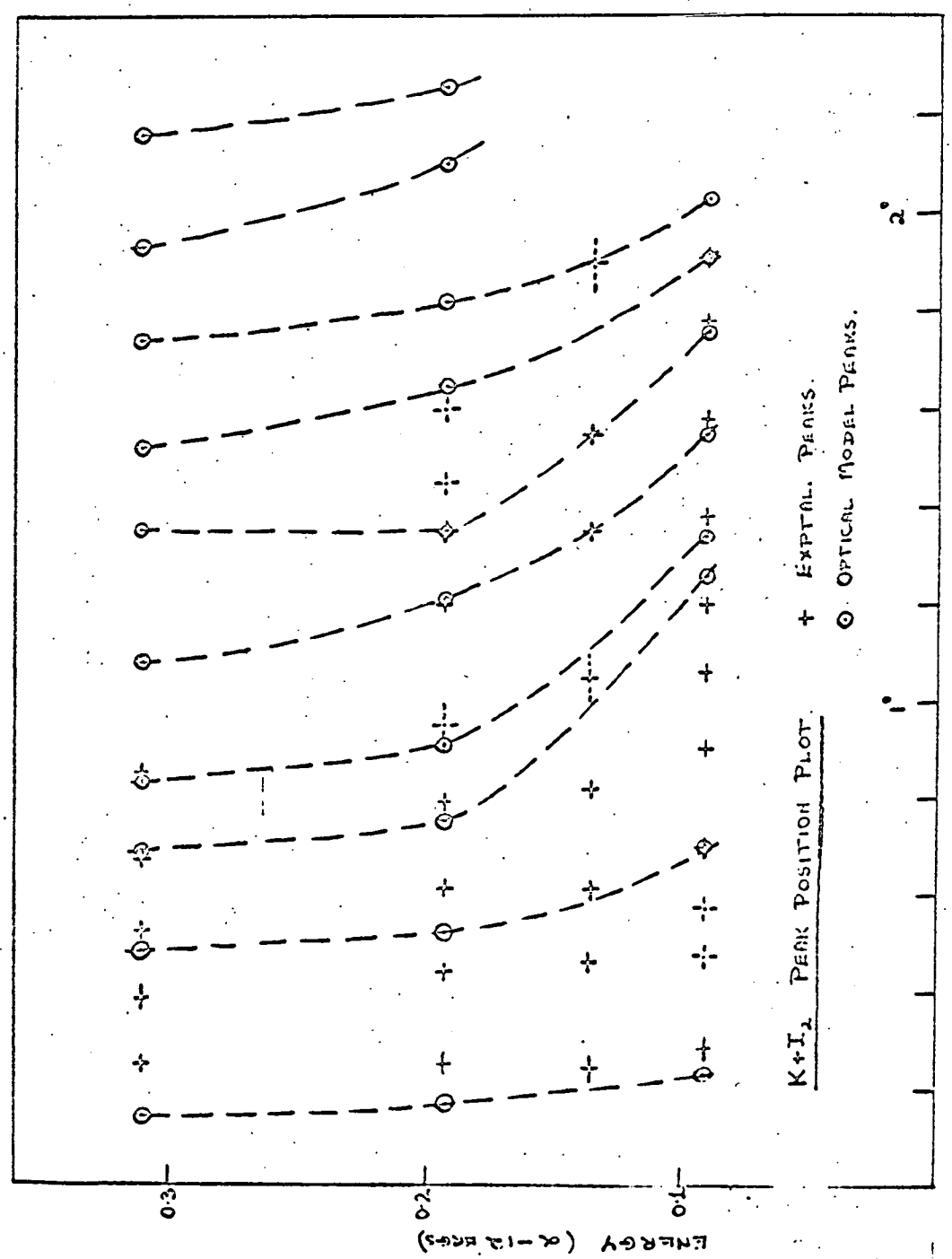

Sodium + Iodine Atom Scattering.

The differential cross-section data for this case was treated in the same manner as for the other two. The results shown in Figs. 5.10. and 5.11. are not good. So bad are they in fact that no interpretation is really possible and none has been attempted.

The total cross-section results reveal nothing very interesting either. The data here is not good enough to show any of the undulatory structure arising from the influence of short range forces, and merely shows that Q is dominated by a $v^{-2/5}$ dependent contribution.

Conclusions.

Differential cross-sections have been measured for elastic collisions between potassium and atomic iodine. The results here are consistent with a model which assumes that the O state adiabatically switches to the ionic state of the alkali halide molecule, with the other covalent interactions being represented by a LJ (12, 6) potential with $\epsilon = 5 \times 10^{-14}$ erg and $r_m = 4.9$Å. Such a model implies a large interaction between the covalent and ionic states in the region of the crossing point.

Measurements were also made for the K/I_2 system but these do not have the same degree of reliability. Preliminary analysis using an optical model reveals that the small angle scattering may be a sensitive function of the reaction probability model.

Both sets of measurements were made in the thermal energy range, the relative velocity ranging from $5 \propto 4$ to $11 \propto 4$ cm. sec^{-1}.

REFERENCES

BAR 53 R.F. Barrow & A.D. Caunt, Proc. Roy. Soc. A219,120 (1953)

BAT 60 D.R. Bates, Proc. Roy. Soc. A257,22, (1960)

BEC 68 D. Beck, F. Engelke & H.J. Loesch, Ber. Buns. Phys. Chem. 72,1105, (1968)

BED 62 B. Bederson & K. Rubin, U.S. At. Energy Commission Tech. Report. NYLO (1962) p.117.

BED 66 B. Bederson & E.J. Robinson, Adv. in Chem. Physics 10,1, (1966)

BER 62 K. Berkling, R. Helbing, K. Kramer, H. Pauly, C. Schlier & P. Toschek. Z. Physik 166,406 (1962)

BER 66 R.B. Bernstein, Adv. in Chem. Physics 10,75, (1966)

BER 68 R.B. Bernstein & R.D. Levine, 49,3872 (1968), J. Chem. Phys.

BER 57 R.S. Berry, J. Chem. Phys. 27,1288 (1957)

BER 62 R.S. Berry, C.W. Reimann & G.N. Spokes, J. Chem. Phys. 37,2278 (1962)

BIR 67 J.H. Birely, R.R. Herm, K.R. Wilson & D.R. Herschbach, J. Chem. Phys. 47,993 (1967)

BRA 64 J.C.D. Brand & J.C. Speakman, Molecular Structure - The Physical Approach. Edward Arnold (London), (1964)

BRA 68 H.M. Brash et al. Conf. on Heavy Particle Collisions, Belfast (1968)

BUC 59 A.D. Buckingham, Quart Rev. 13,183 (1959)

BYK 65 Y. Bykhovskii, E. Nikitin & M. Ovchinnikova, Soviet Phys. - JETP 20,500 (1965)

CHA 67 Tai Yup Chang. Rev. Mod. Phys. 39, 911, (1967).

CHI 69 M.S. Child, Mol. Phys. 16,313, (1969)

CIT 31 P.H. van Cittert, Z. Physik. 69,298 (1931)

CLY 63 M. Clyne & B.A. Thrush, Proc. Roy. Soc. A275,544 (1963)

COT 62 F.A. Cotton & G. Wilkinson, Advanced Inorganic Chemistry John Wiley (Interscience) (1962)

COU 61 C.A. Coulson, Valence p.178. O.U.P. (1961)

COU 62 C. Coulson & K. Zalewski, Proc. Roy. Soc. A268,437, (1962)

COW 68 L.T. Cowley, Ph. D. Thesis, Edinburgh, (1968)

COW 69 L.T. Cowley, M.A.D. Fleundy & K.P. Lawley, Trans. Faraday. Soc. 65,2027, (1969)

DAT 61 S. Datz, R.E. Minturn & E.H. Taylor, Rev. Sci. Inst. 32,210, (1961)

DUB 64 G. Dubrovskii, Soviet Phys. JETP 19,591, (1964)

EME 36 Emeleus et al. Proc. Roy. Soc. A156, 394 (1936)

FIT 67 W.L. Fite, Amer. Chem. Soc. Div. Fuel Chem. Preprints, Part 1 11(2), 1, (1967)

FLU 65 M.A.D. Fluendy, J. Sci. Inst. 42,489 (1965)

FON 53 S.N. Foner & R.F. Hudson, J. Chem. Phys. 21,1608, (1953)

FON 66 S.N. Foner, Adv. in At. & Molec. Phys. 2,385, (1966)

FRI 55 G. Fricke, Z. Physik, 141,166 (1955)

Garvin, Green & Lipworth, Phys. Rev. 111,534, (1958)

GRE 59 Greaves & Linnett, Trans. Faraday Soc. 55,1346, (1959)

HEI 68 J. Heinrichs, Phys. Rev. 176,141 (1968)

HER 63 F. Hermann & S. Skilman, Atomic Structure Calcs. (Prentice - Hall Inc. New Jersey 1963)

HER 66 D.R. Herschbach, Adv. Chem. Phys. 10,319 (1967)

HER 50 G. Herzberg, Spectra of Diatomic Molecules (Van. Nostrand Co.In. 1950)

HIR 64 J.O. Hirschfelder, C.F. Curtiss & H.B. Bird, Molecular Theory of Gases & Liquids (Wiley London 1964)

HON 54 Honig, Mandel, Stitch & Townes, Phys. Rev. 96,629, (1954)

IOU 67 G.E. Ioup & B.S. Thomas, J. Chem. Phys. 46,3959, (1967)

JAN 67 R.E.W. Jansson & L.A. Middleton, Brit. J. Appl. Phys. 18,1079, (1967)

JEN 61 K.R. Jennings, Quart. Rev. 15,237 (1961)

KUS 64 P. Kusch, J. Chem. Phys. 40,1, (1964)

LAN 32 L. Landau, Phys. Z. Sowjet. 2,46, (1932)

LAN 59 L.D. Landau & E.M. Lifshitz, Quantum Mechanics, (Pergamon Press, London, 1959)

LEV 34 H. Levi, Doctoral Dissertation, Berlin, (1934)

LEV 69 R.D. Levine, B.R. Johnson & R.B. Bernstein, J. Chem. Phys. 50,1694, (1969)

Linnett & Marsden, Proc. Roy. Soc. A234,489, (1956)

LUN 36 Lunt & Meek, Proc. Roc. Soc. A156,146, (1936)

MAG 40 J.L. Magee, J. Chem. Phys. 8,687, (1940)

MAR 66 R. Martin & M.A.D. Fleundy, Rev. Sci.Inst. (1966), 36

MAR 69 R. Marriot & D.A. Micha, Phys. Rev. 180,120, (1969)

MAS 34 H.S.W. Massey & C.B.O. Mohr, Proc. Roy. Soc. A144,188, (1934)

MAS 52 Massey & Burhop, Electronic & Ionic Impact Phenomena, Oxford (1952)

MAT 69 M. Matsuzawa, J. Phys. Soc. Japan, 25,1153, (1968)

MIN 66 R.E. Minturn, S. Datz & R.L. Becker, J. Chem. Phys. 44,1149, (1966)

MOR 68 A.W. Morris, B.Sc. Thesis, Edinburgh, (1968)

MOR 63 J.D. Morrison, J. Chem. Phys. 39,200, (1963)

MOT 65 N.F. Mott & H.S. Massey, The Theory of Atomic Collisions - 3rd edition (Oxford, 1965)

MUL 30 R.S. Mulliken, Phys. Rev. 36,699, (1930)

OGR 61 Ogryzlo, Can. J. Chem. 39,2556, (1961)

PAT 67 M.M. Patel, V.B. Gohel & M.D. Trivedi, Ind. J. Phys. 41,235, (1967)

PAU 59 H, Pauly, Z. Physik. 157,54, (1959)

PAU 65 H. Pauly & J.P. Toennies, Adv. in At. & Mol. Phys. 1,195, (1965)

PIT 59 K.S. Pitzer, Adv. in Chem. Phys. 2,59, (1959)

POL 69 J.C. Polanyi, Private Communication.

RIC 57 S.A. Rice & W. Klemperer, J. Chem. Phys. 26,573 (1957)

RIT 51 E.S. Rittner, J. Chem. Phys. 19,1030 (1951)

ROD 67 L.S. Rodberg & R.M. Thaler, Introduction to the Quantum Theory of Scattering (1967)

Rodebush & Klinglehoffer, J. Amer. Chem. Soc. 55,130, (1933)

ROS 67 H.Y. Sun & J. Ross, J. Chem. Phys. 46,3306, (1967)

ROS 69 E.F. Greene, L.F. Hoffman, M.W. Lee, J. Ross & C.E. Young, J. Chem. Phys. 50,3450, (1969)

SAL 60 L. Salem, Molec. Physics. 3,441, (1960)

SHA 59 T.M. Shaw, J. Chem. Phys. 31,1142, (1959)

SLA 60 J.C. Slater, Quantum Theory of At. Structure, McGraw Hill (1960)

SOM 29 K. Sommermeyer, Z. Physik, 56,548, (1929)

STU 32 E.C.G. Stueckelberg, Helv. Phys. Acta 5,369, (1932)

VAR 61 Varshni & Shukla, J. Chem. Phys. 35,582, (1961)

WAT 68 K.M. Watson, in Properties of Matter under Unusual Conditions, edited by H. Mark (Wiley, 1968)

WES 53 G. Wessel & H. Lew, Phys. Rev. 92,641, (1953)

WIG 28 E. Wigner & E.E. Witmer, Z. Phys. 51,859, (1928)

WOO 20 Wood, Proc. Roy. Soc. A97,455, (1920)

WU 62 T. Wu & T. Ohmura, Quantum Theory of Scattering (1962)

ZEN 32 C. Zener, Proc. Roy. Soc. A137,696, (1932)

ABSTRACT OF THESIS

Name of Candidate DAVID SMITH HORNE.

Address 23 CLEGHORN DRIVE, BROXBURN, WEST LOTHIAN.

Degree DOCTOR OF PHILOSOPHY. *Date* OCTOBER, 1969.

Title of Thesis THEORETICAL AND EXPERIMENTAL STUDIES OF ATOMIC AND MOLECULAR SCATTERING.

Small angle differential cross-sections in the thermal energy range are reported for the elastic scattering of potassium from atomic and molecular iodine. Such interactions are among the simplest two-state curve crossings to be found in chemistry.

The situation is complicated by the fact that the curve-crossing case is only one of four which can occur when an alkali metal and a halogen atom collide. It was hoped that information on both the curve-crossing and these other interactions would be derived from the small angle scattering in the thermal energy range.

The molecular beam apparatus had already been constructed for alkali metal-alkali metal collisional studies. The chief modification to this was the building of a halogen atom source. The iodine atom source was of a two-chamber design, with the temperature of the upper chamber controlling the degree of dissociation. A radio frequency discharge source for atomic chlorine is also described.

The other main modification was the introduction of a cross-beam modulation system to increase the detection efficiency. As before the primary beam was velocity selected before collision, the scattered alkali particles being surface ionized and subsequently counted.

In both iodine atom and molecule cases differential cross-sections were measured at three different relative collision energies. The angular structure in the iodine atom system was found to be best interpreted in terms of an adiabatic potential involving an electron transfer at the crossing point plus an 'effective' covalent potential to account for the other three interactions. This latter potential is a Lennard-Jones (12,6) with $\epsilon = 5 \times 10^{-12}$ ergs and

Use other side if necessary.

$C_6 = 1400 \times 10^{-60}$ ergs cm .

The interpretation of the iodine molecule results has been based on the 'optical model' treatment since in this case chemical reaction opens another exit channel for the scattering species. The results here lend hope that the small angle scattering of reactive species will prove to be a sensitive function of both the form and parameters of the reaction probability function.